STARS

Electronic Theses and Dissertations, 2004-2019

2008

Extended Focus Range High Resolution Endoscopic Optical Coherence Tomography

Kye-Sung Lee
University of Central Florida

Part of the Electromagnetics and Photonics Commons, and the Optics Commons

Find similar works at: https://stars.library.ucf.edu/etd

University of Central Florida Libraries http://library.ucf.edu

Showcase of Text, Archives, Research & Scholarship

EXTENDED FOCUS RANGE HIGH RESOLUTION
ENDOSCOPIC OPTICAL COHERENCE TOMOGRAPHY

by

KYE-SUNG LEE
B.S. Kyungpook National University, Daegu, South Korea 1997
M.S. Kyungpook National University, Daegu, South Korea 2000

A dissertation submitted in partial fulfillment of the requirements
for the degree of Doctor of Philosophy
in the College of Optics and Photonics: CREOL & FPCE
at the University of Central Florida
Orlando, Florida

Fall Term
2008

Major Professor: Jannick P. Rolland

ABSTRACT

Today, medical imaging is playing an important role in medicine as it provides the techniques and processes used to create images of the human body or parts thereof for clinical purposes (medical procedures seeking to reveal, diagnose or examine disease) or medical science (including the study of normal anatomy and function). Modalities are developing over time to achieve the highest possible resolution, speed of image acquisition, sensitivity, and specificity. In the past decade, advances in optics, fiber, as well as laser technology have enabled the development of noninvasive optical biomedical imaging technology that can also be applied to endoscopy to reach deeper locations in the human body. The purpose of this dissertation is to investigate a full system design and optimization of an optical coherence tomography (OCT) system to achieve high axial and lateral resolution together with an extended depth of focus for endoscopic *in vivo* imaging.

In this research aimed at advancing endoscopic OCT imaging, two high axial resolution optical coherence tomography systems were developed: (1) a spectrometer-based frequency-domain (FD) OCT achieving an axial resolution of ~2.5 μm using a Ti:Sa femtosecond laser with a 120nm bandwidth centered at 800nm and (2) a swept-source based FD OCT employing a high speed Fourier domain mode locked (FDML) laser that achieves real time *in vivo* imaging with ~8 μm axial resolution at an acquisition speed of 90,000 A-scans/sec. A critical prior limitation of FD OCT systems is the presence of mirror images in the image reconstruction algorithm that could only be eliminated at the expense of depth and speed of imaging. A key contribution of this research is the development of a novel FD OCT imager that enables full range depth imaging without a loss in acquisition speed. Furthermore, towards the need for better

axial resolution, we developed a mathematical model of the OCT signal that includes the effect on phase modulation of phase delay, group delay, and dispersion. From the mathematical model we saw that a Fourier domain optical delay line (FD ODL) incorporated into the reference arm of the OCT system represented a path to higher performance. Here we then present a method to compensate for overall system dispersion with a FDODL that maintains the axial resolution at the limit determined solely by the coherence length of a broadband source.

In the development of OCT for endoscopic applications, the need for long depth of focus imaging is critical to accommodate the placement of the catheter anywhere within a vessel. A potential solution to this challenge is Bessel-beam imaging. In a first step, a Bessel-beam based confocal scanning optical microscopy (BCSOM) using an axicon and single mode fiber was investigated with a mathematical model and simulation. The BCSOM approach was then implemented in a FD OCT system that delivered high lateral resolution over a long depth of focus. We reported on the imaging in biological samples for the first time with a double-pass microoptics axicon that demonstrated clearly invariant SNR and 8 μm lateral resolution images across a 4 mm depth of focus. Finally, we describe the design and fabrication of a catheter incorporated in the FD OCT. The design, conceived for a 5 mm outer diameter catheter, allows 360 degree scanning with a lateral resolution of about 5 μm across a depth of focus of about 1.6 mm. The dissertation concludes with comments for related future work.

To my mother Hong-Ryun

To my family

ACKNOWLEDGMENTS

the whole ODALab team for their friendship. I also thank UCF friends including Korean friends. Especially I thank my best friend Chul-Whan Kim and good friends in Korea. My very special thanks go to my family: my mother Hong-Ryun Lee, my father Jeung-Su Lee and my sister Sung-Lim Lee.

TABLE OF CONTENTS

LIST OF FIGURES

LIST OF TABLES

LIST OF ACRONYMS

A/D	Analog-to-Digital Converter
BCSOM	Bessel-beam based Confocal Scanning Optical Microscopy
BW	Bandwidth
CAD	Coronary Artery Disease
CARS	Anti-Stokes Raman Scattering
COPD	Chronic Obstructive Pulmonary Disease
CT	Computed Tomography
DEJ	Dermal Epidermal Junction
DOF	Depth of Focus
DR FROCT	Dual Reference Full Range FD OCT
ED	Epidermis
FD OCT	Frequency Domain Optical Coherence Tomography
FD ODL	Fourier Domain Optical Delay Line
FDML	Fourier Domain Mode Locking
FFP-TF	Fiber Fabry-Perot Tunable Filter
FSR	Free Spectral Range
FWHM	Full-Width at Half-Maximum
IVUS	Intravascular Ultrasound
MI	Myocardial Infarctions
MRI	Magnetic Resonance Imaging
MZI	Mach-Zehnder Interferometer

NA	Numerical Aperture
NMR	Nuclear Magnetic Resonance
OCM	Optical Coherence Microscopy
OCT	Optical Coherence Tomography
OSA	Optical Spectrum Analyzer
PET	Positron Emission Tomography
PID	Proportional-Integral-Derivative
PSF	Point Spread Function
SC	Stratum Corneum
SD OCT	Spectral Domain Optical Coherence Tomography
SD	Sweat Ducts
SLD	Superluminescent Diode
SNR	Signal to Noise Ratio
SOA	Semiconductor Optical Amplifier
SPECT	Single Photon Emission Computed Tomography
TD OCT	Time Domain Optical Coherence Tomography

CHAPTER ONE: INTRODUCTION

Chapter One begins with a summary of various modern medical imaging modalities. Then, the origin and basics of biomedical optical imaging are reviewed. We then introduce Optical Coherence Tomography (OCT). Finally, our motivation for the research and summary followed by the dissertation outline are presented.

1.1 Modern Medical Imaging Modalities

Noninvasive medical imaging techniques have revolutionized diagnostic medicine since the early 1960s. There are four categories: X-ray computed tomography (CT), radionuclide imaging, ultrasound, and magnetic resonance imaging (MRI). X-ray imaging was discovered accidentally by W. K. Roentgen in 1895. In conventional X-ray radiography, an X-ray image is made either by exposing a photographic film to the X-ray or by converting the X-ray photons to visible photons with fluorescent screens and imaging the screen onto a CCD. As fast data acquisition and mass data storage has been made possible by improving computer technology, X-ray images are now routinely reconstructed in 2D and 3D tomographical images.

The concept and the term radionuclide imaging was proposed by Kohman in 1947 to describe a nucleus with a measurable half-life of radioactive decay. Here, radioactive chemical tracers emitting gamma rays or positrons can provide diagnostic information about a person's internal anatomy and the functioning of specific organs. These are used today in some forms of tomography: single photon emission computed tomography (SPECT), and positron emission tomography (PET).

The potential of ultrasound as an imaging modality was realized as early as the late 1940s, borrowing from sonar technology used in World War Ⅱ. The ultrasound-based imaging modality has become a widely accepted diagnostic tool to visualize muscles, internal organs, and pregnancy.

The phenomenon of nuclear magnetic resonance (NMR), discovered by F. Block and E. Purcell in 1946, has become a standard spectroscopic technique in chemistry and physics. Nuclear magnetic resonance imaging, abbreviated MRI in the clinical field, has the advantages of being able to penetrate bony and air-filled structures with negligible attenuation and artifacts. This modality uses non-ionizing radiation and is minimally invasive, however it is expensive at this time.

In the past decade, advances in optics, fiber, as well as laser technology, have enabled the development of a novel noninvasive optical biomedical imaging technology. Optical imaging presents several potential advantages over existing radiological techniques in medicine because optical photons provide safe nonionizing radiation for medical applications. Light interacts with biological tissue in various ways including absorption, scattering, polarization, variation in absorption with wavelength, fluorescence, Raman scattering, etc. Leveraging the interactions of light behavior in biological tissue, various imaging modalities have emerged and are being actively advanced in research laboratories, including confocal microscopy, two-photon microscopy, diffuse optical tomography, optical coherence tomography, anti-Stokes Raman scattering (CARS), and optical spectroscopy.

1.2 Introduction to OCT

Optical coherence tomography (OCT) is analogous to ultrasound imaging. It is based on measuring the backreflection intensity of infrared light, rather that sound. However, unlike ultrasound, the backreflection intensity cannot be measured electronically given the high speed of light propagation. Therefore, a technique known as low coherence interferometry is used. OCT measurements of echo time delay are based on correlation techniques that compare the backscattered or backreflected light signal to a reference light signal traveling a known path length in another arm of the interferometer. In contrast to conventional microscopy, in OCT the mechanisms that govern the axial and transverse image resolution are independent. The axial resolution in OCT imaging is determined by the coherence length of the light source. Specifically, the axial depth resolution is inversely proportional to the bandwidth of the light source and therefore broad-bandwidth optical sources are required to achieve high axial resolution. The transverse resolution is the same as for conventional optical microscopy and is determined by the numerical aperture of the optical beam in the sample. In the beginning, Huang *et al.* successfully used an optical coherence domain reflectometry technique to measure corneal thickness, corneal excision depth, and anterior chamber depth of the eye with a spatial depth resolution of 10 μm. In 1991, an article was published in *Science* with the title of "Optical Coherence Tomography". In the article, for the first time, 2-dimensional cross-sectional images of internal structures in biological samples were demonstrated. Recently, Frequency Domain Optical Coherence Tomography (FD OCT) has attracted significant interest because of its improved sensitivity and imaging speed compared to time domain OCT (TD OCT). There are two types of FD OCT; Spectrometer OCT and Swept Source OCT. Basically for both types,

23

axial depth information is derived from the spectrum of the interference between signals from a reference arm and the sample. The spectrum is obtained from a spectrometer or a swept source without depth scanning. The Fourier transformation of the measured spectrum delivers the depth information. In the medical imaging market, OCT is appearing in clinical applications in ophthalmology. OCT has also been investigated for monitoring the growth of epithelial and subepithelial layers of internal organs such as lungs, urinary bladder, human intestine, and coronary arteries with endoscopic OCT.

1.3 Motivation

Today, medical imaging is playing an important role in medicine as the techniques and processes used to create images of the human body or parts, thereof for clinical purposes (medical procedures seeking to reveal, diagnose or examine disease) or medical science (including the study of normal anatomy and function). All modalities for invasive medical imaging are being developed to provide higher resolution and higher sensitivity images for a broader range of sites in and on the human body at even higher image acquisition speed. Various optical imaging modalities using light are currently emerging as promising new additions with some superior aspects compared to current imaging modalities. OCT in particular has established itself as a high-resolution imaging modality.

Cardiovascular disease represents the leading cause of death worldwide. In the United States, the prevalence of coronary artery (CAD) is approximately 13 million with myocardial infarctions (MI) at 7 million in 2002. Deaths from MI (not including heart failure, strokes, or

24

arrhythmias) were approximately 600,000 in the same year, while all cancers together totaled 560,000, accidents 106,000, Alzheimer 59,000, and HIV 14,000.

Three of the most common lung diseases are asthma, chronic obstructive pulmonary disease (COPD), and lung cancer. About 20 million Americans have asthma. COPD is a term that describes related diseases: chronic obstructive bronchitis and emphysema. COPD is the fourth leading cause of death in the United States. Lung cancer is the second most common cancer diagnosed in men and women, but the leading cause of cancer mortality in the United States. Current imaging techniques employed for diagnosis of lung disease do not provide sufficient resolution to detect critical early pathologic changes within the bronchial epithelium.

High frequency ultrasound among imaging modalities has been used for diagnosis of cardiovascular and lung diseases. However, ultrasound imaging has several significant limitations. Catheters are relatively large use of low resolution with a current axial resolution of 80~90 μm using 40MHz ultrasound. The high frequency intravascular ultrasound (IVUS) has been compared with OCT for intravascular imaging. The comparison of OCT with IVUS validated the superior resolution of OCT. At present, intravascular OCT *in vivo* imaging with 40 μm lateral and 15 μm axial resolution, respectively, was commercially developed using a 430 μm imaging guidewire in the presence of a saline flush. Endoscopic imaging with conventional light focusing faces a fundamental conflict between depth of focus and lateral resolution particularly in the very limited space to an imaging catheter. A full system design and optimization of an optical coherence tomography system including the light source, the detection technology, the scanning in an interferometer, as well as a new light focusing scheme are explored here resulting in higher axial and lateral resolution over an extended depth of focus.

1.4 Research Summary

The purpose of the research is to implement an optical coherence tomography system for high resolution and extended depth of focus endoscopic *in vivo* imaging in tubular structures, such as the intravascular wall and the tracheobronchial tree. We will deal in order with

- achieving high axial resolution FD OCT systems with extended depth imaging range,

- keeping the axial resolution by removing dispersion in the system,

- obtaining high lateral resolution over extended depth of focus with Bessel beam imaging including the design and fabrication of a Bessel-beam based catheter for endoscopic imaging, and

- suppressing mirror images intrinsic to the basic FD OCT technique.

The first system to be designed, simulated, and implemented is a spectrometer based FD OCT with a broadband femtolaser source providing high axial resolution. This system was applied to various biological imaging subjects including a tadpole, an onion, and engineered tissues and was also used to gather high resolution images of femtosecond pulsed laser-written 3D structures. The second system to be designed, simulated, and implemented is a swept source FD OCT with a high speed Fourier domain mode lock (FDML) laser that provides real time imaging of human skin. We also present a dual reference, full range, swept source FD OCT system implemented to double the imaging depth by removing mirror images generated from the Fourier transform of the detected real valued spectra.

Dispersion in OCT is a critical issue. The fiber optics, the specimen, and other dispersive components in a fiber optic interferometer may introduce significant dispersion resulting in a degradation of axial resolution. We demonstrate the impact of dispersion up to second-order in a

fiber-optic interferometer that has the general structure of an OCT system. We study a mathematical model of the OCT signal including the effect of phase modulations including phase delay, group delay, and dispersion. This model is then studied with a Fourier domain optical delay line (FD ODL) incorporated to the reference arm of the OCT system. We then investigate dispersion compensation with the FD ODL and present a practically useful method to minimize the effect of dispersion through the interferometer and the specimen combined. Finally, we quantify the results using two general metrics for resolution.

We study Bessel-beam based confocal scanning optical microscopy (BCSOM) using an axicon and single mode fiber with a developed mathematical model and simulations showing suppression of sidelobes coming from the Bessel beams. The BCSOM is then applied to frequency domain OCT to achieve high resolution over a long depth of focus. We report on the collection efficiency measured across the depth of focus of a custom-made microoptic axicon lens designed to theoretically achieve an 8 mm depth of focus. The efficiencies are compared to those of a conventional lens of equivalent resolution at its focal plane. Based on these measurements, the sensitivities achieved in a frequency domain optical coherence tomography system were derived and compared for both types of beams, Bessel and Gaussian. Imaging in biological samples is demonstrated for the first time with axicon microoptics (i.e., <1 mm in diameter) showing invariant SNR and invariant 8 μm lateral resolution images across a 4mm depth of focus.

A biophotonic catheter was then conceived for endoscopic OCT with the investigated collimation optics and the axicon lens combined with custom design imaging optics, yielding a 360 degree scan aimed at imaging within concave structures such as lung lobes. This device

enables imaging a thick sample with a constant, high transverse resolution over a long depth of focus. It also easily focuses the light beam on a targeted location to be imaged with the high resolution of Bessel beams, given the extension of the focusing range. We present a design for a 5mm outer diameter catheter that allows 360 degree scanning with a lateral resolution of about 5 microns across a depth of focus of about 1.6mm.

1.5 Dissertation Outline

The rest of the dissertation is organized in the following way: Chapter 2 summarizes the previous related work performed on dispersion compensation in OCT, which plays a critical role in achieving high axial resolution and describes advancements and achievements in research on endoscopic OCT imaging.

Chapter 3 describes the OCT systems developed. We first present a high axial resolution spectrometer-based FD-OCT developed with a broadband source that is a Ti:Sa sub-ten femtosecond laser. The developed system is applied to various applications and the images are then shown. Another developed swept source based FD-OCT is demonstrated with real time imaging of human skin. We also describe a novel system that we refer to as the dual-reference full-range FD OCT that enables doubling the imaging depth.

In Chapter 4, we study the application of Fourier domain optical delay line (FD-ODL) in OCT. We present a method to compensate overall system dispersion with a FD-ODL to keep the axial resolution determined by the coherence length of a broadband source.

In Chapter 5, we study the Bessel-beam-based confocal scanning optical microscopy (BCSOM) and apply it to frequency domain OCT to achieve high lateral resolution over long depth of focus.

Chapter 6 describes the design and fabrication of a catheter for endoscopic imaging.

In Chapter 7 the contribution of our research is summarized.

CHAPTER TWO: RELATED WORK

In this chapter, we review the previous research and advancements achieved in dispersion compensation methods in OCT and endoscopic OCT imaging.

2.1   Dispersion Compensation in OCT

Fiber-optic imaging interferometers configured for optical coherence tomography (OCT) have been developed to image backscattered light from biological tissues and other turbid materials accurately, rapidly, and noninvasively by exploiting the partial temporal coherence of a broadband light source [Huang, Swanson et al. 1991; Tearney, Bouma et al. 1996; Rollins, Kulkarni et al. 1998]. Because of the broadband nature of the light source used for OCT, dispersion is an important issue. Sources of dispersion include the fiber optics, the specimen, and other dispersive components in the interferometer. A dispersion mismatch between the interferometer arms affects the temporal width and shape of the interferometric signal formed by the low-coherence interferometer and consequently affects the longitudinal resolution of the imaging system. Therefore, balancing dispersion between the reference and the specimen arms in low-coherence interferometry is necessary to achieve the highest possible axial resolution throughout the imaging depth of the specimen. Similarly, in ultrafast lasers and in ultrafast measurement, dispersion compensation among the wavelengths is essential in order to preserve pulse durations and to achieve high time measurement resolutions [Brito-Cruz, Fork et al. 1987; Lemoff and Barty 1993].

There are two approaches to compensate dispersion: One is a post-imaging digital technique such as numerical dispersion compensation, the other is a pre-imaging optical technique. Within post-imaging compensation, numerical algorithms based on the fast Fourier transform [Marks, Oldenburg et al. 2003] or the numerical correlation of the depth scan signal with a depth variant kernel were presented for computationally correcting the effect of material dispersion on OCT signal data [Fercher, Hitzenberger et al. 2001]. An autofocus algorithm was also presented for rapid image correction [Marks, Oldenburg et al. 2003]. Recently, other numerical methods based on Fourier transform techniques were adopted to compensate dispersion in spectral domain OCT by correcting the frequency-dependent nonlinear phase of the received spectral OCT signal [Cense, Nassif et al. 2004; Leitgeb, Drexler et al. 2004; Wojtkowski, Srinivasan et al. 2004].

For any given material, the propagation constant $\beta(\omega)$ can be expanded as a Taylor series near the center frequency of the light source ω_0, as shown below:

$$\beta(\omega) = \beta(\omega_0) + \left.\frac{d\beta}{d\omega}\right|_{\omega_0} (\omega - \omega_0) + \frac{1}{2}\left.\frac{d^2\beta}{d\omega^2}\right|_{\omega_0} (\omega - \omega_0)^2 + \frac{1}{6}\left.\frac{d^3\beta}{d\omega^3}\right|_{\omega_0} (\omega - \omega_0)^3 + \ldots$$

(2.1)

The constant term $\beta(\omega_0)$ is the propagation constant at the center wavelength ω_0 of the spectral bandwidth, while the second term is the inverse group velocity. The third term describes the group velocity dispersion or a variation in group velocity with frequency. This is the term that produces pulse broadening in femtosecond optics and broadening of the axial resolution in OCT. The fourth term has been referred to as third-order dispersion, which produces asymmetric pulse distortion in femtosecond optics and asymmetric distortion of the point spread function in OCT.

Higher order terms may also be present. To remove the second order and higher order dispersions, a number of methods have been proposed. Fig. 2.1 shows a flowchart of the signal processing used in spectral domain OCT originally proposed by Wojtkowski and Fujimoto in 2004 [Wojtkowski, Srinivasan et al. 2004].   In this method the interference spectrum is first rescaled to convert from wavelength to frequency and then resampled. In standard spectral domain OCT, the spectrum is Fourier transformed to calculate the axial scan, which gives backreflection/backscattering versus distance (solid line). For dispersion compensation (dashed line), the Hilbert transform is used to calculate the complex representation of the input signal. The phase of this signal is modified by using adjustable second- and third-order terms.   The modified spectrum is Fourier transformed to calculate the axial scan. In order to perform automatic dispersion compensation, the sharpness of the axial scan or image is measured. The second- and third-order phase correction is iteratively adjusted to achieve optimum sharpness (dotted line). This procedure may be generalized to correct higher orders of dispersion.
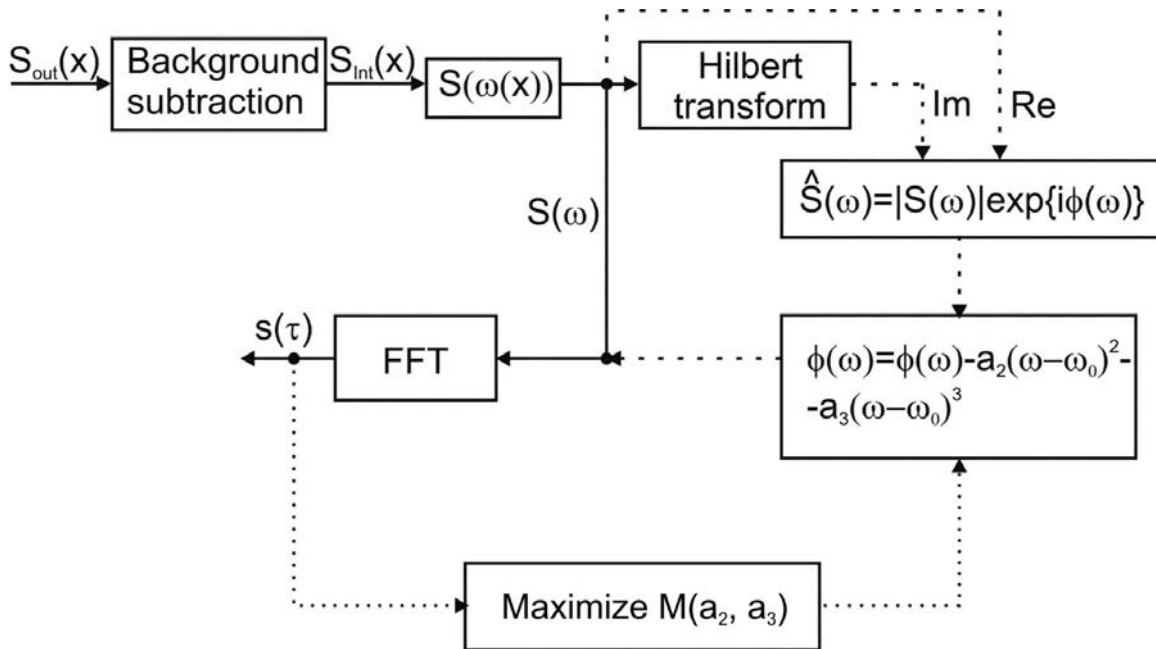
Figure 2.1 : Flow chart of spectral domain OCT dispersion compensation procedure.

Another method is used to determine the phase correction terms. The spectrum is Fourier transformed to *z*-space where it is shifted such that the coherence function is centered on the origin. A complex spectrum in *k*-space is obtained after an inverse Fourier transformation. The phase function of *k* is equal to the arctangent of the imaginary component divided by the real component. It indicates by how much subsequent wave numbers *k* are out of phase with each other. This function was fit to a polynomial expression of 9th order, yielding a set of coefficients. Individual spectra were first multiplied with the correction phase as determined from the last seven polynomial coefficients and then inverse Fourier transformed into A-lines, thus removing dispersion [Cense, Nassif et al. 2004].

Within pre-imaging compensation, optical dispersion balancing between the specimen and the reference arms is typically achieved by placing the same material in both arms as shown in Fig. 2.2, which was implemented by Boccara's group [Dubois, Vabre et al. 2002].

Dispersion compensation can be also achieved by adjusting dispersion using a dispersive optical element, such as a pair of prisms employed as a variable thickness dispersive plate in the reference arm as shown in Fig 2.3 [Maciejewski, Strakowski et al. 2006].
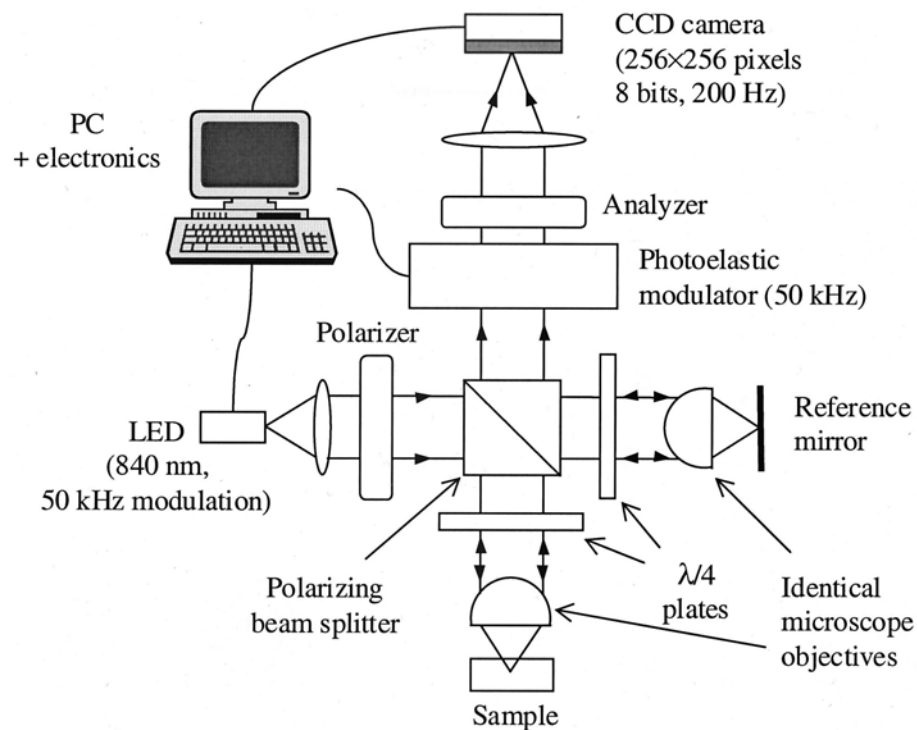
Figure 2.2 : Experiment setup for a full field OCT [Dubois, Vabre et al. 2002]
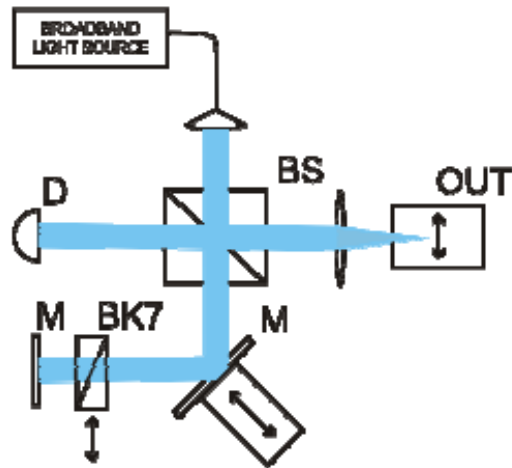
Figure 2.3 : Free-space OCT setup with mechanical dispersion compensation; BS -beamsplitter, M – mirrors, OUT – object under test, D – photodetector [Maciejewski, Strakowski et al. 2006]

A Fourier-domain optical delay line (FD-ODL) was first introduced for high-speed scanning in 1993 [Kwong, Yankelvich et al. 1993]. In 1993 FD-ODL was used for high speed scanning and dispersion compensation in TD OCT [Tearney, Bouma et al. 1997; Smith, Zvyagin et al. 2002]. A solution related to this approach is one of the primary topics in this dissertation. The potential assessment of dispersion in the sample was proposed [Niblack, Schenk et al. 2003]. Besides these methods, numerical and optical methods were have also been used together [Hsu, Sun et al. 2003] and an optimal center wavelength for the source was proposed at which the dispersion of water in tissue was minimized [Wang, Nelson et al. 2003].

2.2 Endoscopic OCT

Given the limitation of depth of penetration of a light beam in biological tissue, endoscopic probes are needed to image organs such as the lung, the stomach, the colon, and

arteries inside the body. After the first endoscopic applications of OCT in 1996, various types of endoscopic OCT were presented [Tearney, Boppart et al. 1996; Sergeev, Gelikonov et al. 1997; Bouma and Tearney 1999; Zara, Yazdanfar et al. 2003; Tran, Mukai et al. 2004].

The first endoscopic OCT adopting a catheter-endoscope is shown in Fig. 2.4. This implementation was reported to give 20 μm axial resolution and 38 μm lateral resolution. The outer diameter of the catheter is 1.1 mm. A new endoscopic probe was suggested by Tran in 2004 to eliminate the need to couple the rotational energy from the proximal to the distal end of the probe as shown in Fig. 2.5.
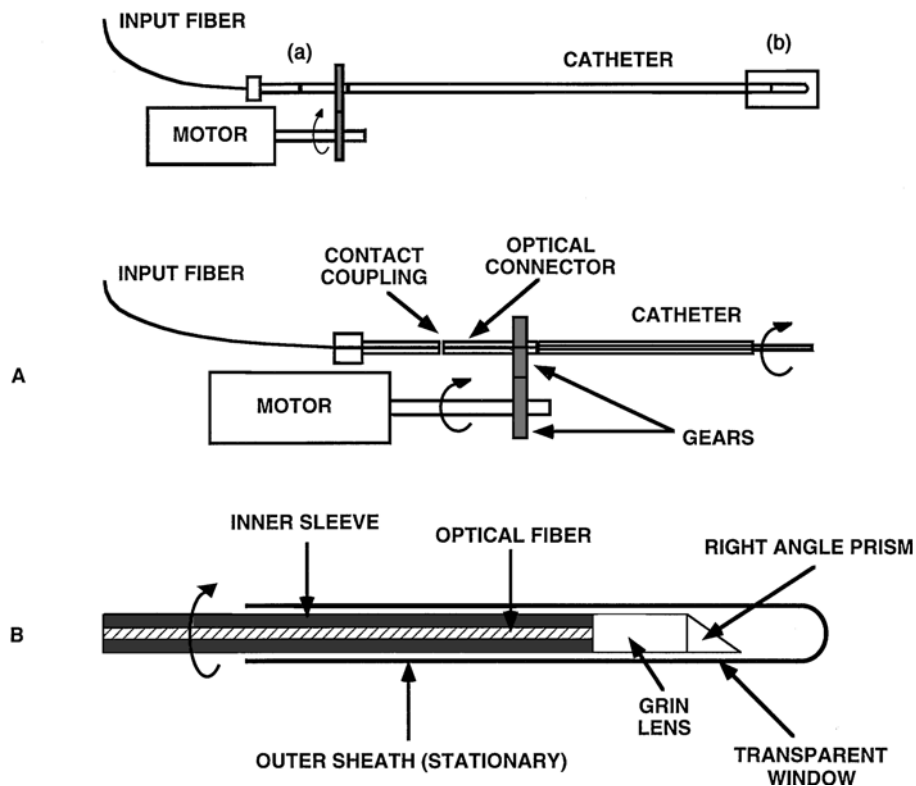
Figure 2.4 : Schematic of catheter–endoscope: A, Proximal end; B, Body and distal end.
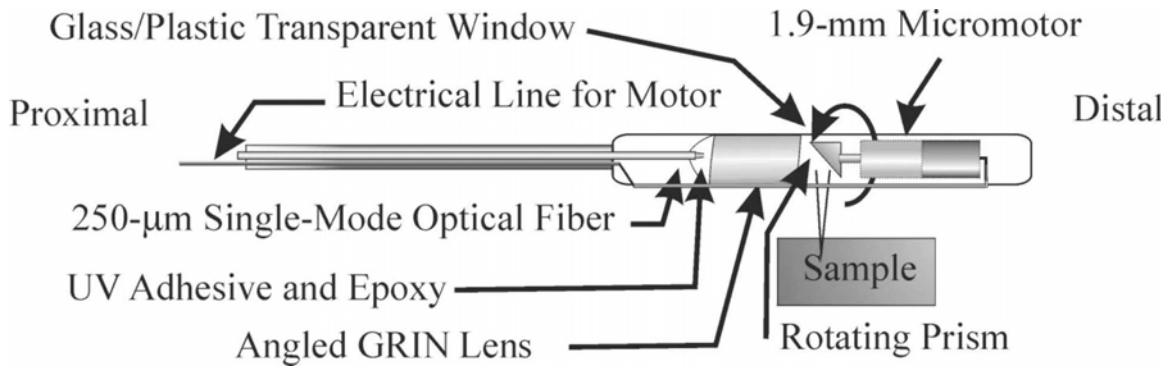
Figure 2.5 : Schematic of an endoscope probe.

Regardless of the scanning method, current endoscopic probes typically supply over 20μm lateral resolution. They are focused in the targeted location by pushing and pulling a wire outside the body, which is used to guide the catheter. High lateral resolution (i.e., < 5 μm) probes are typically achieved with high numerical aperture optics and Gaussian beam imaging which reduces the depth of focus (e.g., ~140 μm for ~5 μm lateral resolution at 800 nm). A fine focus adjustment is thus required that cannot be achieved by pushing and pulling a wire. High resolution endoscopic probes to-date use a mechanically adjustable catheter to change focal position in the tissue.

In Fig 2.6, MIT Fujimoto's group fabricated and demonstrated a distally actuated micromotor- based catheter in 2004 [Zara, Yazdanfar et al. 2003]. The fiber collimator and the focusing lens of the catheter are attached so that it enables the distal focus to be adjusted by translation of the fiber and lens assembly with respect to the fixed scanning motor at the distal end [Herz, Chen et al. 2004]. This system achieved an 8 μm lateral resolution over 4mm with C-

mode scanning. However, it requires that the focusing adjustment should be handled inside the catheter and multiple images with different focal planes must be acquired.
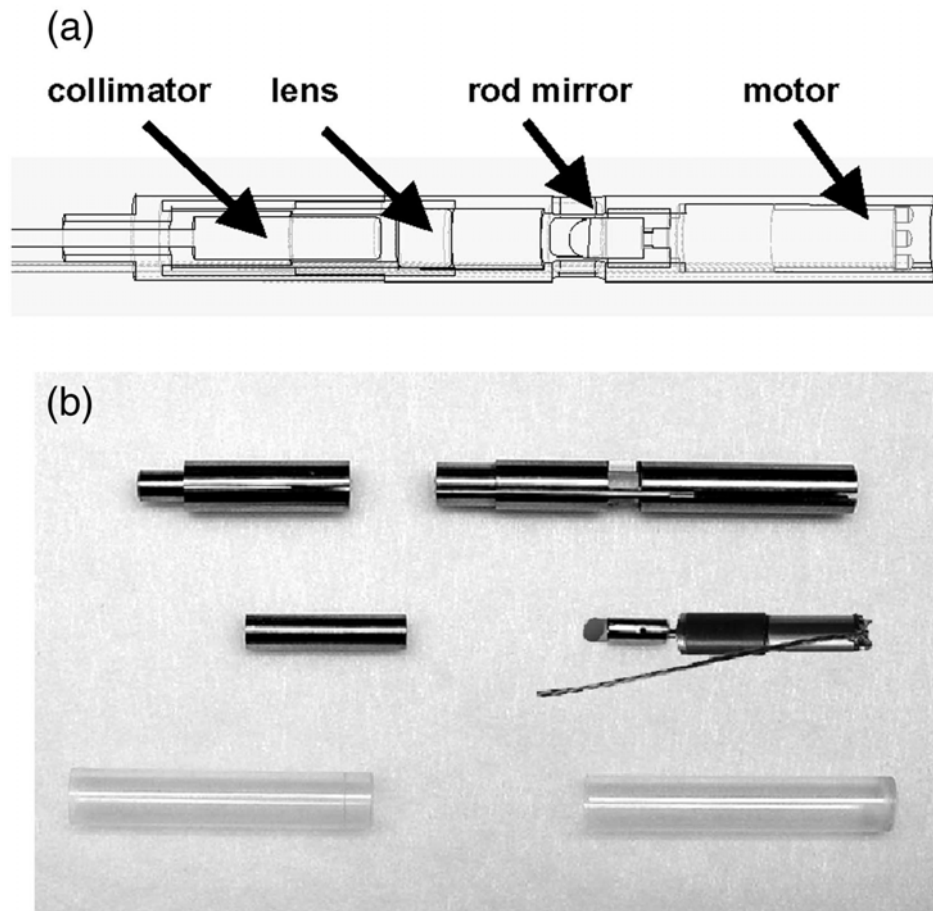
Figure 2.6 : Schematic and photograph of the distally actuated micromotor-based catheter assembly and components.

In Fig. 2.7, a GRIN lens rod based probe with dynamic focusing was presented to focus on a targeted location in a sample by moving a stage outside the body [Xie, Guo et al. 2006]. However the non-flexible rod limits some endoscopic applications.
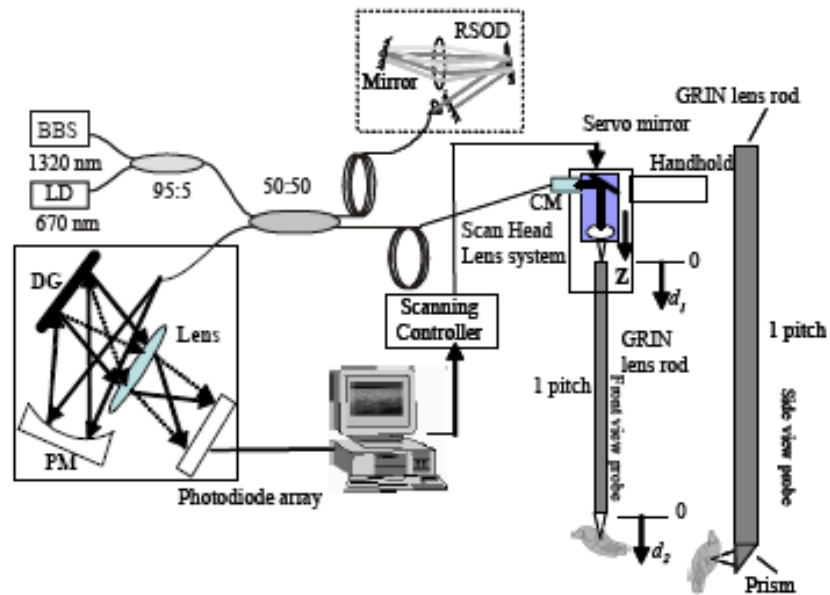
Figure 2.7 : Schematic diagram of a GRIN lens rod based dynamic focusing 2-D spectral domain optical coherence tomography system. PM: parabolic mirror; DG: diffractive grating; RSOD: rapid-scanning optical delay line for dispersion compensation.

Recently, an extended depth of focus imaging scheme using liquid lens technology has been investigated [Meemon, Murali et al. 2008; Murali, Lee et al. 2007]. The approach is currently limited by the physical size of the liquid lens 3mm. Liquid crystal lenses have also been attempted, however the speed of liquid crystal lenses is too slow to acquire high speed *in vivo* imaging [Wang, Ye et al. 2006]. Also, liquid crystal lenses require polarized light.

Bessel beam formation, generated by axicon optics, distinguishes itself from Gaussian beam formation in that it enables extension of the focusing range without loss of resolutions [McLeod 1954]. The trade-off however is light efficiency. In Fig. 2.8 Bessel beam illumination has been used to generate extended depth of focus in Spectral Domain Optical Coherence Tomography (SD OCT). Here the illumination was achieved using an axicon and the light was

collected via a beam splitter using a conventional objective to increase the light efficiency related to the system sensitivity for imaging in biological samples [Leitgeb, Villiger et al. 2006]. Researchers reported 1.5 μm resolution across a 200 μm depth of focus. A main drawback of this system is required to allow for another beam path for collecting the backscattered light limited the applications.
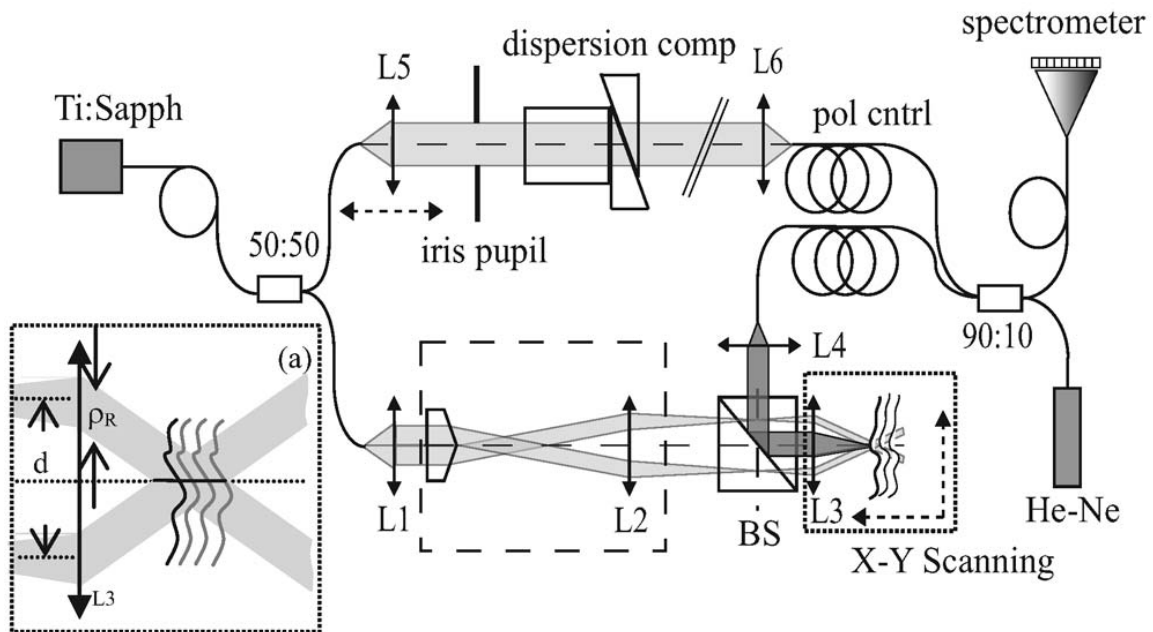
Fig. 2.8. Optical setup: L1–L6, lenses; BS, nonpolarizing beam splitter 50:50; He–Ne, helium–neon laser for adjustment; pol cntrl, polarization control. (a) Dark field illumination (light gray) and detection field (dark gray) at the sample position.

CHAPTER THREE: TWO HIGH RESOLUTION OCT SYSTEMS

3.1 High Axial Resolution Spectrometer Based FD OCT

In this chapter two OCT systems are described. The first system is a spectrometer-based FD OCT imager that achieved an axial resolution of ~2.5 μm using a Ti:Sa femtosecond laser with a 120nm bandwidth centered at 800nm. This system was used to image various biological samples including tadpoles, onions, and engineered alveolar tissues as well as 3D structures written in fused silica using a femtosecond laser. The reconstructed 3D images for each sample are presented with their own typical structure. The second system is a swept-source based FD OCT imager employing a high-speed Fourier-domain mode-locked (FDML) laser with a broadband spectral width (~156nm). The system achieved ~8 μm axial resolution. The real time imaging of human skin in the region of the finger tip was operated at an acquisition speed of 90,000 A-scans/sec. To accomplish the removal of mirror images inherent to the basic FD OCT image reconstruction algorithm, we invented, designed, and implemented a novel system referred to as the dual- reference full range FD OCT (DR FDOCT), which achieves the goal for extended imaging depth without a loss of acquisition speed. DR FDOCT is less sensitive to phase error generated by involuntary movements of the subject compared to the other established full range OCT systems because it uses two signals with phase difference of $\pi / 2$ obtained simultaneously from two reference arms respectively to remove mirror images.

3.1.1 FD-OCT system Configuration

A spectrometer-based fiber optic FD OCT system was developed as shown in Fig. 3.1. To achieve high axial resolution in the system, we integrated a high power, broadband femtosecond Ti:Sapphire laser source centered at 800nm with a spectral width 120 nm (FWHM), corresponding to ~2.4 μm axial resolution in air (Femtolasers Inc.) into the system. A spectrometer (HR 4000; Ocean Optics Inc.) images an optical bandwidth of 200nm on to a 3648 CCD pixel line array with a spectral resolution of 0.054 nm pixels corresponding to an axial measurement range of ~2 mm. A custom designed 80/20 fiber coupler benefited from the PTAP program funded by the National Science Foundation/Defense Advanced Research Projects Agency (NSF/DARPA) to support the broad bandwidth of the light source.

In the imaging path, 80% of the beam intensity from the fiber coupler is collimated within a 1.3 mm diameter beam (full width at $1/e^2$) and then focused by a 0.12 NA microscope objective installed into the sample arm of the OCT system. This configuration achieved a 6.5 μm transverse resolution about 5 μm into the tissue and a depth of focus that is ~ 100 μm in air. The remaining 20% of the beam intensity is used as a reference to be reflected by a mirror through a Fourier domain optical delay line (FD ODL) located in the reference arm to control the overall dispersion in the system. The details of the FD ODL will be discussed in Chapter 4. The polarization is adjusted to yield maximum signal modulation contrast.
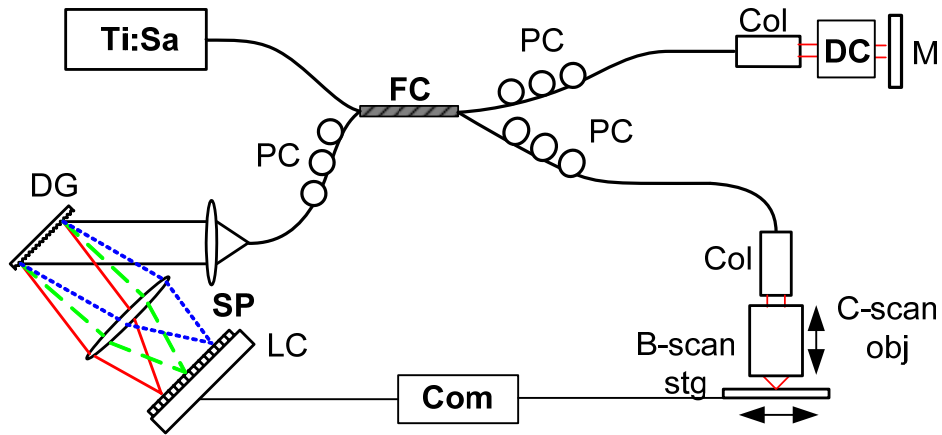
Figure 3.1 : A schematic diagram of the custom built OCM system. FC : fiber coupler, PC : polarization controller, Col : collimator, DC : dispersion compensation, DG : diffraction grating, LC : line CCD, SP : spectrometer, M : mirror, B-scan stg : automatically B-scan stg : automatically B-scanning translation stage, and C-scan obj : manually C-scanning objective

To verify the axial resolution of the system, we measured the axial point spread function (PSF) with a mirror in the sample arm located 0.1 mm away from the mirror in the reference arm. The PSF is shown in Fig. 3.2. The measured axial resolution is ~ 2.5 μm full width at half maximum (FWHM), versus a theoretical axial resolution of 2.4 μm.
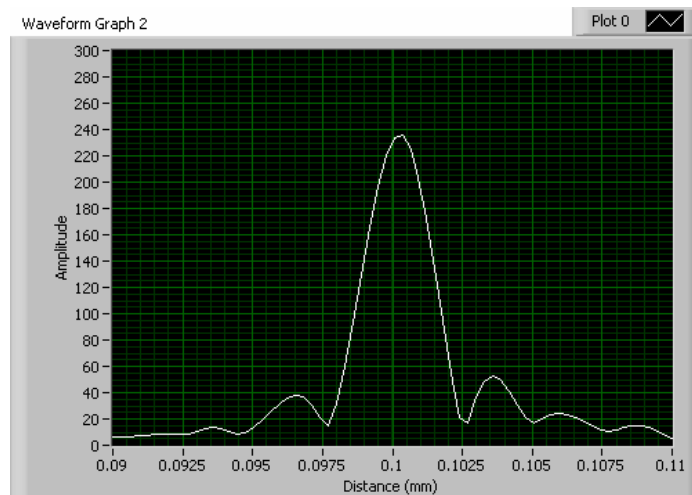
Figure 3.2 : Axial point spread function

3.1.2 Imaging of Various Samples with FD-OCT

3.1.2.1 Biological Samples (Tadpole and Onion)

Fig. 3.3 shows images of an African frog (*Xenopus laevis*) tadpole. Imaging was performed at a speed of one axial scan per 83 μs in a 1mm by 1mm region localized close to the gill structures (Fig.3.3b). The exposure time for one axial scan was 50 μs and the sensitivity was 97 dB for 5 mW of incident optical power. 3D data sets of 200 x-z images with 200 axial scans were collected in about 160 sec. The duty cycle of the system was therefore 1.25%. The data was displayed as shown in Fig. 3.3a. The x-y *en face* OCM images were reconstructed every 40 μm in depth from the top surface of the sample with a 1 mm x 1 mm field of view as shown in Fig. 3.3c. Images clearly show that planes outside the focus point (i.e. beam focused at depth corresponding to rows 2 and 3 in Fig.3.3c) lose lateral resolution.

(a)   (b)

(c)
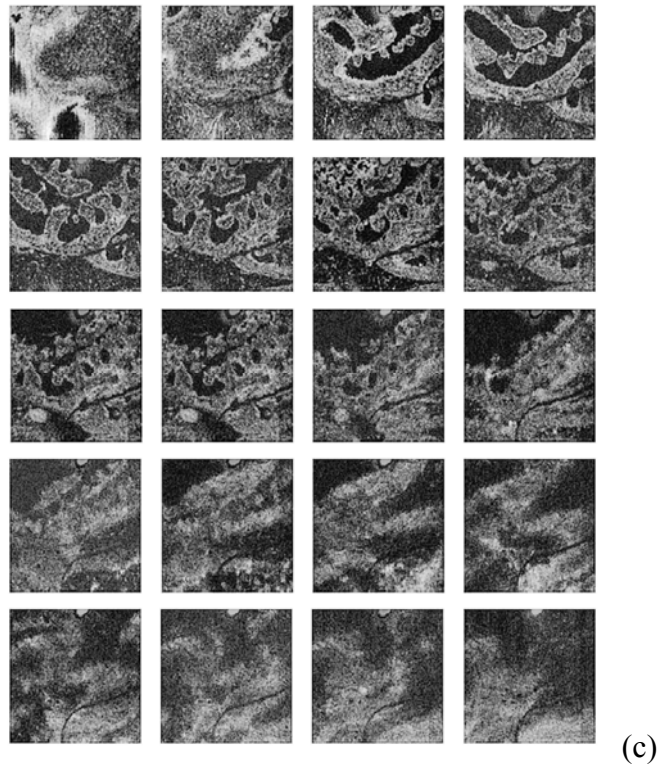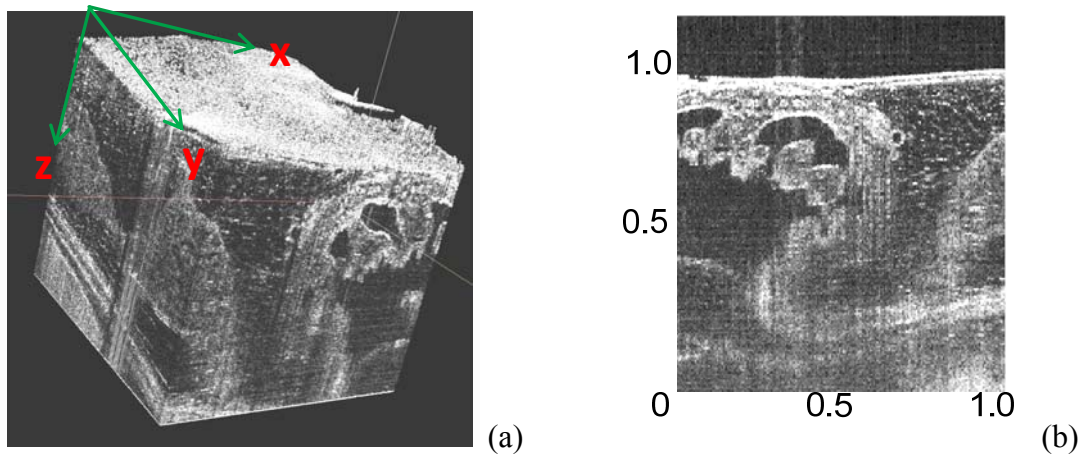
Figure 3.3 : (a) x-y-z 3D volume size=1mm^3 (b) 1 mm×1 mm x-z cross-sectional image (c). x-y *en face* OCM images acquired at every 40 μm depth with 1 mm×1 mm field of view. [Image acquired in ODALab, July 2007]

We also collected four tadpole images manually dynamic focused as shown in Fig. 3.4. using a microscope objective with 0.12 numerical aperture (NA) corresponding to a diffraction

limited lateral resolution of ~4.4μm and a depth of focus (DOF) as defined by the Rayleigh λ/4 criterion of ~40μm. The four images were taken at different focal planes with an approximately 120μm separation. The small depth of focus caused by the high numerical aperture results in image degradation outside of the focused zone, which is demonstrated in Fig. 3.4 a-d where the loss of resolution and contrast is distinctly visible as we move out of the depth-of-focus region of the objective. The four images (a-d) were then fused using a manual cut and stitching technique to create a single image shown in Fig. 3.4e with an extended depth. The Gabor domain has since been developed in our laboratory to automatically fuse the images [Rolland, 2008].
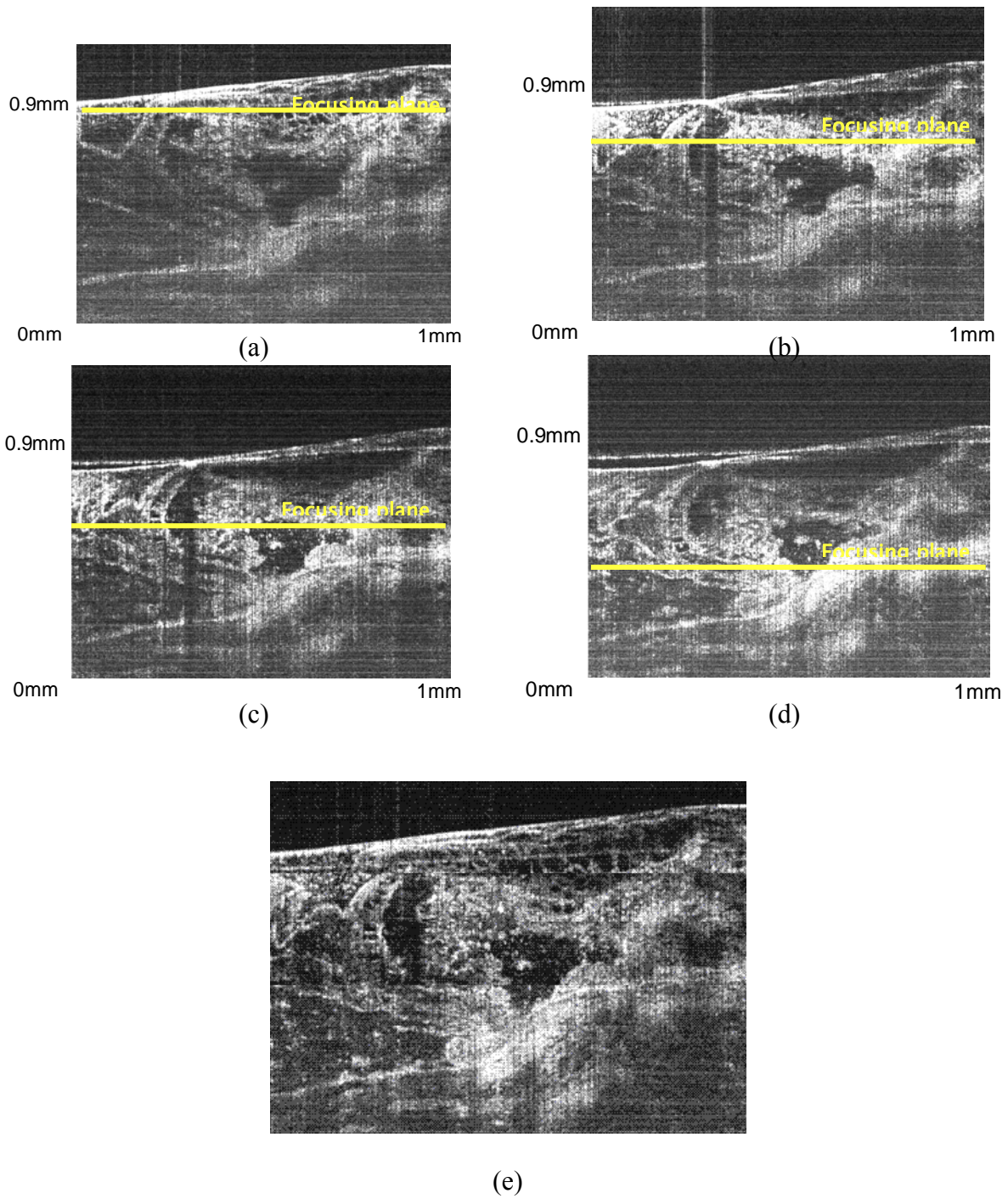
Figure 3.4 : (a) (b) (c) (d) four images taken at different focal planes with an approximately 120 μm separation. (e) A fused image with an extended depth using a manual cut and stitching technique. [Images acquired in ODALab, July 2007]

A piece of onion sample was scanned 1 mm laterally using a computer-controlled mechanically driven translation stage. The individual onion cells are easily resolved as shown in Fig. 3.5 because their cell size, usually ~100μm, is much larger than the lateral resolution of the objective throughout the imaging volume. 3D data sets of 200 x-z images with 200 axial scans were also collected. The two x-y *en face* onion images in different depth were then reconstructed with 1 mm x 1 mm field of view as shown in Fig. 3.6. The nuclei of onion cells are observed in Fig 3.6b.
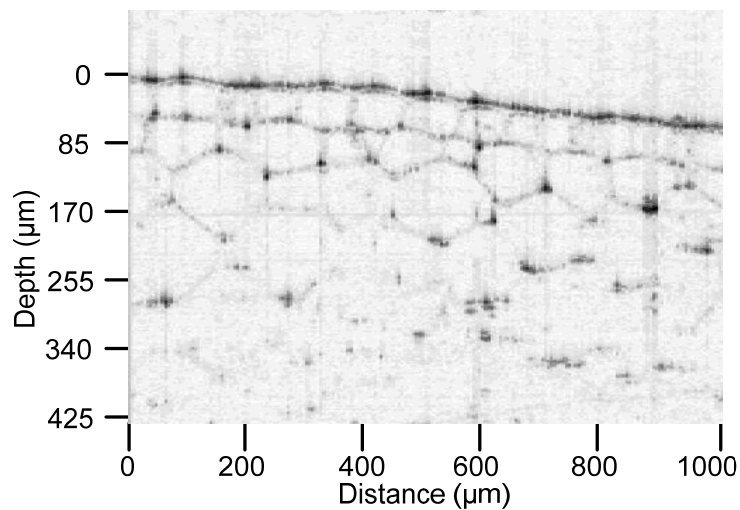
Figure 3.5 : OCT image of an onion sample [Images acquired in ODALab, August 2007]

<center>(a)   (b)</center>
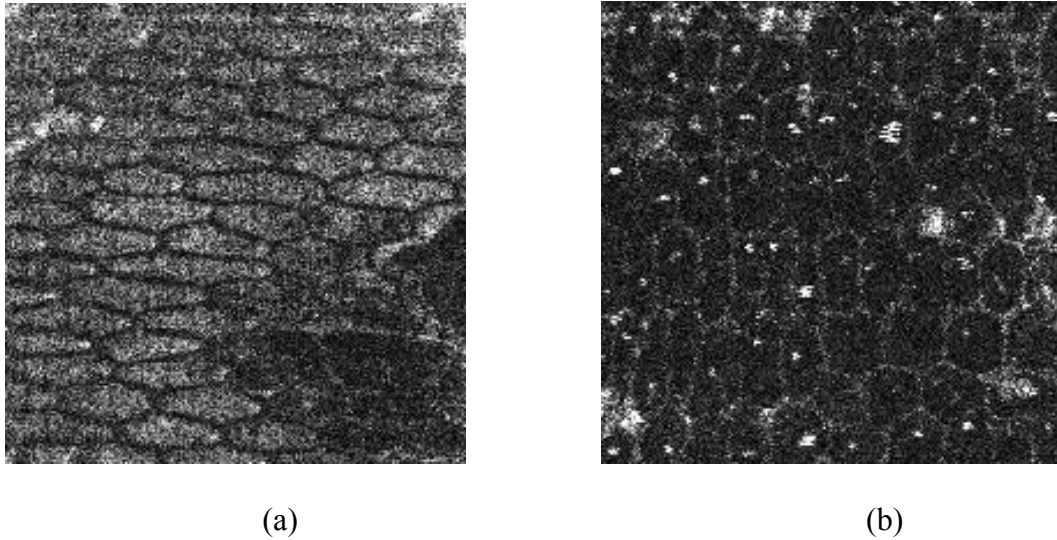
Figure 3.6 : Two x-y en face onion images in different depth with 1 mm x 1 mm field of view [Images acquired in ODALab, August 2007]

3.1.2.2 Engineered Alveolar Tissue

Engineered alveolar tissue was imaged with a 0.12 NA microscope objective integrated into the sample arm of the FD OCT system, achieving ~ 4 μm in transverse resolution with a depth of field of ~ 40 μm. The 3D dataset of 200 x-z images with 200 axial scans was collected by x-y scanning over a 200 μm by 200 μm region in the field of view. The x-y en face OCM images were then reconstructed. Fig. 3.7 shows the images of a bilayer cell sample that is composed of one epithelium and one endothelium layers and a membrane. Fig. 3.7(a) is a cross section (x-z) image of the sample using OCM and Fig.3.7(b) is a cross-sectional histology image using light microscopy as reference. The thickness of the epithelium, the endothelium, and the membrane were measured to be approx. 6μm, 4μm, and 12μm, respectively. The thicknesses were calculated based on a media index of 1.33 for the tissue and the refractive index of polyester 1.6 for the membrane. The top view (*en face*) images of the epithelium and

<center>49</center>

endothelium layers and the membrane were taken at about 4 μm below the surface in Fig.3.7(c), 8 μm below the surface in Fig.3.7(d), and 16 μm below the surface in Fig.3.7(e). Figure.3.7(e) shows a top view layer image in the middle of the membrane [Rolland, 2008].

(a) Cross section OCM image (b) Histology

(c) Epithelium layer (d) Endothelium layer (e) Middle of Membrane
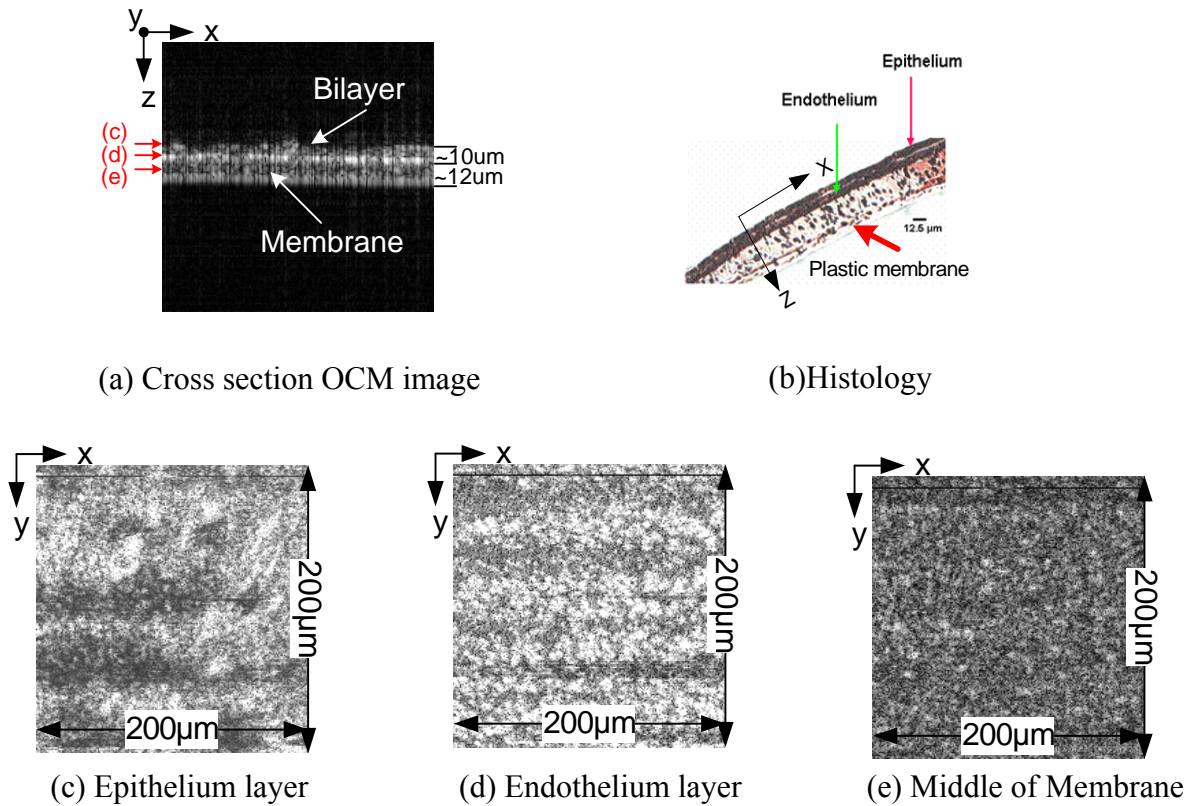
Figure 3.7 : Optical coherence microscopy (OCM) and light microscopy (LM) images of the bilayer alveolar tissue constructs: (a) A cross section OCM image where arrow "c" points to the epithelium, "d" endothelium and "e" membrane structures (b) cross-sectional histology image provided by VaxDesign Corporation; Top view (en face) OCM images of an (c) epithelium layer, (d) endothelium layer and (e) inside a membrane. The top view image size is 200 μm by 200 μm. [Images acquired in ODALab, March 2008]

3.1.2.3 Ti:Sa Femtosecond Laser Written 3D Structure

To be able to compare the images to a structure with known dimensions, a fused silica substrate was mounted on a 3D stage and translated perpendicular to the beam propagation to image photo-induced buried structures. The acquisition time was about 3 minutes for the spectra dataset for 200 x-z images, where 200 axial scans were collected for each sample set. The x-y end face OCM images were reconstructed over a 1000 μm × 1000 μm field of view by slicing the 3D data matrix in the x-y direction. In Fig. 3.8(a), a dark field optical microscope image illustrates the scattering centers created by the intense femtosecond irradiation over the damage threshold applied in Dr. Richardson group in CREOL, the College of Optics and Photonics at UCF. In Fig 3.8(b), the side view of the volumetric structure and its en face images, which were constructed as a function of depth from the surface, are shown in Fig 3.8(b).
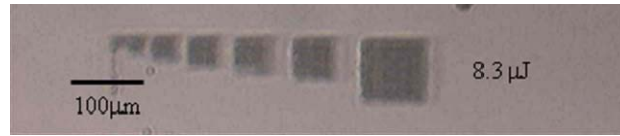
(a)
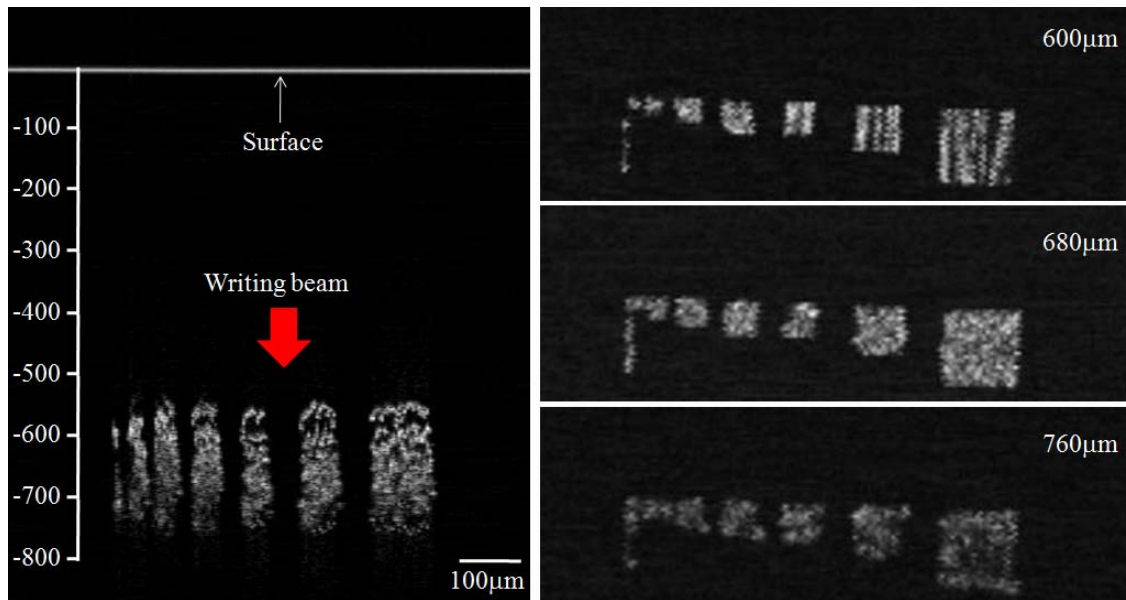
(b)

Figure 3.8 : (a) A dark field optical microscope image of the femtosecond laser written structures in fused silica and (b) side view of the first layer and top views acquired with OCM at 600 μm, 680 μm and 760 μm from the surface. The red arrow represents the direction of the writing beam from the surface. [Images acquired in ODALab, May 2008]

3.2 Swept Source based FD OCT

3.2.1   System Configuration

The schematic for a Fourier Domain Mode Locking (FDML) laser is shown in Fig. 3.9. The fiber Fabry-Perot tunable filter (FFP-TF) has a free spectral range (FSR) ~160 nm, a bandwidth (BW) ~0.2nm, and a loss (L) <2dB. This swept source is not a commercial product, it was co-developed by Micron Optics Inc. and our laboratory as part of PTAP program jointly funded by NSF/DARPA to yield the broader single semiconductor optical amplifier (SOA) centered at ~1300nm. The current FFP-TF design has a first-order electro-mechanical resonance near 45 KHz. Therefore the total fiber cavity length (including the fiber delay loop (Corning SMA28-e)) is designed for a length of ~4500 m. The semiconductor optical amplifier (SOA) has a peak gain of 32.9 dB at 1304 nm, a BW~46 nm, and a 3 dB saturation power Psat of ~12.4 dBm. The output coupling ratio of the fused coupler is 20%, which provides an average output power of 5.6 mW.
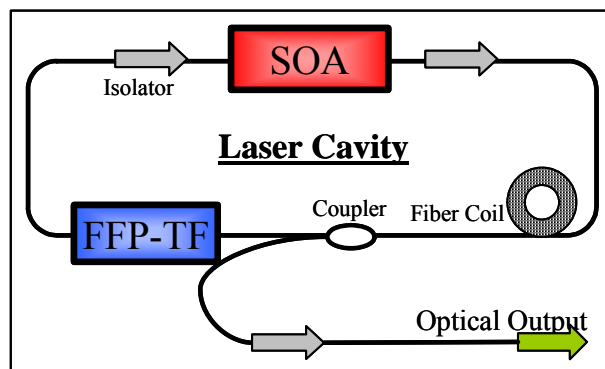
Figure 3.9 : A schematic of a FDML Laser [Courtesy of Micron Optics, Inc.]

Fig. 3.10 shows the power spectrum of the FDML laser measured with an optical spectrum analyzer (OSA) in 50 spectra average mode. The full-width at half-maximum (FWHM) was measured to be ~156 nm (from 1252.0nm ~ 1408.0nm). Fig. 3.11 shows two periods of the transient power profiles of the FDML for forward and backward frequency sweeps. The sweep frequency of the FFP-TF was 45 kHz as shown in the plot. Note that due to the sinusoidal drive waveform, the temporal sweep profile is distorted, with most of the spectral range compressed in the middle of the sweep profile.
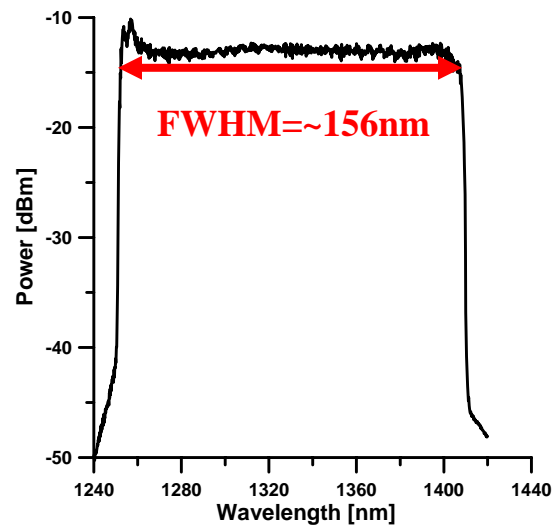
Figure 3.10 : Spectrum of the FDML laser measured with an OSA.
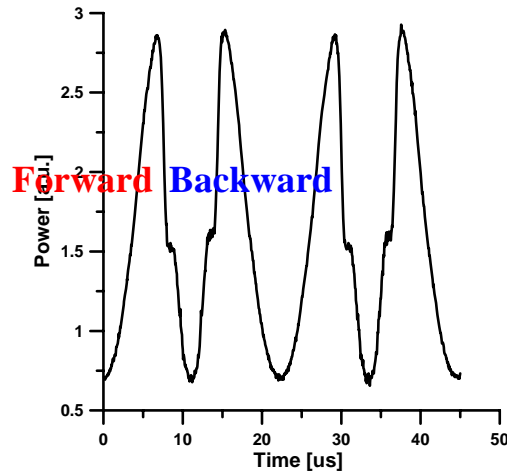
Figure 3.11 : Transient power profiles of the FDML.

Figure 3.12 is a schematic diagram of the swept source FD OCT system using the FDML laser. It consists of a 20:80 fiber coupler to send 80% of the light from the source to the sample through scanning optics and 20% to the reference arm with dispersion compensation optics. The reflected light from the mirror in the reference arm and the reflected or backscattered light from the sample are combined through a 50:50 fiber coupler in a dual-balanced detector via optical circulators. The photodiodes have a bandwidth of 80 MHz and a transimpedance gain of ~50,000 V/A. The interferometric fringe signals from the OCT interferometer were acquired on one channel of a two-channel, high-speed, 12-bit-resolution analog-to-digital converter (A/D) operating at 200 Msamples/s (National Instrument, Inc., model NI PCI 5124). 10% of the output power from the FDML laser was coupled into a fiber based Mach-Zehnder interferometer (MZI) with adjustable free space length in one of two arms. When the laser is frequency swept in time, the sweep frequency is not linear because the FFP-TF is controlled by a continuous sinusoidal wave signal. The peak and valley points of the sinusoidal interference fringes generated by the MZI were used to calibrate the interference signal. The calibrated points were selected from

indices of the peak and valley points of the MZI interference fringes, that were acquired on the other channel of the same A/D converter card. In the acquisition mode, the interference data for 400 sweeps of the FFP-TF at a sweep rate of 45 kHz were recorded onto the onboard memory of the A/D converter card. The data amount corresponds to 400 A-scans that form one frame. The acquisition speed was also synchronized with the mirror mounted on the galvanometer for 2D imaging as shown in Fig. 3.12. The signal processing such as the sampling calibration, zero padding to a length of 1024 samples, inverse Fourier transform, and log-scale 2D visualization were done after the onboard memory was read out to computer memory. The overall dispersion compensation in the system was controlled with a FD-ODL located in the reference arm. The polarization was adjusted to yield maximum signal modulation contrast with polarization controllers shown in Fig. 3.12.

The axial point spread functions (PSFs) derived from the broadband FDML laser source were measured and compared. The measured spectrum obtained with the optical spectrum analyzer (OSA) shown in Fig. 3.10 was first used to derive its PSF (blue dot line in Fig. 3.13) using an inverse Fourier transform. The PSF shows almost the same curve with the PSF (green dash dot line in Fig. 3.13) derived from the one period of the measured transient power profile shown in Fig. 3.11. The axial resolutions of both PSFs were 7 μm at FWHM. The spectrum of the reflected light from a single mirror in the sample arm of the OCT imaging setup shown in Fig. 3.12 was also measured and the corresponding axial PSF was obtained as shown by the red solid curve line in Fig. 3.13. The FWHM axial resolution was measured as 8 μm, which corresponds to ~6.2 μm in skin tissue. The spectrum of light from the source became narrower after passing

though the circulator, fiber coupler, and FD-ODL, which accounts for the small degradation of

the axial resolution from 7 to 8 μm.
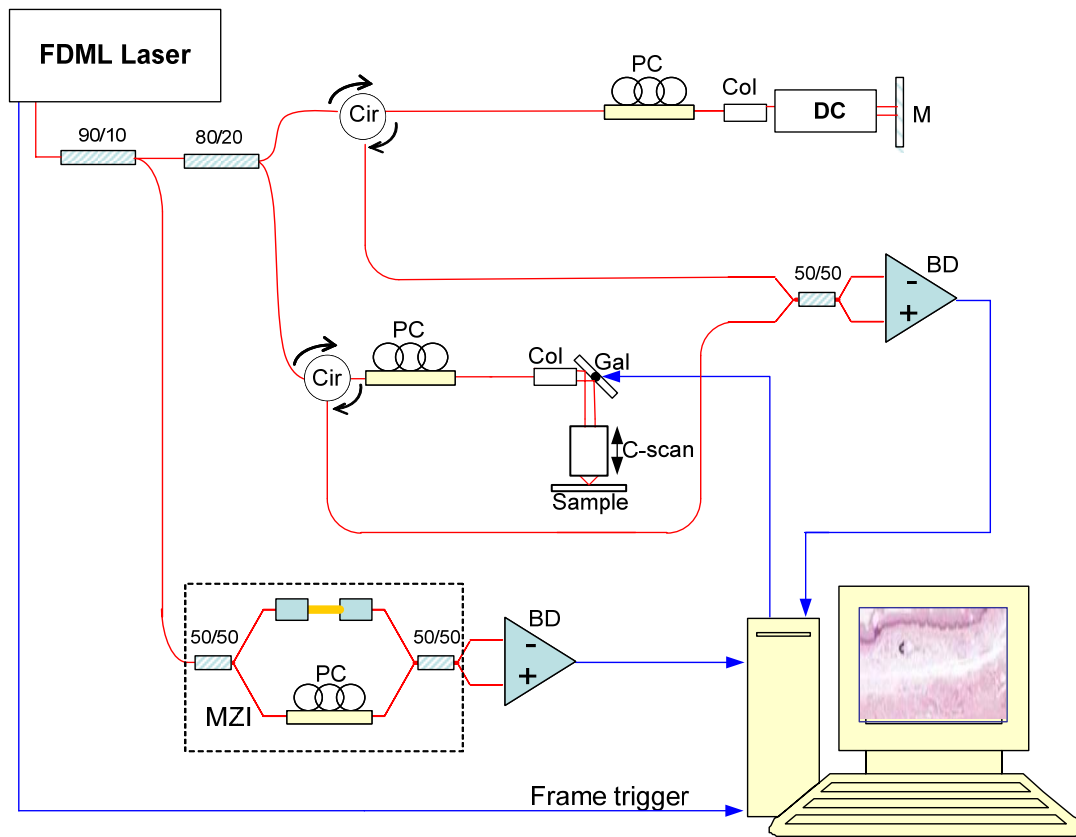
Figure 3.12 : A schematic diagram of the swept source based OCT system using the FDML laser. PC : polarization controller, Cir : optical circulator Col : collimator, DC : dispersion compensation, M : mirror, Gal : galvanometer, and BD : balance detector.
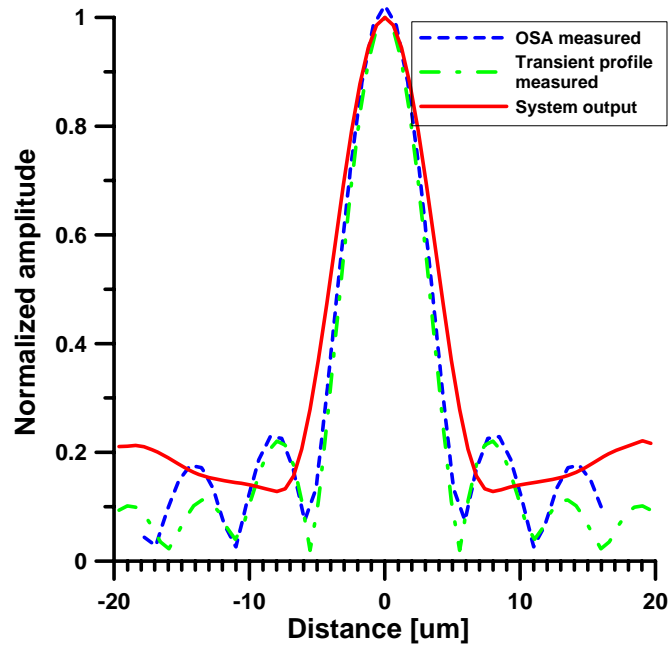
Figure 3.13 : Axial point spread functions based on different measured spectrums.

Sensitivities were measured at different depths with a mirror in the sample arm. The power incident on the sample reflector was 2.6 mW and the sweep rate was 45 kHz. The reflected power from the mirror was then attenuated by 40 dB. The signal to noise ratio (SNR) between the peaks of the PSF amplitude to the standard deviation of the noise floor was measured for each depth. The sensitivity values were then calculated by adding the SNRs and the attenuation ratio 40dB. The sensitivities for depths up to 2 mm are shown for 0.4 mm steps in Fig 3.14. The measured sensitivities were 102.0 dB, 101.7 dB, 95.1 dB, 91.4 dB, and 90.1 dB. The sensitivity decreased by 11.6 dB over a depth range of 2 mm.
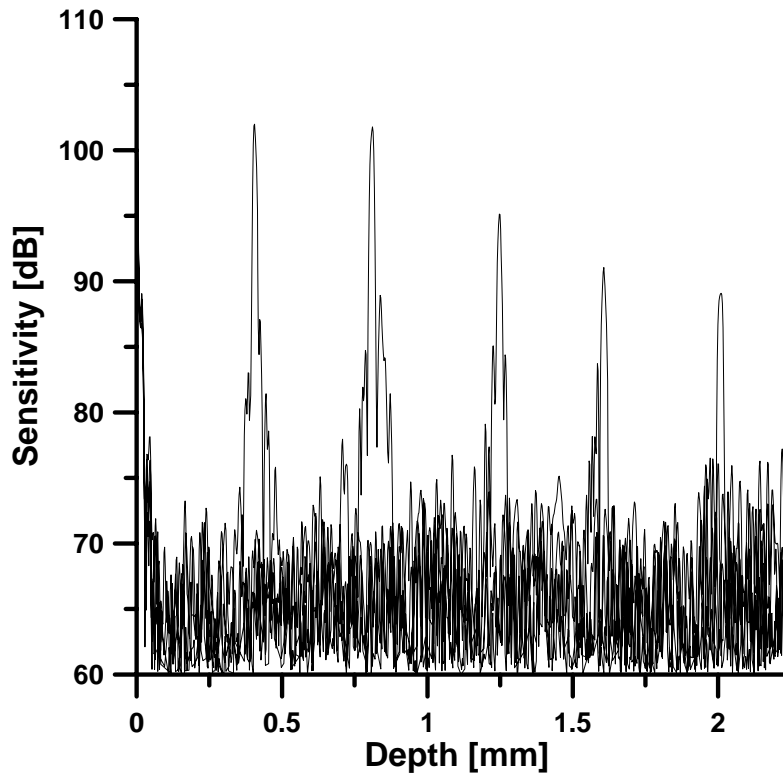
Figure 3.14 : Sensitivity as function of depths.

3.2.2 Imaging Result of Human Skin

The system was applied to imaging *in vivo* with human skin in the area of the finger tip. The multimedia file and an image are shown in Fig. 3.15 and Fig. 3.16, respectively. The focusing optics use a 25 mm focal length achromatic lens (Melles Griot Inc.) resulting in 0.04 numerical aperture (NA) with a 2mm diameter (full width at $1/e^2$) beam after the collimator in the sample arm in Fig. 3.12. It achieves 21 μm lateral resolution (FWHM) and has a 530 μm confocal parameter (i.e. two times Rayleigh range). Lateral scanning was performed using a gold mirror mounted on a galvanometer (VM 500, GSI Lumonics Inc.). Four hundred spectra were

acquired in 4.4 ms into the internal memory of the A/D card at a sampling speed of 200 Msamples/s. The data were used to form one frame using synchronized scanning with the acquisition process. The signal processing for real-time visualization of the acquired data was done before initiating acquiring new data for another frame. The real time imaging of the human finger tip at the speed of about 2 frames/s was directly recorded as shown in Fig. 3.15. The duty cycle of the system was about 1% (ratio between the acquisition time and the time corresponding to the acquisition of one frame in real time imaging). The delay came from the real time signal processing and the data transfer time from internal memory of the A/D card to the computer memory. The image-size of each frame is 400 transverse x 512 axial pixels. The OCT image acquired at 90,000 A-scans/sec clearly shows features such as the stratum corneum (SC), the dermal epidermal junction (DEJ), the epidermis (ED), sweat ducts (SD) in addition to a pattern of the finger print itself.
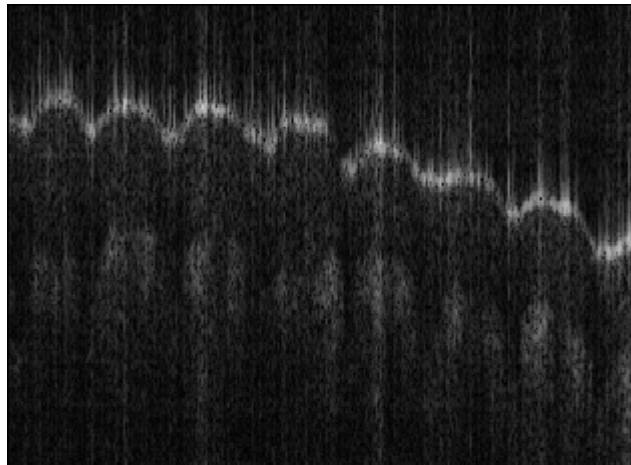
Figure 3.15 : Real-time swept-source-based FD-OCT recorded video clip of human finger *in vivo*. The image size of each frame is 1 mm by 2 mm and data were acquired in 4.4 ms for each frame, real-time displaying at the speed of 2 frames/s. [Images acquired in ODALab, Oct. 2008]
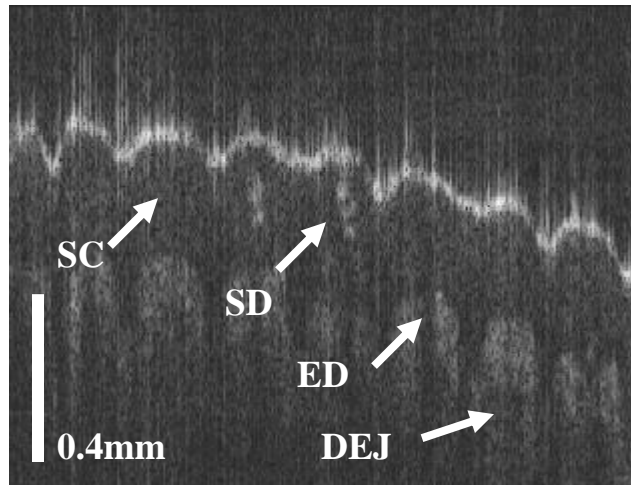
Figure 3.16 : Swept-source-based FD-OCT image of human finger tip [Images acquired in ODALab, Oct. 2008]

3.3 Dual Reference Full Range FD OCT (DR FROCT)

Fig. 3.17 is a schematic diagram of the dual reference full range FD-OCT system. It was developed as an extension of the system shown in Fig. 3.12 by adding another reference arm using another 50:50 fiber coupler after the 20:80 fiber coupler. The reflected light from the mirror in the added reference arm interferes with light reflected from the sample and is incident on another dual-balanced detector. The dual-balanced detector has the same specifications as the photodiode used in the system in Fig. 3.12. The two interferometric signals were acquired on each channel of a two-channel, high-speed, 12-bit-resolution analog-to-digital converter (A/D) operating at 200 Msamples/s (National Instrument, Inc., model NI PCI 5124). The MZI signal used for the calibration in the system in Fig. 3.12 was recorded on another 8-bit-resolution analog-to-digital converter (A/D) operating at 250 Msamples/s (National Instrument, Inc., model NI PCI 5114). We used a fiber stretcher using a ceramic piezo tube to introduce a $\pi/2$ phase shift

between two signals. The length of the fiber wound around the piezo tube was adjusted by a proportional-integral-derivative (PID) controller to maintain a constant fiber length change corresponding to a $\pi/2$ phase shift offsetting the environmental affects such as small temperature variation, and air flow. The phase difference at the central wavelength of the two signals was tracked in time and is shown in Fig. 3.18. The standard deviation was $\pi/10$.

To investigate the removal of the mirror image from the image with the developed DR-FROCT, we used a mirror (single interface) as a sample. The two interference signals each recorded on their own detector are shown in Fig. 3.19. One of the two signals in red has a $\pi/2$ phase difference compared to another interference signal in blue shown in Fig. 3.19(b). The amplitude and phase variations of the two interference signals were made identical using polarization controllers and FD-ODLs in the respective reference arms.
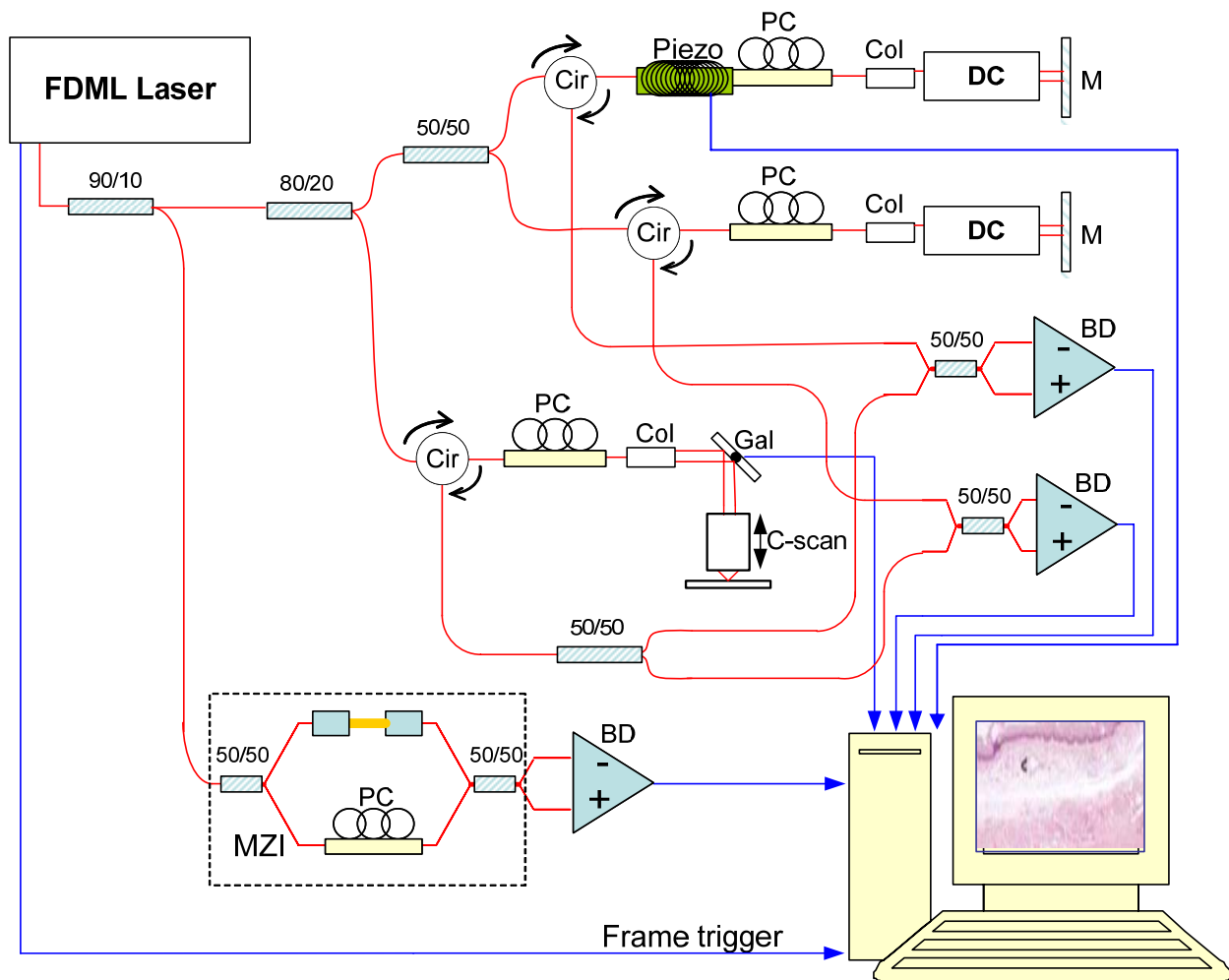
Figure 3.17 : A layout of the dual reference full range swept-source-based FD-OCT using the FDML laser. PC : polarization controller, Col : collimator, DC : dispersion compensation, M : mirror, Gal : Galvanometer, Cir : optical circulator, MZI : Mach-Zehnder interferometer, Piezo : Piezo tube fiber stretcher phase modulator, and BD : balance detector.
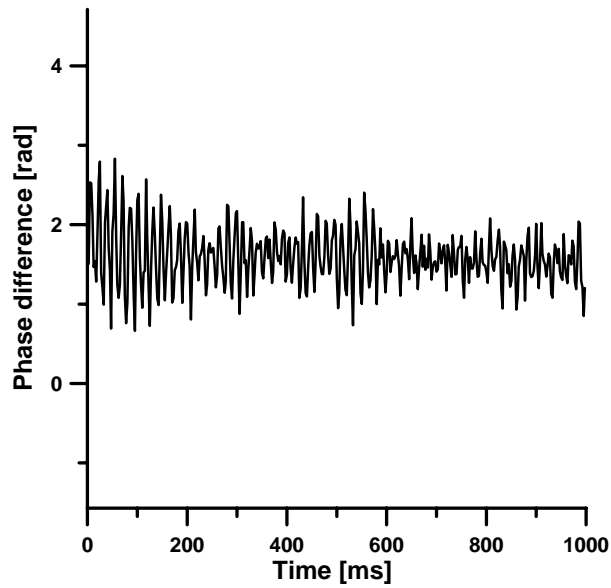
Figure 3.18 : Phase difference between the two signals at the central wavelength in B-scanning mode

(a)

(b)
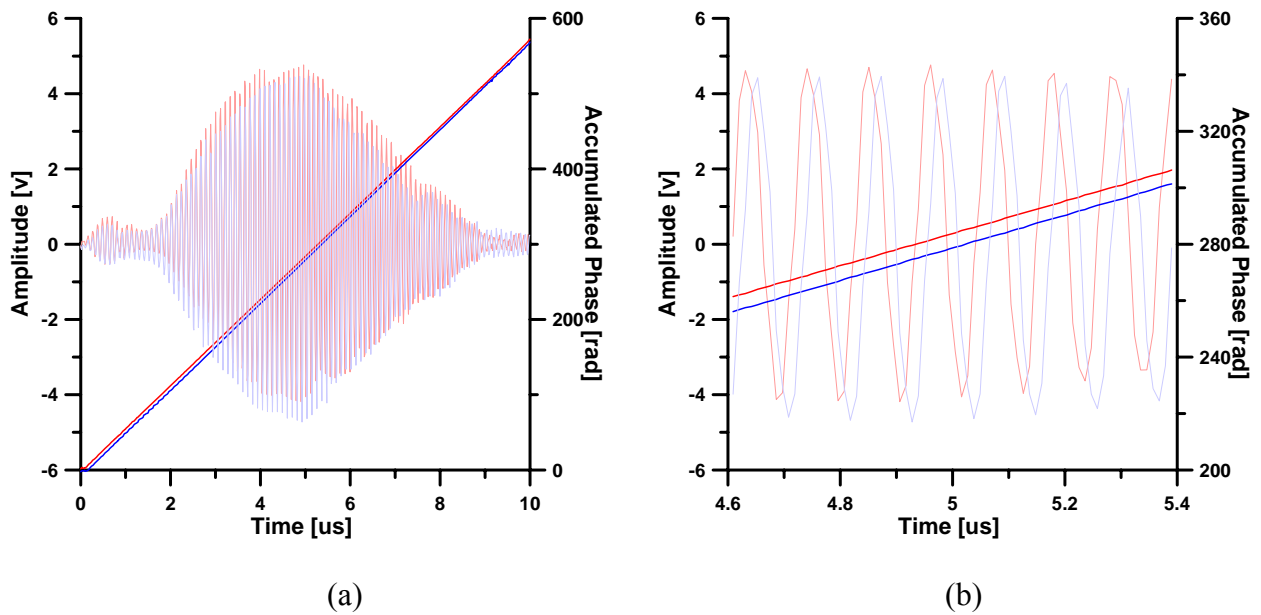
Figure 3.19 : (a) Two interference signals and their phase curves generated from the dual reference FD-OCT. (b) two zoom-in signals and the phase curves in the narrow time interval.

The modified two frame algorithm presented by Gotzinger was then used to remove the mirror image using the acquired two interference signals each having a $\pi/2$ phase difference [Gotzinger and *et al*, 2005]. First, a complex spectral signal $\widetilde{I}(\omega)$ was generated using the two acquired signals described by $I(\omega)$ and $I(\omega, \Delta\phi = \pi/2)$ respectively. It is given by

$$\widetilde{I}(\omega) = I(\omega) + iI(\omega, \Delta\phi = \pi/2). \tag{3.1}$$

$\widetilde{I}(\omega)$ and its complex conjugate $\widetilde{I}^*(\omega)$ were inverse Fourier transformed and are plotted in Fig. 3.20 (a) and (b), respectively. The inverse Fourier transform of $\widetilde{I}^*(\omega)$ was then subtracted from the inverse Fourier transform of $\widetilde{I}(\omega)$. The subtracted signals, presented in Fig. 3.20 (c), show that the real image lies in the positive side and the mirror image lies in the negative side. We finally multiply the signal with the Heaviside step function to obtain only the positive values corresponding to the real image as shown in Fig. 3.20 (d). Fig. 3.21 shows an OCT image of a single layer laterally scanned over 1mm after applying the mirror image removal algorithm. To emphasize the need for PID control, the phase difference was tracked in time without the PID control for comparison. The phase difference varies randomly as shown in Fig. 3.22. The OCT image of the single layer displays mirror image artifacts even though the mirror image removal algorithm was applied. Finally, DR-FDOCT was applied to a biological specimen (Garlic) and we achieved a full range OCT image as shown in Fig. 3.23.

In conclusion, DR-FDOCT system enables full range imaging without any loss of speed. Also, DR-FDOCT is less sensitive to phase error generated by involuntary movements of the subject compared to the other established full range OCT systems because it uses two signals

with phase difference of π/2 obtained simultaneously from two reference arms to remove mirror images. Importantly, it may be applied to Doppler FD OCT together with full range imaging.
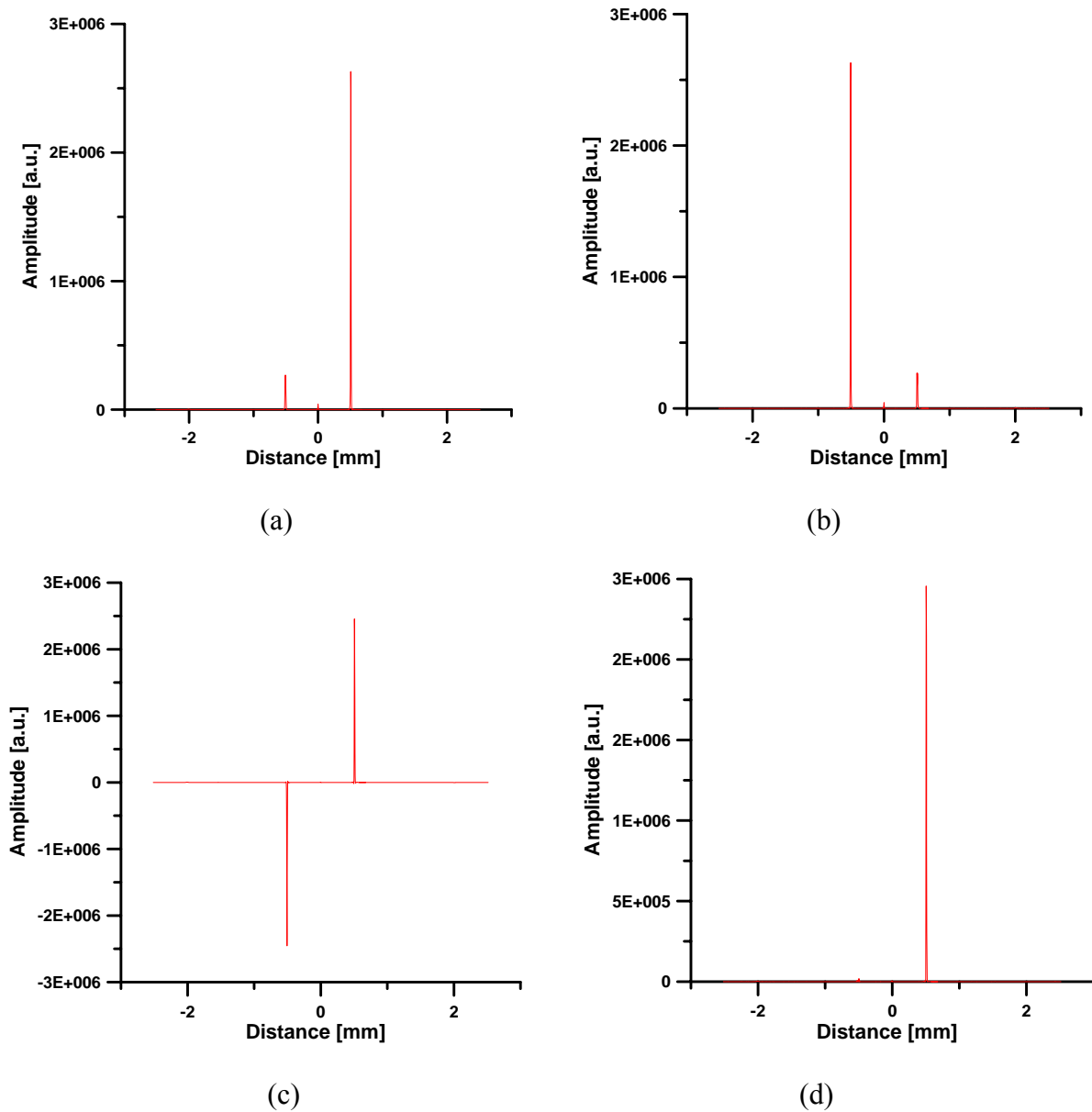
Figure 3.20 : (a) Fourier transform of the complex signal, (b) Fourier transform of the complex conjugate, (c) subtraction of the signal in (b) from the signal in (a), (d) the positive signal obtained after multiplying the signal in (c) with the Heaviside step function to get only positive values.
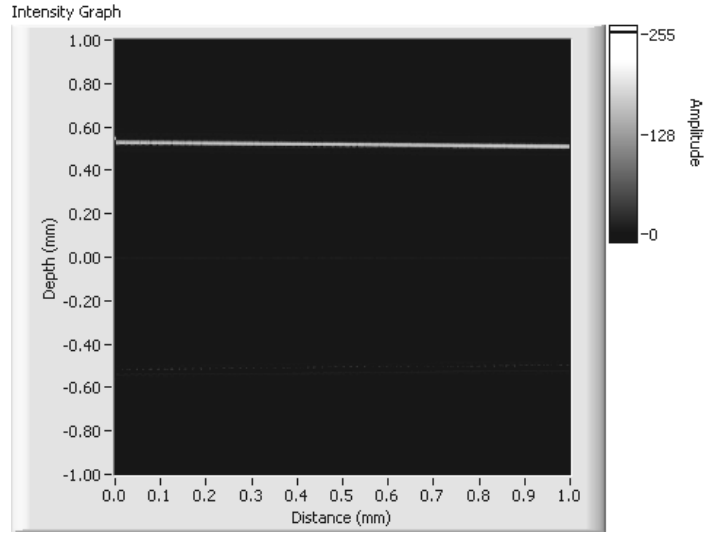
Figure 3.21 : OCT image of a single layer laterally scanned by 1 mm with the mirror image removal algorithm and PID control.
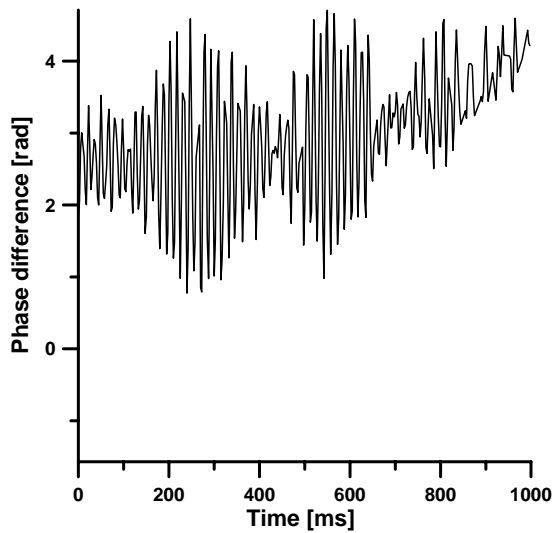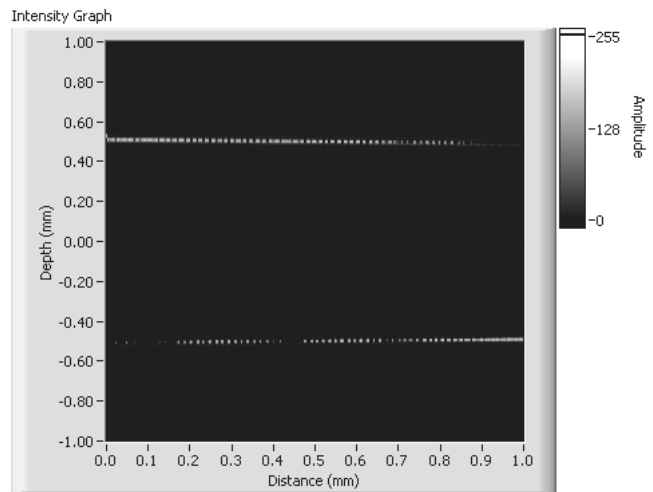
(a)   (b)

Figure 3.22 : (a) Phase difference between the two signals at the central wavelength in a B-scanning without PID control (b) OCT image of a single layer laterally scanned by 1mm with the mirror image removal algorithm but without PID control.
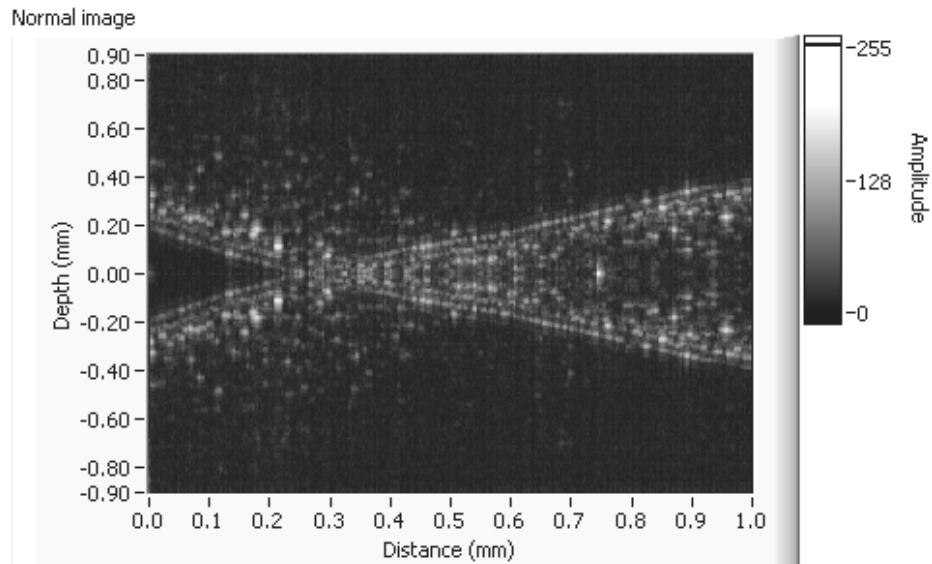
(a)
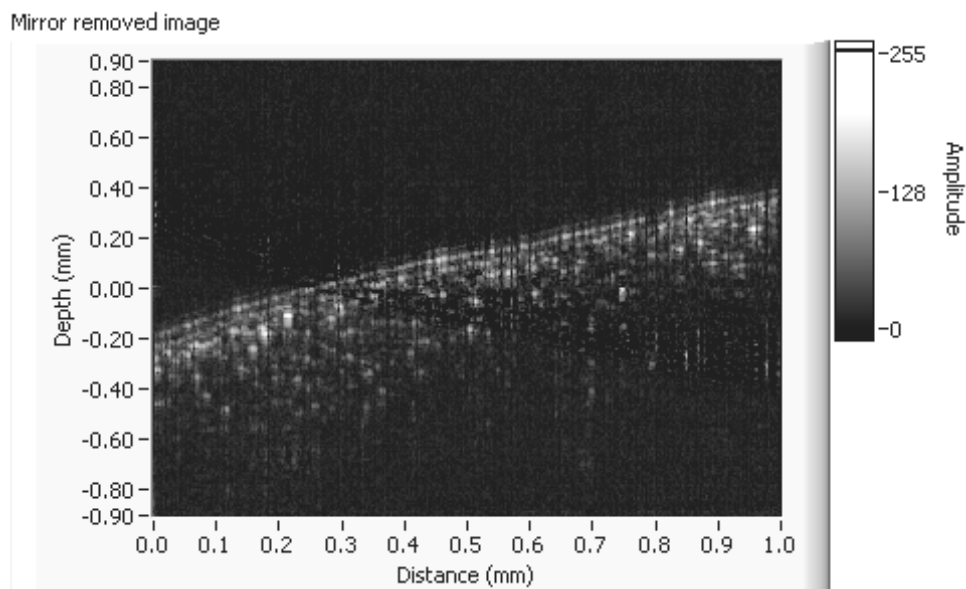
(b)

Figure 3.23 : Biological imaging (Garlic): (a) real image and mirror image overlapped OCT image using normal FD OCT system (b) mirror image removed OCT image using the DR FDOCT system

CHAPTER FOUR: DISPERSION COMPENSATION IN OCT USING FOURIER DOMAIN OPTICAL DELAY LINE

In this Chapter, we study the application of Fourier domain optical delay line (FD-ODL) in OCT. We demonstrate dispersion compensation with a FD-ODL. We demonstrate the impact of dispersion up to second-order in a fiber-optic interferometer that has the general structure of an optical coherence tomography (OCT) system. The dispersion effects induced by $LiTaO_3$ were included for validation with ground truth and its similarity of dispersion characteristics to skin specimens. We present a theoretical and associated experimental framework for minimizing broadening of the envelopes of the photocurrent signals observed across the depth of the specimen. We quantify how first-order dispersion in the overall system with a biological specimen can be compensated by employing an FD-ODL with a grating with a variable axial position. We also propose a dispersion compensation method that provides the highest overall axial resolution across the depth of the specimen. The method proposed is suitable for imaging a few millimeters into the specimen. When the overall first-order dispersion compensation is set for the photocurrent signal resulting from the light reflected from around the middle plane of the specimen, the impact of first-order dispersion on the photocurrent signal is minimized resulting in the highest resolution throughout the depth of the specimen. Figure 4.2 is a schematic diagram of an FD-ODL placed in the reference arm of the fiber optic interferometer. Here a collimated beam is incident on a diffraction grating and dispersed spatially. After passing through the lens, the light is then projected on a steerable mirror. The pivot point of the mirror may be offset from the optical axis by a distance x_0. The reflected, dispersed light is focused back onto the grating through the lens and then reflected by a double-pass mirror. The double-pass mirror returns the

light to the collimator through the same path. The dispersion introduced by the FD-ODL in the reference arm of the fiber optic interferometer can be controlled by the axial shift Δz of the grating from the focal plane of the lens. This shift is equivalent to introducing a defocus or equivalently a quadratic phase variation across the spectrum. Also the tilt angle θ_g of the grating normal with respect to optical axis of the FD-ODL can be used to compensate for dispersion [Zvyagin 2003]. Therefore, the grating axial shift and tilt angle have an effect on the axial point spread function (PSF), which is the envelope of the interferometric autocorrelation of the optical field reflected from the specimen and the optical field reflected from the reference mirror of the FD-ODL. Consequently, these parameters do impact the axial resolution.

4.1 Theory

In section 4.1.1, we derive the mathematical model of the photocurrent signal at the output of a fiber-optic imaging interferometer employing an FD-ODL in one arm and a specimen in the other arm. In section 4.1.2, the quantitative relation between the first-order dispersion effects of the FD ODL and the optical fiber is derived and then used to estimate the optical fiber length mismatch.

4.1.1   Mathematical Expression of the Photocurrent Signal in a Fiber-Optic Imaging

Interferometer with a FD-ODL

In order to represent the output signal of the system, we must first start with the input signal, which is the electric field emitted by the source. Given the broadband nature of the light source, it is desirable to express this field by its Fourier components as

$$\mathbf{E}_s(t) = \int_{-\infty}^{\infty} \exp(i\omega t)\hat{\mathbf{E}}_s(\omega)d\omega, \tag{4.1}$$

where the caret (^) denotes a function in the Fourier domain. Bold letters will denote vectors or matrices. Next, we may express the field at the detector in terms of the field at the source as

$$\mathbf{E}(t) = \int_{-\infty}^{\infty} \alpha_1 \exp[i\phi_1(\omega,t) + i\omega t]\hat{\mathbf{E}}_s(\omega)d\omega + \\ \int_{-\infty}^{\infty} \hat{\alpha}_2(\omega)\exp[i\phi_2(\omega,t) + i\omega t]\hat{\mathbf{E}}_s(\omega)d\omega, \tag{4.2}$$

where the first term is the electric field from the reference arm, and the second term is the electric field from the specimen. Because we use vector field theory, the expression given in Eq. (4.2) applies to any state of polarization. The term $\alpha_1 \exp[i\phi_1(\omega,t) + i\omega t]$ contains a real number α_1 that is the relative amplitude at the detector of the wave reflected from the mirror in the FD-ODL and the phase $\phi_1(\omega,t)$ that accounts for the optical path length to the mirror and the associated phase change along the path. We can use the FD-ODL in the reference arm to induce a phase change that is a function of frequency. The function $\hat{\alpha}_2(\omega)$ is the amplitude at the detector of the component of the wave backscattered from the specimen at the frequency ω and

is determined by the refractive index profile of the specimen. Finally, the term $\phi_2(\omega,t)$ accounts for the optical path length in the specimen arm and the associated phase changes caused for example by reflection, dispersion, and movement of the specimen among other possible effects. If we write

$$m(\omega,t) = \alpha_1 \exp[i\phi_1(\omega,t)] + \hat{\alpha}_2(\omega)\exp[i\phi_2(\omega,t)], \tag{4.3}$$

then we have

$$\mathbf{E}(t) = \int_{-\infty}^{\infty} m(\omega,t)\exp(i\omega t)\hat{\mathbf{E}}_s(\omega)d\omega. \tag{4.4}$$

In this expression, both $\mathbf{E}(t)$ and $\hat{\mathbf{E}}_s(\omega)$ are stochastic processes. Because of its broadband nature, we assume that the source field $\mathbf{E}_s(t)$ obeys circular Gaussian statistics [Barrett 2004]. This assumption implies that $\mathbf{E}(t)$ is also a Gaussian random process. In particular, the mean source field satisfies

$$\langle \mathbf{E}_s(t) \rangle = 0,$$

which implies that

$$\langle \mathbf{E}(t) \rangle = 0.$$

Given that the detector has an integration time of Δt, the detected photocurrent is given by

$$I(t) = \frac{e}{\Delta t}\int_{t-\Delta t}^{t} N(t')dt' = \frac{e}{\Delta t}\int_{-\infty}^{\infty} r(t-t')N(t')dt', \tag{4.5}$$

72

where e is the electron charge, and $r(t)$ denotes the time integration window of the detector, which is given by

$$r(t) = \begin{matrix} 1 \text{ for } 0 \le t \le \Delta t \\ 0 \text{ otherwise} \end{matrix} . \tag{4.6}$$

In this integral, $N(t)$ is a doubly stochastic Poisson random process representing the photoelectrons produced by the field impinging on the detector. Its mean is given by

$$\langle\langle N(t) \rangle\rangle = \rho \langle \mathbf{E}^\dagger(t) \mathbf{E}(t) \rangle, \tag{4.7}$$

where ρ is proportional to the detector responsivity and area and the double angle brackets are used to indicate statistical averages over the two sources of randomness associated with the source and the detection process, respectively. Therefore, the mean current is given by

$$\langle\langle I(t) \rangle\rangle = \frac{e}{\Delta t} \int_{-\infty}^{\infty} r(t - t') \langle\langle N(t') \rangle\rangle \, dt'. \tag{4.8}$$

The expectation in the integrand is given by

$$\langle\langle N(t') \rangle\rangle = \rho \int_{-\infty}^{\infty} \int_{-\infty}^{\infty} m^*(\omega, t') m(\omega', t') \exp[i(\omega' - \omega)t'] \langle \hat{\mathbf{E}}_s^\dagger(\omega) \hat{\mathbf{E}}_s(\omega') \rangle \, d\omega d\omega'. \tag{4.9}$$

We will assume that the source field is a stationary random process and we define the scalar autocovariance function of the source field as

$$G(\tau) = \left\langle \mathbf{E}_s^\dagger(t - \tau)\mathbf{E}_s(t)\right\rangle, \tag{4.10}$$

The stationarity assumption is related to the stability of the source. This assumption may be relaxed to quasi-stationarity in order to account for other sources of variation in the source field. The scalar autocovariance function has the property that

$$G^*(\tau) = G(-\tau) \quad, \tag{4.11}$$

which ensures that the Fourier transform $\hat{G}(\omega)$ is real. The expectation $\left\langle \hat{\mathbf{E}}^\dagger{}_s(\omega)\hat{\mathbf{E}}_s(\omega')\right\rangle$ from (4.9) may be expressed by means of the inverse Fourier transform as

$$
\begin{aligned}
\left\langle \hat{\mathbf{E}}_s^\dagger(\omega)\hat{\mathbf{E}}_s(\omega')\right\rangle &= \frac{1}{4\pi^2}\int_{-\infty}^\infty\int_{-\infty}^\infty \exp\!\left[-i(\omega't_2 - \omega t_1)\right]\!\left\langle \mathbf{E}_s^\dagger(t_1)\mathbf{E}_s(t_2)\right\rangle dt_1 dt_2 \\
&= \frac{1}{4\pi^2}\int_{-\infty}^\infty\int_{-\infty}^\infty \exp\!\left[-i(\omega't_2 - \omega t_1)\right]G(t_2 - t_1)\,dt_1 dt_2.
\end{aligned}
\tag{4.12}
$$

By using

$$\omega't_2 - \omega t_1 = \frac{1}{2}(\omega' - \omega)(t_2 + t_1) + \frac{1}{2}(\omega' + \omega)(t_2 - t_1) \quad, \tag{4.13}$$

and performing a change of variable with s equal t_2-t_1, we can reduce Eq. (4.12) to

$$\left\langle \hat{\mathbf{E}}_s^\dagger(\omega)\hat{\mathbf{E}}_s(\omega')\right\rangle = \frac{1}{2\pi}\delta(\omega' - \omega)\int_{-\infty}^\infty \exp\!\left[-i\frac{(\omega' + \omega)}{2}s\right]G(s)\,ds = \delta(\omega' - \omega)\hat{G}(\omega). \tag{4.14}$$

Hereafter, $\hat{G}(\omega)$ will be represented as $S(\omega)$, which is the power spectral density of the source.

Inserting $\left\langle \hat{\mathbf{E}}_s^\dagger(\omega)\hat{\mathbf{E}}_s(\omega') \right\rangle$ into Eq. (4.9) yields

$$\left\langle\left\langle N(t') \right\rangle\right\rangle = \rho \int_{-\infty}^{\infty} \left| m(\omega,t') \right|^2 S(\omega) d\omega. \tag{4.15}$$

In the integrand we have

$$\left| m(\omega,t') \right|^2 = \alpha_1^2 + \left| \hat{\alpha}_2(\omega) \right|^2 + 2\alpha_1 \, \mathrm{Re}\{\hat{\alpha}_2(\omega)\exp[-i\phi_1(\omega,t')+i\phi_2(\omega,t')]\}. \tag{4.16}$$

The last term is the interference term, which is usually the term of interest. Combining Eq. (4.15) and Eq. (4.8) further yields

$$\left\langle\left\langle I(t) \right\rangle\right\rangle = \frac{\rho e}{\Delta t} \int_{-\infty}^{\infty} r(t-t')\left[\int_{-\infty}^{\infty} \left| m(\omega,t') \right|^2 S(\omega) d\omega \right] dt'. \tag{4.17}$$

If we assume that the response time of the detector is instantaneous, i.e. $r(t-t')=\delta(t-t')$, Eq. (4.17) simplifies to

$$\left\langle\left\langle I(t) \right\rangle\right\rangle = \frac{\rho e}{\Delta t} \int_{-\infty}^{\infty} \left| m(\omega,t) \right|^2 S(\omega) d\omega. \tag{4.18}$$

To isolate and quantify the interaction of fiber dispersion and the FD ODL, we model the specimen as a mirror. We then introduce the effect of the biological specimen into the model. With the mirror as the specimen, $\hat{\alpha}_2(\omega)$ can be replaced by α_2, and Eq. (4.16) may be written as

$$\left| m(\omega,t) \right|^2 = \alpha_1^2 + \alpha_2^2 + 2\alpha_1\alpha_2 \, \mathrm{Re}\{\exp[-i\phi_1(\omega,t)+i\phi_2(\omega,t)]\}. \tag{4.19}$$

Filtering out the dc term of the photocurrent signal, the remaining ac term representing the interference may be written as

$$\langle\langle I_{ac}(t)\rangle\rangle \propto \int_{-\infty}^{\infty} \text{Re}\{\exp i[\phi_2(\omega,t) - \phi_1(\omega,t)]\}S(\omega)d\omega$$

$$\propto \int_{-\infty}^{\infty} \text{Re}[\exp i\Delta\phi(\omega,t)]S(\omega)d\omega,$$

(4.20)

The phase difference $\Delta\phi(\omega,t)$ can be expanded as a Taylor series as follows

$$\Delta\phi(\omega,t) = \phi_2(\omega,t) - \phi_1(\omega,t)$$

$$= \omega_0 t_p(t) + (\omega - \omega_0)t_g(t) + D_\omega(t)\frac{(\omega - \omega_0)^2}{2!} + D_\omega^{(1)}(t)\frac{(\omega - \omega_0)^3}{3!},$$

(4.21)

where ω_0 is the center frequency of the light source, $t_p(t)$ is the phase delay, $t_g(t)$ is the group delay, $D_\omega(t)$ is the first-order group delay dispersion, and $D_\omega^{(1)}(t)$ is the second-order group delay dispersion. Furthermore each parameter can be further defined as

$$t_p(t) \equiv \Delta\phi(\omega_0,t)/\omega_0,$$

$$t_g(t) \equiv \partial[\Delta\phi(\omega,t)]/\partial\omega\,|_{\omega=\omega_0},$$

$$D_\omega(t) \equiv \partial^2[\Delta\phi(\omega,t)]/\partial\omega^2\,|_{\omega=\omega_0},$$

$$D_\omega^{(1)}(t) \equiv \partial^3[\Delta\phi(\omega,t)]/\partial\omega^3\,|_{\omega=\omega_0}.$$

(4.22)

Substituting Eq. (4.21) into Eq. (4.20), $\langle\langle I_{ac}(t)\rangle\rangle$ may be expressed as

$$\left\langle\left\langle I_{ac}(t)\right\rangle\right\rangle \propto \text{Re}\left[\begin{array}{l}\int\limits_{-\infty}^{\infty} S(\omega-\omega_0)\exp[i(D_\omega\frac{(\omega-\omega_0)^2}{2!}+D_\omega^{(1)}\frac{(\omega-\omega_0)^3}{3!})]\\ \times\exp(i\omega_0 t_p)\exp[i(\omega-\omega_0)t_g]d\omega\end{array}\right], \qquad (4.23)$$

where $S(\omega-\omega_0)$ is the source power spectral density centered at ω_0. It can be observed that Eq. (4.23) is the inverse Fourier transform of the frequency-domain function given by

$$\hat{I}_{ac}(\omega') \propto S(\omega')\exp[i(D_\omega\frac{\omega'^2}{2!}+D_\omega^{(1)}\frac{\omega'^3}{3!})]\exp(i\omega_0 t_p), \qquad (4.24)$$

where $\omega'=\omega-\omega_0$. It may be noted that for the first-order group delay dispersion, the dependence of the phase difference is quadratic in ω', corresponding to defocus. We shall now apply Eq. (4.24) to the fiber optic interferometer with an FD-ODL in the reference arm. We first need, however, to establish some expressions for the phase and group delays, as well as the first- and second-order group delay dispersion associated with the FD-ODL. First, the expressions for $t_{p\_odl}(t)$, $t_{g\_odl}(t)$, $D_{\omega\_odl}(t)$, and $D_{\omega\_odl}^{(1)}(t)$ associated with the FD-ODL, first derived by Zvyagin and D. Sampson $et.\ al.$ [Zvyagin 2003], have been adapted here for a double-pass system. These expressions are derived in the Appendix and given by

$$t_{p\_odl}(t) = \frac{4\Delta z}{c}+\frac{4\Delta\theta(t)x_0}{c}, \qquad (4.25)$$

$$t_{g\_odl}(t) = \frac{4\Delta z}{c}+\frac{4\Delta\theta(t)x_0}{c}+\frac{8\pi\Delta\theta(t)f}{p\omega_0\cos\theta_g}, \qquad (4.26)$$

$$D_{\omega\_odl}(t) = -\frac{16\pi^2 c(\Delta z+f\Delta\theta(t)\tan\theta_g)}{p^2\omega_0^3\cos^2\theta_g}, \qquad (4.27)$$

77

$$D^{(1)}_{\omega\_odl}(t) = \frac{48\pi^2 c(\Delta z + f\Delta\theta(t)\tan\theta_g)}{p^2\omega_0^4 \cos^2\theta_g}(1 + \frac{2\pi c \sin\theta_g}{p\omega_0 \cos^2\theta_g}). \tag{4.28}$$

where p is the grating period, f is the focal length of the lens, Δz is the axial shift of the

grating with respect to the focal plane of the lens, θ_g is the tilt of the grating with respect to the

lens, x_0 is the lateral offset of the pivot point of the scanning mirror with respect to the optical

axis of the lens, $\Delta\theta(t)$ is the scan angle of the mirror, and c is the speed of light.

Provided the set of equations (4.25-4.28), the effect of both the fiber-length mismatch

between two arms and the effect of the specimen are added to the equations of the double-pass

FD-ODL to yield

$$t_p(t) = t_{p\_odl}(t) + t_{p\_fiber}(t) + t_{p\_sample}(t)$$

$$= \frac{4\Delta z}{c} + \frac{4\Delta\theta(t)x_0}{c} + \frac{2\delta}{c} - \frac{2\Delta d_s}{v_{p\_sample}} \tag{4.29}$$

$$t_g(t) = t_{g\_odl}(t) + t_{g\_fiber}(t) + t_{g\_sample}(t)$$

$$= \frac{4\Delta z}{c} + \frac{4\Delta\theta(t)x_0}{c} + \frac{8\pi\theta(t)f}{p\omega_0 \cos\theta_g} + \frac{2\delta}{c} - \frac{2\Delta d_s}{v_{g\_sample}} \quad, \tag{4.30}$$

where δ is the potential optical path length mismatch $l_r - l_s$ between the reference arm and the

specimen arm, l_r is the optical path length in the reference arm, l_s is the optical path length in

the specimen arm up to the specimen surface, and Δd_s is the depth of penetration in the

specimen. The mismatch is caused by the implementation challenge in setting equal fiber length

in both arms of the interferometer. The phase velocity v_{p_sample} is given by c/n_{p_sample}, and the group velocity v_{g_sample} is given by c/n_{g_sample}, where n_{p_sample} is the mean refractive index of the specimen, and the group velocity index n_{g_sample} is given by $n_{p\_sample} - \lambda(dn_{p\_sample}/d\lambda)$. The overall first- and second-order dispersion equations in the interferometer caused by the FD-ODL, the fiber length mismatch, and the specimen are given by

$$D_\omega(t) = D_{\omega\_odl}(t) + D_{\omega\_fiber}(t) + D_{\omega\_sample}(t)$$

(4.31)

$$= -\frac{16\pi^2 c(\Delta z + f\Delta\theta(t)\tan\theta_g)}{p^2\omega_0^3\cos^2\theta_g} + 2\beta_{2\_fiber}\Delta d - 2\beta_{2\_sample}\Delta d_s$$

$$D_\omega^{(1)}(t) = D_{\omega\_odl}^{(1)}(t) + D_{\omega\_fiber}^{(1)}(t) + D_{\omega\_sample}^{(1)}(t)$$

(4.32)

$$= \frac{48\pi^2 c(\Delta z + f\Delta\theta(t)\tan\theta_g)}{p^2\omega_0^4\cos^2\theta_g}(1 + \frac{2\pi c\sin\theta_g}{p\omega_0\cos^2\theta_g}) + 2\beta_{3\_fiber}\Delta d - 2\beta_{3\_sample}\Delta d_s \quad,$$

where Δd is the fiber length mismatch $d_r - d_s$ between the reference arm and the specimen arm, d_r is the fiber length in the reference arm, d_s is the fiber length in the specimen arm, β_{2_fiber} and β_{2_sample} are the first-order dispersion coefficient of the fiber and the specimen, respectively, and similarly β_{3_fiber} and β_{3_sample} are the second-order dispersion coefficient of the fiber and the specimen, respectively. In equations (4.31) and (4.32), we define the dispersion in the reference arm to be positive if the reference arm fiber is longer than the specimen arm fiber (i.e. $\Delta d > 0$). Therefore, the dispersion in the specimen arm, which may be introduced by a specimen, would create an overall negative dispersion mismatch. The FD-ODL is employed to induce

negative or positive dispersion in the reference arm depending on Δd and the dispersion characteristics of the specimen to match the total first- or second-order dispersion in the interferometer arms.

4.1.2 *Relation between the First-Order Dispersion Effects of the FD-ODL and the Optical Fiber*

With a mirror in place of the specimen, the relation between the first-order dispersion owing to a fiber-length mismatch Δd and the first-order dispersion owing to an axial grating shift Δz of the FD-ODL with respect to the focal plane of the lens may be investigated. An axial shift of the tiltable mirror in the FD-ODL with respect to the lens does not affect dispersion because the lens is telecentric in the optical space of the mirror. This axial shift would simply add a constant optical path length to all wavelengths and decrease the coupling efficiency in the interferometer. In order to determine the axial shift of the grating that induces a first-order dispersion equal to the first-order dispersion induced by a given fiber-length mismatch in the interferometer arms, we derive a relation from Eq. (4.31) by

$$D_{\omega}(t) = D_{\omega\_odl}(t) + D_{\omega\_fiber}(t) = -\frac{16\pi^2 c(\Delta z + f\Delta\theta(t)\tan\theta_g)}{p^2\omega_0^3\cos^2\theta_g} + 2\beta_{2\_fiber}\Delta d. \qquad (4.33)$$

The first-order dispersion, $D_{\omega}(t)$, is proportional to Δz as well as the tilt angle of the mirror $\theta(t)$ that may be a sinusoidal or a triangular function of time in the case where θ_g is nonzero. Therefore with θ_g nonzero, the dispersion would be a time-varying function.

Compensation of a time-varying dispersion would need a dynamic grating axial shift synchronized to the tilt angle of the mirror. Hence, we set the tilt of the grating θ_g to zero and the relation between the amount of axial shift Δz of the grating from the focal plane of a lens and a fiber-length mismatch Δd to make the overall first-order dispersion $D_\omega(t)$ zero is given by

$$\frac{\Delta z}{\Delta d} = \frac{\beta_{2\_fiber}\, p^2 \omega_0^3}{8\pi^2 c} \ . \qquad\qquad (4.34)$$

The axial shift Δz required to remove the first-order dispersion caused by the fiber-length mismatch Δd can be set according to the first-order dispersion coefficient of the fiber β_{2_fiber}, the grating period p, and the center frequency of the source ω_0, all known or measurable parameters. The ratio provided by Eq. (4.34) may be computed, and if either one of the two parameters Δz or Δd is known, the other can be determined. In practice, Δz can be theoretically established and Δd can then be computed using Eq. (4.34) as detailed in Section 4.2.1.

4.2 Simulation and Experimental Validation

In a system without dispersion, the power spectral density of the superluminescent diode (SLD) and its autocorrelation function form a Fourier transform pair as given by the Wiener-Khinchin theorem [Goodman 1985]. Fig. 4.1(a) shows the measured power spectral density of a SLD and Fig. 4.1(b) presents the corresponding photocurrent signal simulated by taking the

inverse Fourier transform of the measured power spectral density of the SLD. Given the power

spectral density of the SLD shown in Fig. 4.1(a), Fig 4.1(b) presents the ideal photocurrent signal.
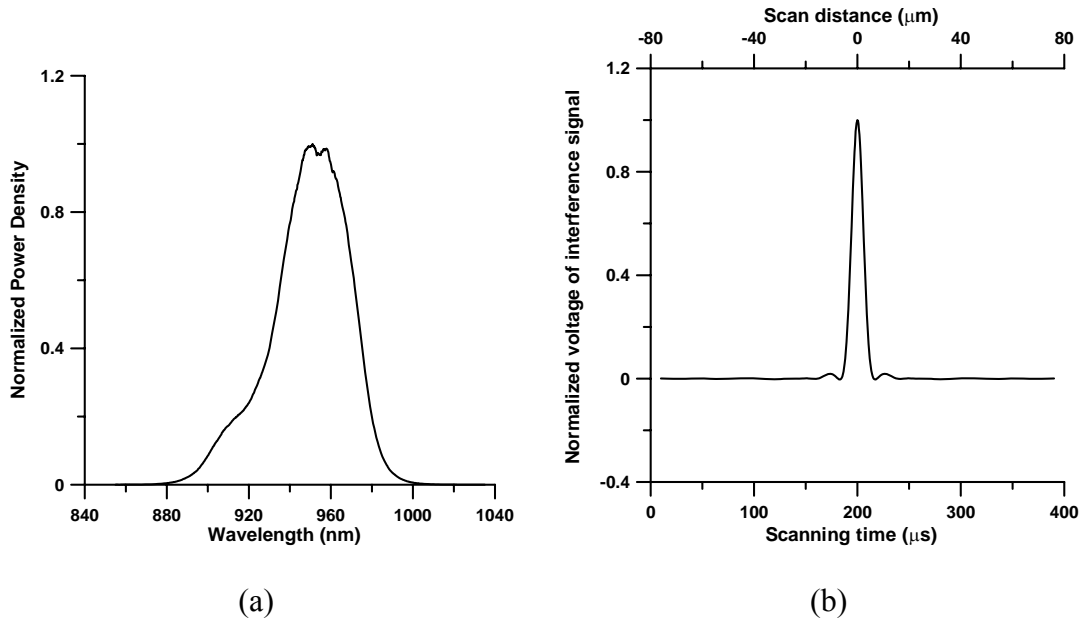
Figure 4.1 :(a) Measured power spectral density of the SLD; (b) Corresponding ideal photocurrent signal.

We implemented the fiber optic interferometer shown in Fig. 4.2. The source is a

superluminescent diode (SLD-47HP Superlum Diodes) centered at 950 nm with a spectral

bandwidth of approximately 70 nm and a power of 7 mW. An attenuator is employed to prevent

optical feedback into the SLD, which would cause permanent damage to the source. A large

bandwidth circulator or isolator centered at 950 nm would have been preferred, but such

components were not yet commercially available. The light emitted by the SLD passes through

two fused fiber couplers. A splitting ratio of 80/20 enabled maximum power into the specimen

reducing excess noise arising from the reference arm. Fig. 4.2 also shows the FD-ODL that was

used for depth scanning and dispersion compensation. We used a balanced detector (Nirvana 2017) connected to a real-time oscilloscope (Tektronix TDS210) in order to observe the photocurrent signal. The oscilloscope was connected to a computer that recorded the signal.
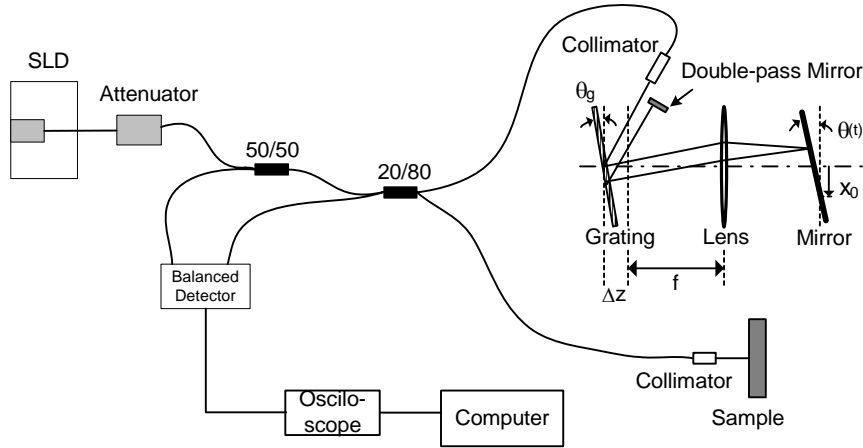
Figure 4.2 : Schematic diagram of a fiber-optic imaging interferometer with a frequency-domain optical delay line (FD ODL) in the reference arm.

In section 4.2.1 we combine experimental work with the theoretical analysis of dispersion in the interferometer up to second-order given in section 4.1. We use a mirror as the specimen first and then analyze the effect of first- and second-order dispersion on the photocurrent signal. We then perform first-order dispersion compensation by adjusting Δz in the FD-ODL to improve the degraded photocurrent signal. In section 4.2.2, we simulate and demonstrate experimentally the effect of dispersion with a LiTaO3 specimen that was chosen given its suitable dispersion characteristics to model a skin specimen in order to validate the process with ground truth dispersion values relevant to tissue imaging.

4.2.1 First-Order Dispersion Compensation and Effect of Second-Order Dispersion on the Photocurrent Signal when the Specimen is a Mirror

The parameters related to the single-mode optical fiber and the FD-ODL are given in Table 4.1. Inserting these parameters into Eq. (4.34), we find the ratio $\Delta z / \Delta d$ equals 0.0168.

Table 4.1 : Parameters of the single-mode optical fiber and the FD ODL

λ_0	β_{2_fiber} at λ_0	β_{3_fiber} at λ_0	p	f	$\Delta\theta_{max}(t)$
950nm	$34.95\text{fs}^2/\text{mm}$	$420\text{fs}^3/\text{mm}$	$1.204\mu\text{m}$	25mm	$2°$

The grating was set to be parallel to the lens (i.e. zero tilt angle). To obtain the narrowest photocurrent signal we shifted the grating axially in order to match the first-order dispersion in the arms of the fiber optic interferometer. We then simulated the photocurrent signal of the system by theoretically varying Δz and x_0. The value of x_0, predicted by this process, was set experimentally at 0.4 mm. This value results in a low modulation frequency for the photocurrent signal, which is directly proportional to x_0 as shown in Eqs. (4.24) and (4.25). Δz was set at 0.06 mm and validated theoretically as well. The fiber-length mismatch Δd was then computed to be 3.6 mm using Eq. (4.34).

Fig. 4.3(a) shows the narrowest photocurrent signal obtained experimentally by adjusting the grating axial shift Δz to compensate the first-order dispersion induced by the fiber-length mismatch. Fig. 4.3(b) represents the corresponding photocurrent signal simulated using Δz, Δd, and x_0 equal 0.06 mm, 3.6 mm, and 0.4 mm, respectively. These figures illustrate that the first-order dispersion induced by Δz equal 0.06 mm compensates the first-order dispersion induced by

the 3.6 mm of fiber-length mismatch between the two arms. With this setting, no overall first-order dispersion remains. However, the second-order dispersion, corresponding to Δz equal 0.06 mm and Δd equal 3.6 mm, is non-zero and is best shown by the small asymmetric oscillations in Figs. 4.3(a-b).

(a)   (b)
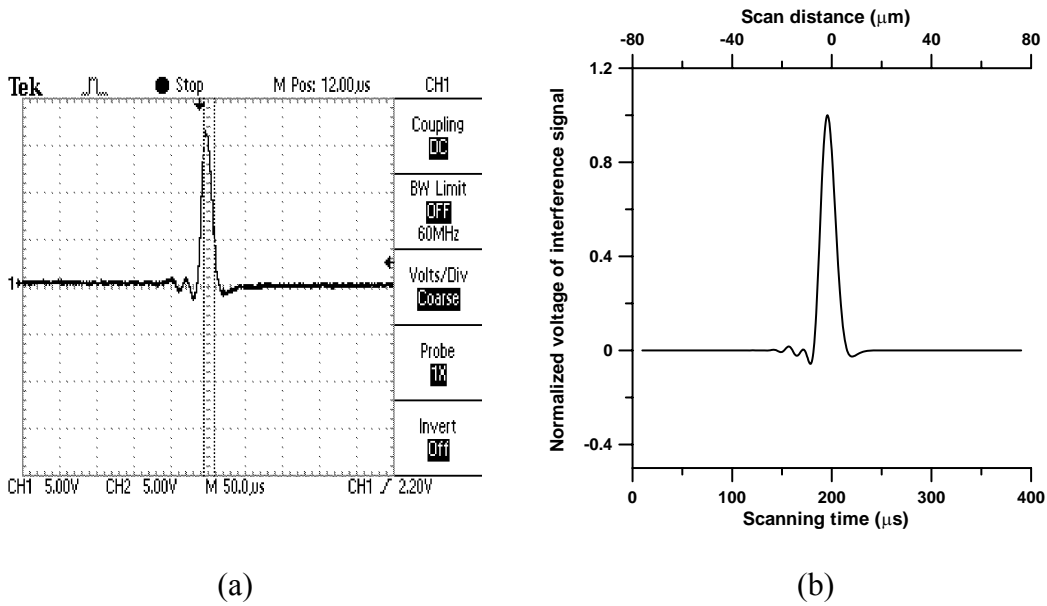
Figure 4.3 : (a) Experimental result corresponding to the parameters listed in (b); (b) Simulation result for $\Delta z = 0.06$ mm, $\Delta d = 3.6$ mm, and x0 = 0.4 mm.

To further validate the set value of x_0, we increased Δz from 0.06 mm to 0.13 mm. The first-order dispersion caused by Δz equal 0.06 mm out of the total grating axial shift Δz equal 0.13 mm compensates the 3.6 mm of the fiber-length mismatch between the two arms because the first order dispersion owing to the FD-ODL is linear with the grating axial shift Δz as given by Eq. (4.27). Thus, there remains first-order dispersion due to the additional axial shift of the gratings of 0.07 mm, second-order dispersion due to the overall grating axial shift Δz equal 0.13

mm, and second-order dispersion due to the fiber-length mismatch Δd equal 3.6 mm. The corresponding photocurrent signal is shown in Fig. 4.4(a) & (b).

To isolate the contribution of the first-order dispersion, we also simulated the photocurrent signal shown in Fig. 4.4(c), where the total second-order dispersion was simply set to zero in the simulation. We then simulated the photocurrent signal shown in Fig. 4.4(d) by setting the total first-order dispersion in the simulation to zero, so that the contribution of the second-order dispersion could be isolated and visualized. Results of these simulations show that the asymmetric shape and sidelobes in the photocurrent signal are caused by the second-order dispersion of the interferometer.
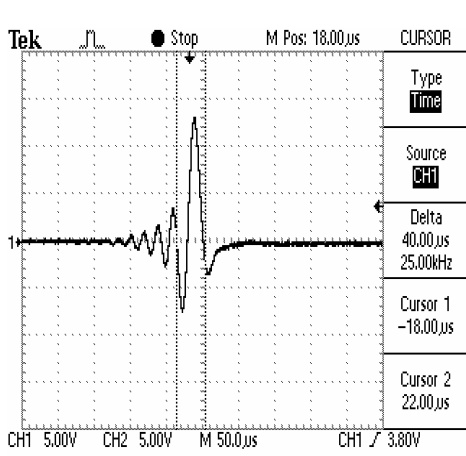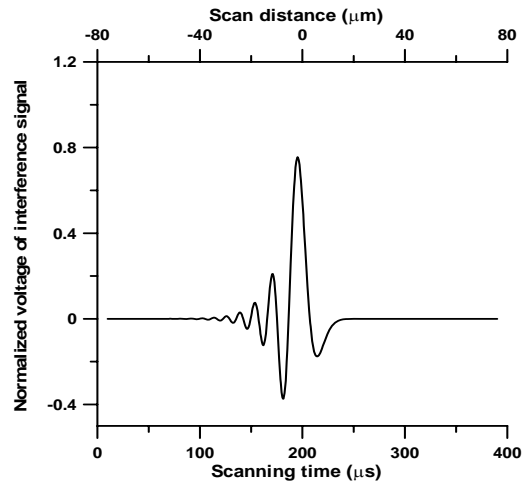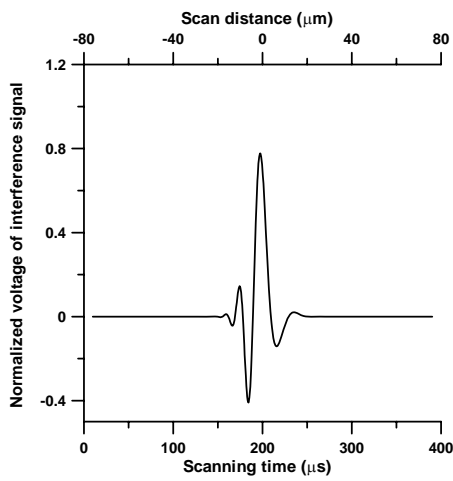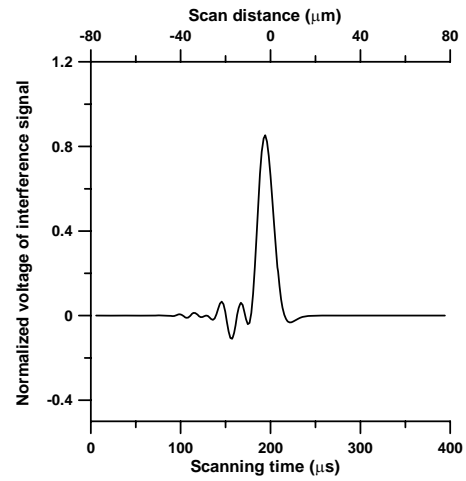
Figure 4.4 : (a) Experimental result with an additional 0.07 mm axial grating-shift from the initial 0.06 mm; (b) Simulation result for $\Delta z = 0.13$ mm, $\Delta d = 3.6$ mm, and x0 = 0.4 mm; (c) Isolated impact of first-order dispersion; (d) Isolated impact of second-order dispersion.

4.2.2 *Impact of Dispersion due to a Dispersive Specimen on the Photocurrent Signal*

In section 4.2.1, we investigated the impact on the signal photocurrent of the first- and

second-order dispersion induced by the fiber-length mismatch between the interferometer arms

87

and the FD-ODL. We quantified the compensation of the first-order dispersion induced by the fiber-length mismatch using the FD-ODL. The specimen employed was a mirror and thus was non-dispersive. In this section, we add the impact of dispersion due to a dispersive specimen on the photocurrent signal. A layered $LiTaO_3$ specimen was selected due to its similar dispersion characteristics to that of a skin specimen. Given that the first-order dispersion coefficient of $LiTaO_3$ is about twice as large as that of skin at 950 nm as shown in Table 4.2, light centered at 950 nm takes on the same first-order dispersion after going through 0.5 mm of $LiTaO_3$ as 1.085 mm of skin specimen. The slight mismatch in second-order dispersion between the skin and the $LiTaO_3$ specimens is found to be negligible. The dispersion coefficients provided in Table 4.2 were derived from the formula for the refractive indices of skin and $LiTaO_3$ given as a function of wavelength in [Troy 2001] and [Abedin 1996]. Using this formula and definitions given in [Lakoba 1999] and [Agrawal 1995], we computed the first- and second-order dispersion coefficients, β2 and β3, of skin and $LiTaO_3$. These coefficients indicate that the first-order dispersion in a skin specimen is large compared to that in the optical fiber, and thus the specimen must be accounted for in any compensation scheme. Since we are focusing in this chapter essentially on dispersion and its impact on resolution, we do not model the power loss due to reflections, scattering, and absorption within $LiTaO_3$.

Table 4.2 : Dispersion Coefficients of Skin and $LiTaO_3$

Specimen	β_2 at 950nm	β_3 at 950nm
Skin	109 fs^2/mm	159 fs^3/mm
$LiTaO_3$	236.8 fs^2/mm	188 fs^3/mm

The simulations and experiments of the photocurrent signal were based on the experimental setup described in section 4.2.1, with the exception that x_0 was increased to 3 mm to modulate the photocurrent signal at a higher frequency where the noise level drops and the signal-to-noise ratio increases. The grating axial-shift Δz was set to 0.06 mm, where the first-order dispersion induced by the fiber-length mismatch of 3.6 mm between the interferometer arms was compensated. The first scenario presented in Fig. 4.5 shows the photocurrent signals when the first-order dispersion was compensated for the light reflected from layer A, indicated with a bold line in Fig. 4.5(a). The 2-D image of the specimen is shown in Fig. 4.5(b). The photocurrent signals are shown in Fig. 4.5(c) when two layers of $LiTaO_3$ separated by an air gap of 80 μm were scanned through the single line S labeled in Fig. 4.5(b). Figs. 4.5(d), 4.5(e), and 4.5(f) present the measured photocurrent signal induced by the reflections off the layers A, B, and C respectively. Also shown in Figs. 4.5(d), 4.5(e), and 4.5(f) are the envelopes of the measured photocurrent signal and the envelopes of the simulated photocurrent signal. The broadening and asymmetry of the envelopes of the photocurrent signal caused by uncompensated first- and second-order dispersion induced by $LiTaO_3$ and the FD-ODL are observed in Fig. 4.5(e) and 4.5(f), while the photocurrent shown in Fig. 4.5(d) only suffers from second-order dispersion. For the light reflected from the back-end of $LiTaO_3$ which is layer C, the impact of dispersion is so severe that the corresponding photocurrent signal is broadened maximally.
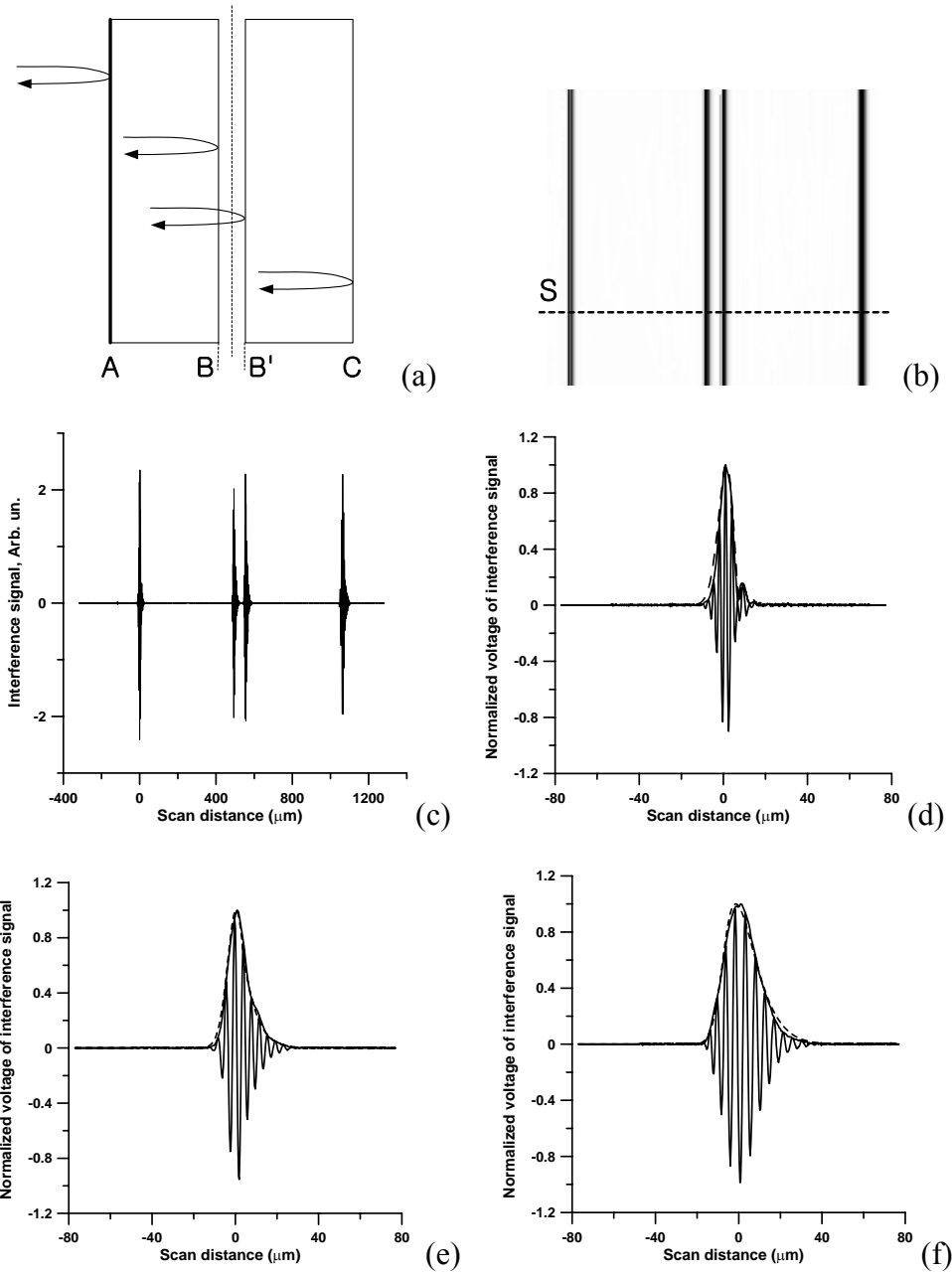
Figure 4.5 : (a) Schematic of two layers of 0.5mm LiTaO$_3$ separated by an air gap; (b) 2-D image of the specimen when the first-order dispersion compensation is set for the signal reflected off the front surface A of the specimen; (c) Single depth scan through the line *S* shown in (b) of the specimen image; (d-f) Solid lines are zoomed photocurrent signal envelopes while dashed-lines are simulated photocurrent signal envelopes for light reflected off; (d) the front surface *A*, (e) the second surface, i.e. from the layer *B*, and (f) the back surface *C* of the specimen, for $\Delta z =$ 0.06 mm, $\Delta d = 3.6$ mm, and $x_0 = 3$ mm.

Observing the severe degradation in the photocurrent signal due to the reflection from the back layer of $LiTaO_3$, i.e. from the layer C, we investigated a scenario where the grating of the FD-ODL was moved closer to the lens of the FD-ODL, i.e. Δz was decreased, so that the total first-order dispersion in the system was zero for the light reflected in the mid-plane of $LiTaO_3$, i.e. from the layer B, as shown in Fig. 4.6(a). We computed the corresponding grating axial shift to be 0.005 mm. Fig. 4.6(c) presents the measured photocurrent signals resulting from reflections off layers A, B, and C respectively through the single line S shown in Fig. 4.6(b). The photocurrent signals and their envelopes are shown in Fig. 4.6(d)-4.6(f). In this case, results show a smaller overall broadening of the photocurrent signal envelopes across the depth of the specimen and a weaker effect of first-order dispersion in the photocurrents. The photocurrent signal that is less affected by the first order dispersion is, as expected, the one detected from layer B as shown in Fig. 4.6(e).

To be comprehensive, we investigated a final scenarios, where we further decreased the grating axial shift Δz down to -0.055 mm so that the total first-order dispersion was set to zero for the light reflected at the back-end of the $LiTaO_3$ shown with a bold line in Fig. 4.7(a). The severe impact of the first-and second-order dispersion is demonstrated in Fig. 4.7(d) for the photocurrent signal resulting from the reflection off layer A of the specimen. The photocurrent signal shown in Fig. 4.7(f) presents the slight effect of second-order dispersion. Figure. 4.7(e) shows the photocurrent signal measured from the reflection off layer B of $LiTaO_3$.

91
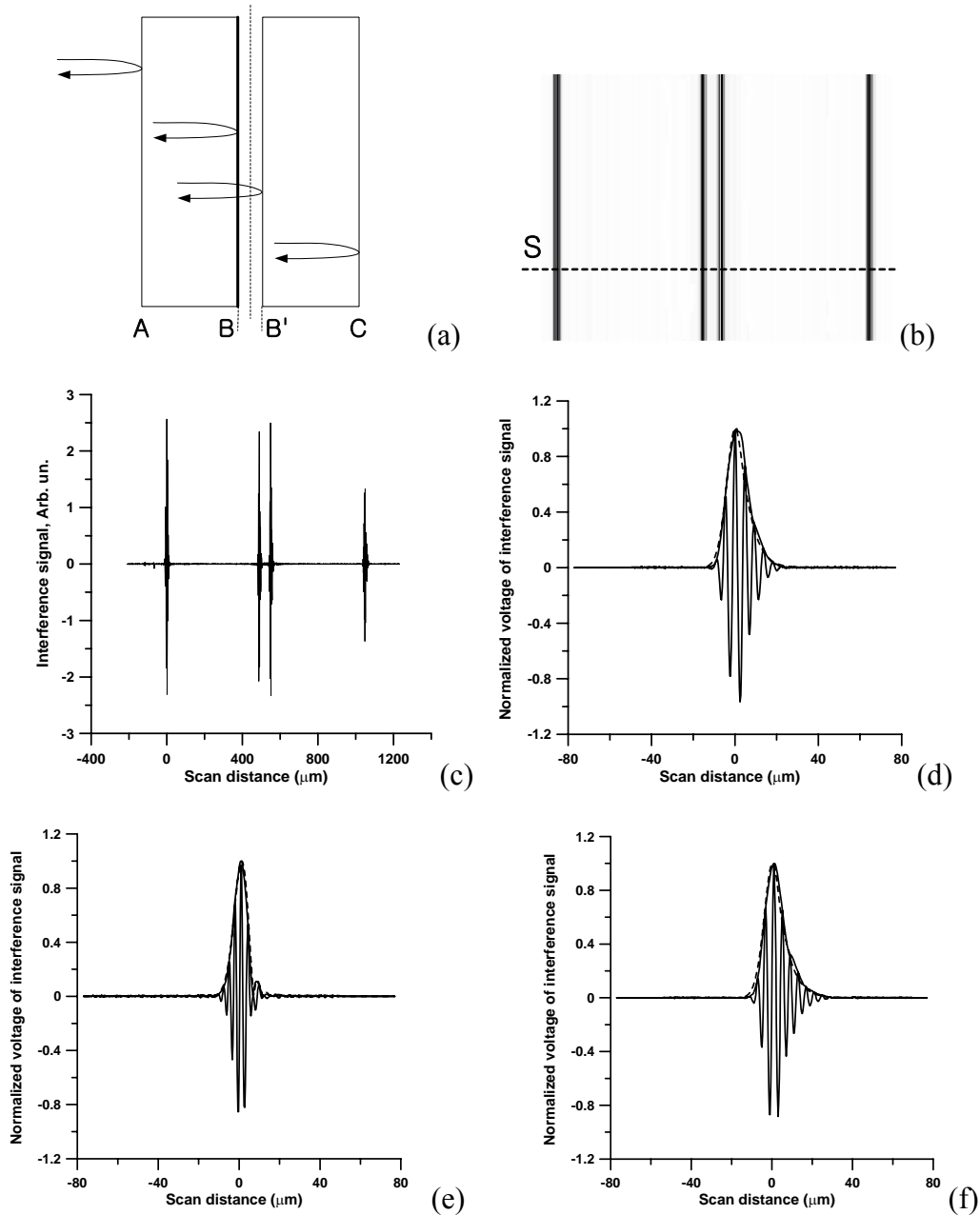
Figure 4.6 : Schematic of two layers of 0.5 mm LiTaO₃ separated by an air gap; (b) 2-D image of the specimen when the first-order dispersion compensation is set for the signal reflected off the middle surface B of the specimen; (c) Single depth scan through the line S shown in (b) of the specimen image; (d-f) Solid lines are zoomed photocurrent signal envelopes, while dashed-lines are simulated photocurrent signal envelopes for light reflected off (d) the front surface *A*, (e) the second surface, i.e. from the layer *B*, and (f) the back surface *C* of the specimen, for $\Delta z = 0.06$ mm, $\Delta d = 3.6$ mm, and $x_0 = 3$ mm.
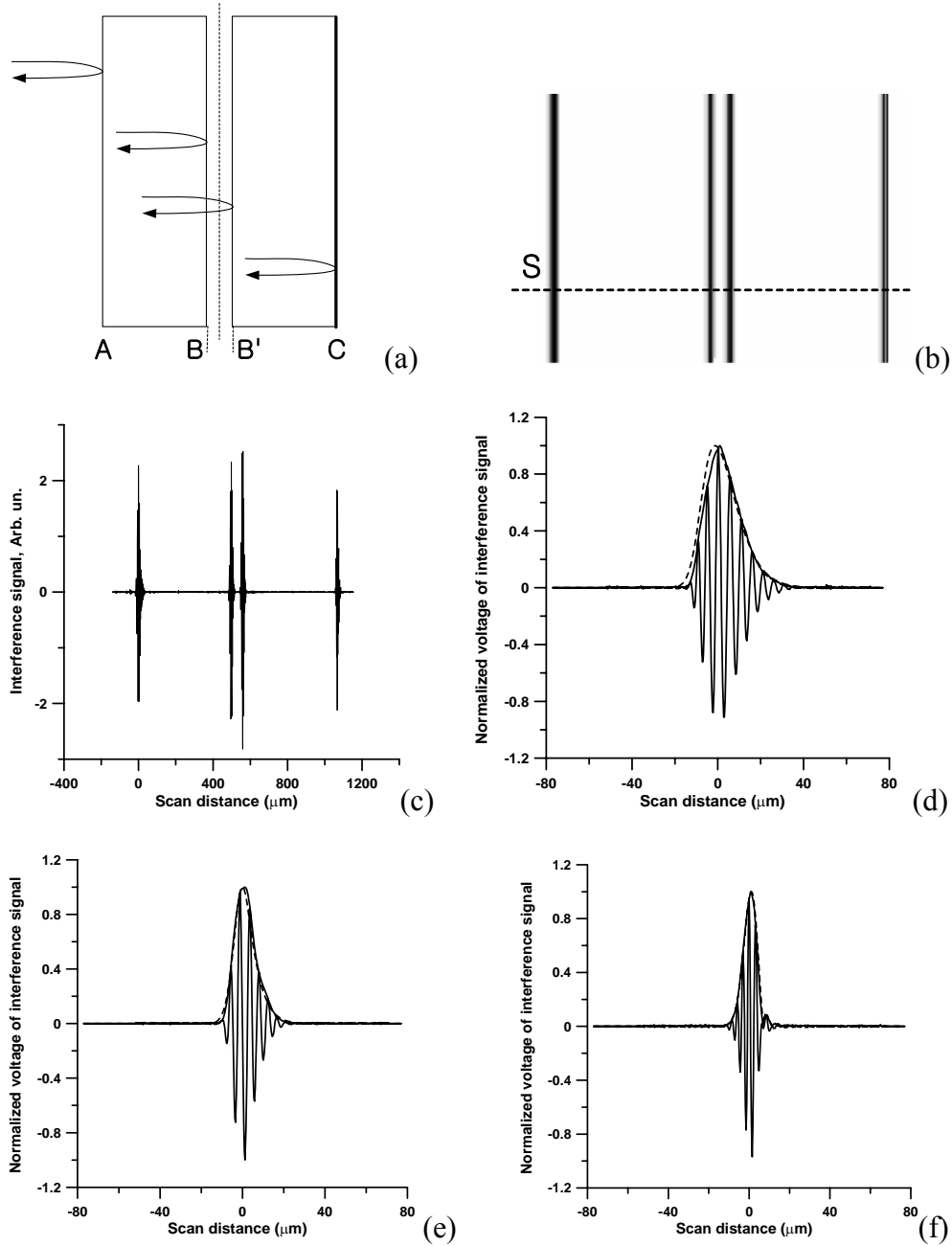
Figure 4.7 : Schematic of two layers of 0.5 mm LiTaO$_3$ separated by an air gap; (b) 2-D image of the specimen when the first-order dispersion compensation is set for the signal reflected off the back surface C of the specimen; (c) Single depth scan through the line S shown in (b) of the specimen image; (d-f) Solid lines are zoomed photocurrent signal envelopes while dashed-lines are simulated photocurrent signal envelopes for light reflected off (d) the front surface A, (e) the second surface, i.e. from the layer B, and (f) the back surface C of the specimen, for $\Delta z = 0.06$ mm, $\Delta d = 3.6$ mm, and $x_0 = 3$ mm.

Photocurrent signals presented in Figures 4.5(d), 4.6(e), and 4.7(f) with overall first-order dispersion equal to zero are not the same because the second-order dispersion for each case is different. For example, the photocurrent signal in Fig 4.5(d) presents significant sidelobes while the one shown in Fig 4.7(f) does not possess any significant sidelobes. Therefore, we do not necessarily expect the axial resolution for each case to be the same because of the impact of second-order dispersion. Table 4.3 presents the computed axial resolutions based on the photocurrent signals shown in Fig.4.5, Fig 4.6, and Fig 4.7(i.e. l_A, l_B, l_B', l_C). The ASI is the absolute square integral of the envelopes of the photocurrent signals and is a metric used to quantify the axial resolution in OCT, while RMSW (i.e. σ_{rms}) is the root-mean-square of the envelopes of the photocurrent signals [Sorokin 2000, Akcay 2002].

Table 4.3 : Computed Axial Resolutions in LiTaO$_3$

Case	Metric	l_A (µm)	l_B (µm)	l_B' (µm)	l_C (µm)
Front surface	ASI	6.35	8.04	8.04	14.23
dispersion compensation	RMS-width	8.87	12.94	12.94	18.71
Middle surface	ASI	8.05	6.18	6.18	8.16
dispersion compensation	RMS-width	12.67	8.05	8.05	12.14
Back surface	ASI	14.45	8.25	8.25	6.00
dispersion compensation	RMS-width	18.34	11.96	11.96	7.33

With the results that quantify resolution presented in Table 4.3, we have shown that the axial resolution in the OCT system is not fixed over a scanned specimen because of dispersion. When the total first-order dispersion is set to zero for the middle plane of the specimen by shifting the

grating of the FD-ODL axially, the impact of the first-order dispersion on the photocurrent signal is minimized over the entire depth of the scanned specimen. In the case of this optimal setting, the small broadening and asymmetry of the photocurrent signal are a combination of first-order residual dispersion away from the plane of compensation and the associated second-order dispersion, respectively.

CHAPTER FIVE: BESSEL BEAM BASED ON FREQUENCY DOMAIN OCT

In this Chapter we study a Bessel beam based confocal scanning optical microscope (BCSOM) and apply it to FD OCT to achieve high resolution over an extended depth of focus. The BCSOM, which uses a single mode fiber to implement a confocal imaging system instead of a pinhole, is described and a mathematical model is derived. Simulations of illumination and detection of Bessel beams based on the model are presented. The model includes the influence of the axicon tip on imaging as well as of the single mode fiber on imaging. We demonstrate that the side lobes of the lateral PSF, which is the Bessel function generated by an axicon, are suppressed when traveling twice through the axicon in the confocal imaging system. The BCSOM is applied to the FD-OCT system to demonstrate its benefit of high lateral resolution over extended depth of focus without refocusing. We then report on the measured resolution and sensitivity achieved with a custom-made microoptic axicon lens. Double-pass Bessel-beam FD OCT with an axicon microoptics is demonstrated in a biological sample showing invariant resolution and SNR across a 4 mm measured DOF and this result is compared to Gaussian beam imaging.

5.1 Bessel Beam Confocal Optical Imaging using an Axicon Lens

5.1.1 Mathematical Model

The fundamental fiber mode for a single mode fiber is often approximated by a Gaussian distribution. With this approximation, the electric field at the output face of the single mode fiber is described by [Marcuse 1982].

$$E_f(x, y) = \exp\left[-\frac{(x^2 + y^2)}{w^2}\right], \tag{5.1}$$

where the width parameter w can be determined by the fiber parameter V defined by $V = \frac{2\pi a}{\lambda}\left(n_1^{\,2} - n_2^{\,2}\right)^{1/2}$, where n_1 and n_2 are the core and cladding index of refraction, and a is the core radius of the fiber.

By placing the output face of the fiber at the front focal point of the lens, the lens creates a collimated Gaussian beam that then forms the waist at the focal point image F' of the lens shown in Fig. 5.1, which is where the axicon is placed. The incident electric field $E_i(x, y)$ at the axicon is derived from the electric field $E_f(x, y)$ at the fiber output face using a Fourier transform relation of a 2f system given by [Goodman 1996]

$$E_i(x, y) = i\lambda f \cdot \tilde{E}_f(\xi, \eta)\Big|_{\xi = \lambda fx, \eta = \lambda fy}, \tag{5.2}$$

where $\widetilde{E}_f(\xi,\eta)$ is the Fourier transform of $E_f(x,y)$. The Gaussian beam can be itself approximated by a plane wave as it propagates through the axicon, because the thickness of the axicon is negligible compared to the Rayleigh distance of the collimated Gaussian beam. Assuming no energy loss from the axicon, the electrical field $E_i(x,y)$ of the Gaussian beam may be rewritten as $E_i(r)$. The electrical field immediately after the axicon, defined as z=0 plane, as shown in the Fig 5.1 is described by

$$E(r, z = 0) = E_i(r) \cdot \exp(ik_r r) \quad , \tag{5.3}$$

where r is the radial distance, the phase term $k_r r$ is the accumulated phase in the direction of r contributed by the axicon, and $k_r = -k \sin \beta$, where k is the wave propagation constant. Here, β is the beam deviation angle with respect to the optical axis that is computed using Snell's law,

$$\beta = \sin^{-1}\left(\frac{n_a}{n_s}\sin \alpha\right) - \alpha \quad , \tag{5.4}$$

where n_a is the refractive index of the axicon and n_s is the refractive index of the surrounding medium (n_s=1 in free space), and α is the edge axicon angle. The Fourier decomposition of the complex electrical field amplitude distribution in the z=0 plane is done to make use of the propagation method applied in the spatial frequency domain. The two dimensional Fourier transform of the rotational symmetric field may be written as a Fourier-Bessel transform (i.e. zero-order Hankel transform). Each component of the angular spectrum of Eq. (5.3) are derived by the Fourier-Bessel transform and it is given by [Gaskill 1978]

$$\tilde{E}(\rho, z = 0) = \int_0^\infty E_i(r) \exp(-irk\sin\beta) J_0(2\pi\rho r) r \, dr \,, \tag{5.5}$$

where the ρ is the spatial frequency in the r coordinate. As the field propagates beyond the axicon in the z direction, each component of the angular spectrum accumulates its own phase $k_z z$ along the z direction

$$\tilde{E}(\rho, z) = \tilde{E}(\rho, z = 0) \exp(ik_z z) = \tilde{E}(\rho, z = 0) \exp\left(iz\sqrt{k^2 - (2\pi\rho)^2}\right) . \tag{5.6}$$

After Eq. (5.5) is inserted into Eq. (5.6), the field $\tilde{E}(\rho, z)$ is given by [Cizm´ar 2006]

$$\tilde{E}(\rho, z) = \exp\left(iz\sqrt{k^2 - (2\pi\rho)^2}\right) \int_0^\infty E_i(r) \exp(-irk\sin\beta) J_0(2\pi\rho r) r \, dr \tag{5.7}$$

Then, $E(r, z)$ in the spatial domain is calculated from $\tilde{E}(\rho, z)$ using the inverse Fourier-Bessel transform.
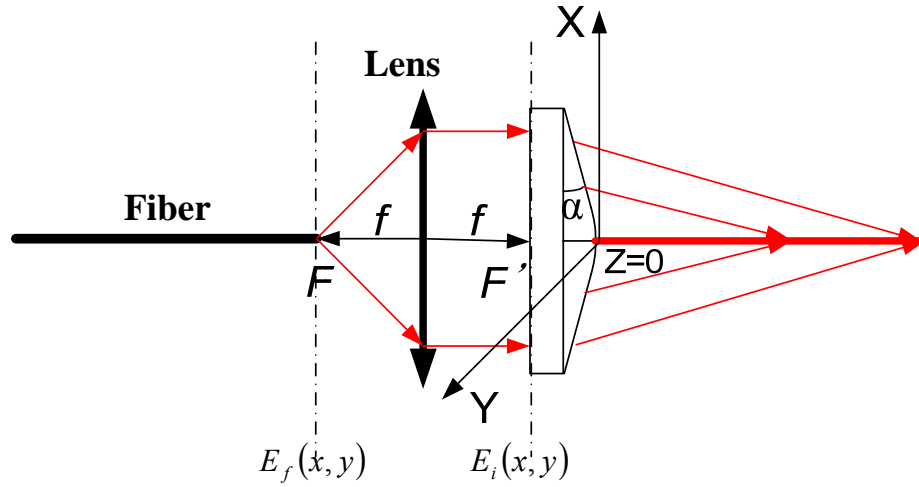
Figure 5.1 : The propagation of a Gaussian beam from a single mode fiber incident on the axicon located at the waist of the Gaussian beam

In practice, it is common to model the profile of an axicon as a hyperbolic curve. In this case, the deviation angle β becomes a function of the radius r as shown in Fig. 5.2. The surface of a hyperboloid of interest (for $z < 0$) is described as

$$\frac{z^2}{a^2} - \frac{r^2}{b^2} = 1 \quad , \tag{5.8}$$

where a and b are defined as the horizontal and vertical semi-axes as shown in Fig. 5.3. The tangent line at a point $P(z_0, r_0)$ of the hyperbola (red line in Fig. 5.3) is given by

$$\frac{z_0 z}{a^2} - \frac{r_0 r}{b^2} = 1 \quad . \tag{5.9}$$

The absolute value of the slope at a point P is given by

100

$$\left|\frac{dz}{dr}\right|_{z=z_0,r=r_0} = \left|\frac{a^2}{b^2}\cdot\frac{r_0}{z_0}\right| \quad . \tag{5.10}$$

So, the edge angle of the axicon at the point P is given by

$$\alpha(z_0,r_0) = \tan^{-1}\left(\left|\frac{a^2}{b^2}\cdot\frac{r_0}{z_0}\right|\right) \quad . \tag{5.11}$$

Putting r_0 in place of z_0 using Eq. (5.8) allows expressing Eq. (5.11) of a function of r,

$$\alpha(r) = \tan^{-1}\left(\left|\frac{a}{b}\cdot\frac{r}{\sqrt{b^2+r^2}}\right|\right) \quad . \tag{5.12}$$

Using eq. (5.4) the deviation angle $\beta(r)$ is

$$\beta(r) = \sin^{-1}\left(\frac{n_a}{n_s}\sin\left(\tan^{-1}\left(\left|\frac{a}{b}\cdot\frac{r}{\sqrt{b^2+r^2}}\right|\right)\right)\right) - \tan^{-1}\left(\left|\frac{a}{b}\cdot\frac{r}{\sqrt{b^2+r^2}}\right|\right) \quad . \tag{5.12}$$

The field $\tilde{E}(\rho,z)$, including the effect of the axicon tip, can be solved by replacing the β in Eq. (5.7) with $\beta(r)$, which yields

$$\tilde{E}(\rho,z) = \exp\left(iz\sqrt{k^2-(2\pi\rho)^2}\right)\int_0^\infty E_i\exp(-irk\sin\beta(r))J_0(2\pi\rho r)rdr \quad . \tag{5.13}$$

101
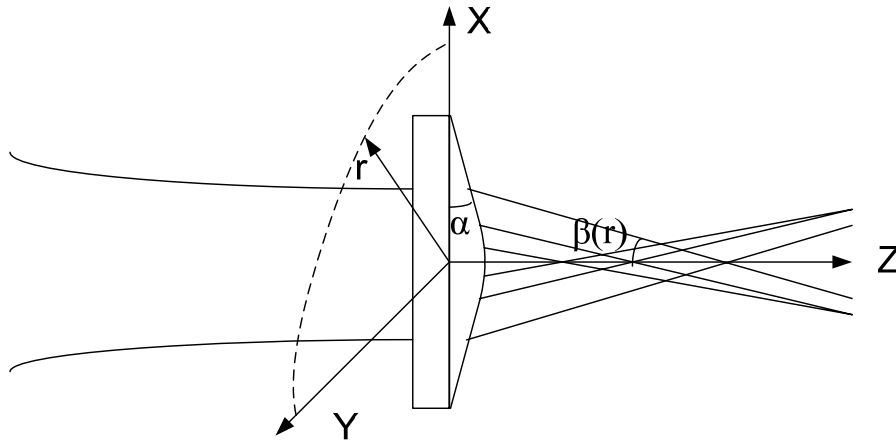
Figure 5.2 : The propagation of a Gaussian beam incident on an axicon (modeled as a hyperbola) located at the waist of the Gaussian beam
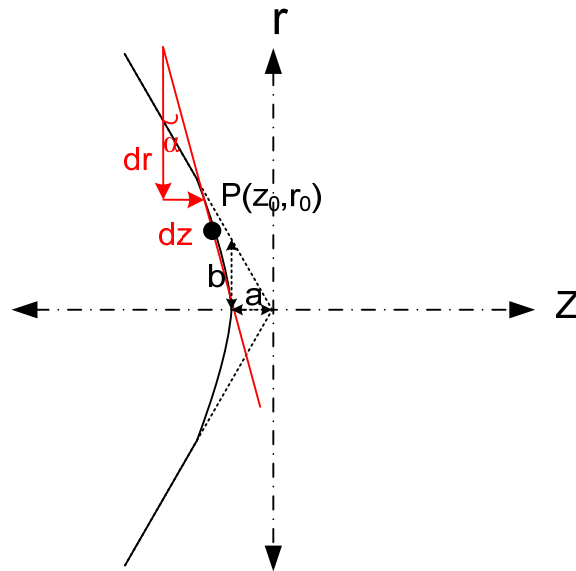
Figure 5.3 : An hyperbola curve describing the shape of an axicon surface in the (r,z) coordinate system; the red line represents the tangent to the surface at a point P.

The electric field beyond the axicon (for $z>0$) in the spatial domain was simulated using the inverse Fourier transform of Eq. (5.13) with the simulation parameters provided in Table 5.1.

Table 5.1 : Simulation parameters

Axicon edge angle (degrees)	Axicon thickness (mm)	Material of axicon	Vertex radius of the axicon (mm)	Wavelength of source (nm)	Incident beam size (Full width at $1/e^2$) (µm)
5	2	Fused silica (Refractive index at 800nm :1.45332)	0.65	800	600

For the simulation, we assume a 600 μm (Full width at $1/e^2$) Gaussian beam generated from the fundamental mode (TEM$_{00}$) of the single mode fiber is incident on the axicon lens in the *2f* system shown in Fig. 5.1. The normalized incident intensity $|E_i(r)|^2$ is shown in Fig 5.4.
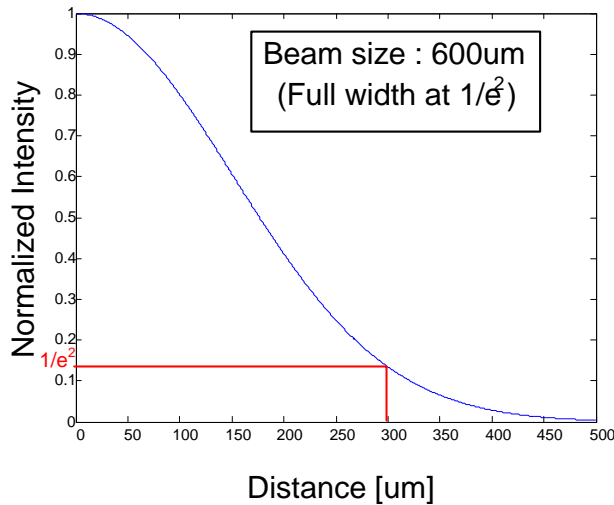
Figure 5.4 : Incident beam intensity profile

The simulated peak optical intensity on-axis are shown in Fig. 5.5. At the location of the axicon lens, an annular ring of incident light with radius *r* close to zero focuses close to the

axicon and illuminates with almost no focused power. As r increases the focused power is increasing. However the intensity drops at some radius value because the power of the annular ring is decreasing following the decrease of the Gaussian distribution of the incident beam away from the optical axis. The periodic modulation of the intensity comes from the interference between the spherical beam refracted from the axicon tip with the wave propagation k and the annular beam with the wave propagation k_z. The modulation depth is decreased given the decreased power along the axial distance z. The corresponding lateral optical intensity profiles to the points z=1 mm, 2 mm, 4 mm, and 6 mm in Fig. 5.5 are shown in Fig. 5.6 for the case of no tip and Fig. 5.7 for the case of a tip. The first zero radius of the Bessel beam is almost invariant over 4 mm. The light propagating from the axicon tip affects the broadening of the radius of the point spread function as shown in Fig. 5.7(a).
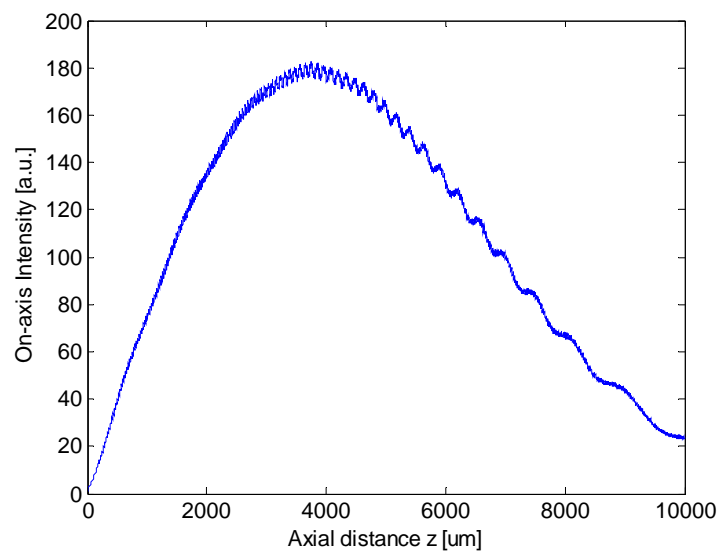
(a)
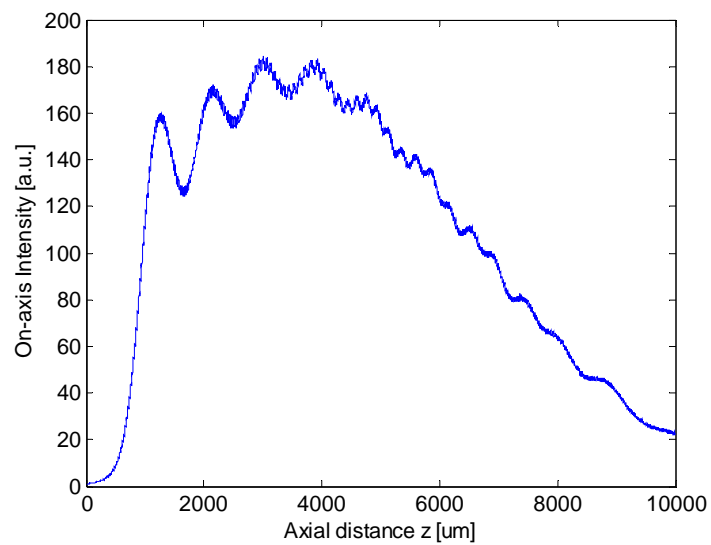
(b)

Figure 5.5 : Simulated axial peak optical intensity beyond the axicon (a) with no tip using Eq. (5.7) (b) with a hyperbolic tip using Eq. (5.13).
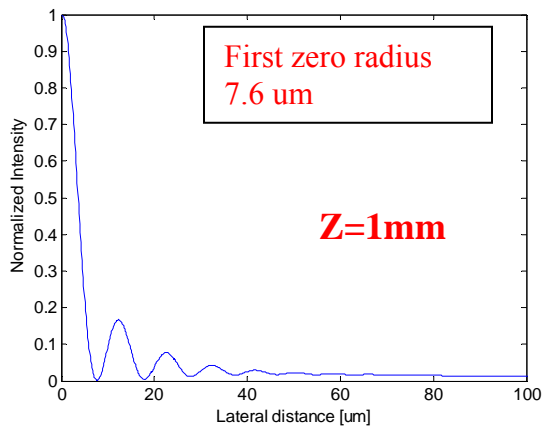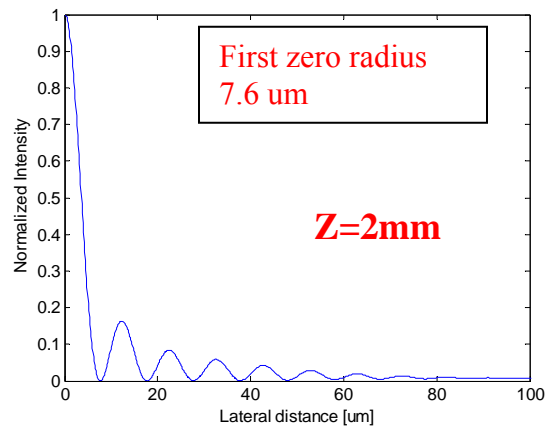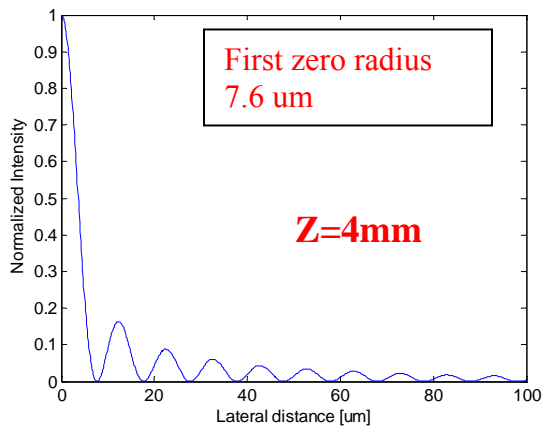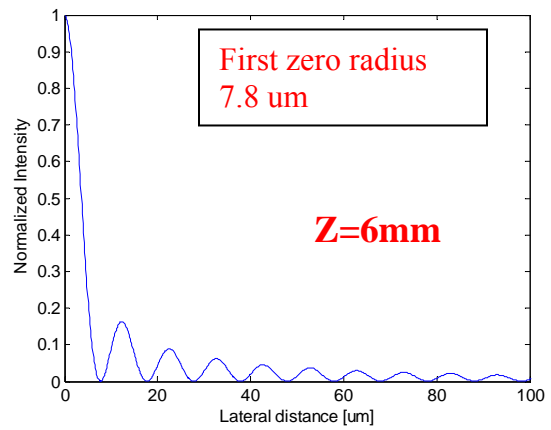
Figure 5.6 : Normalized lateral profiles over the depth of focus with no tip
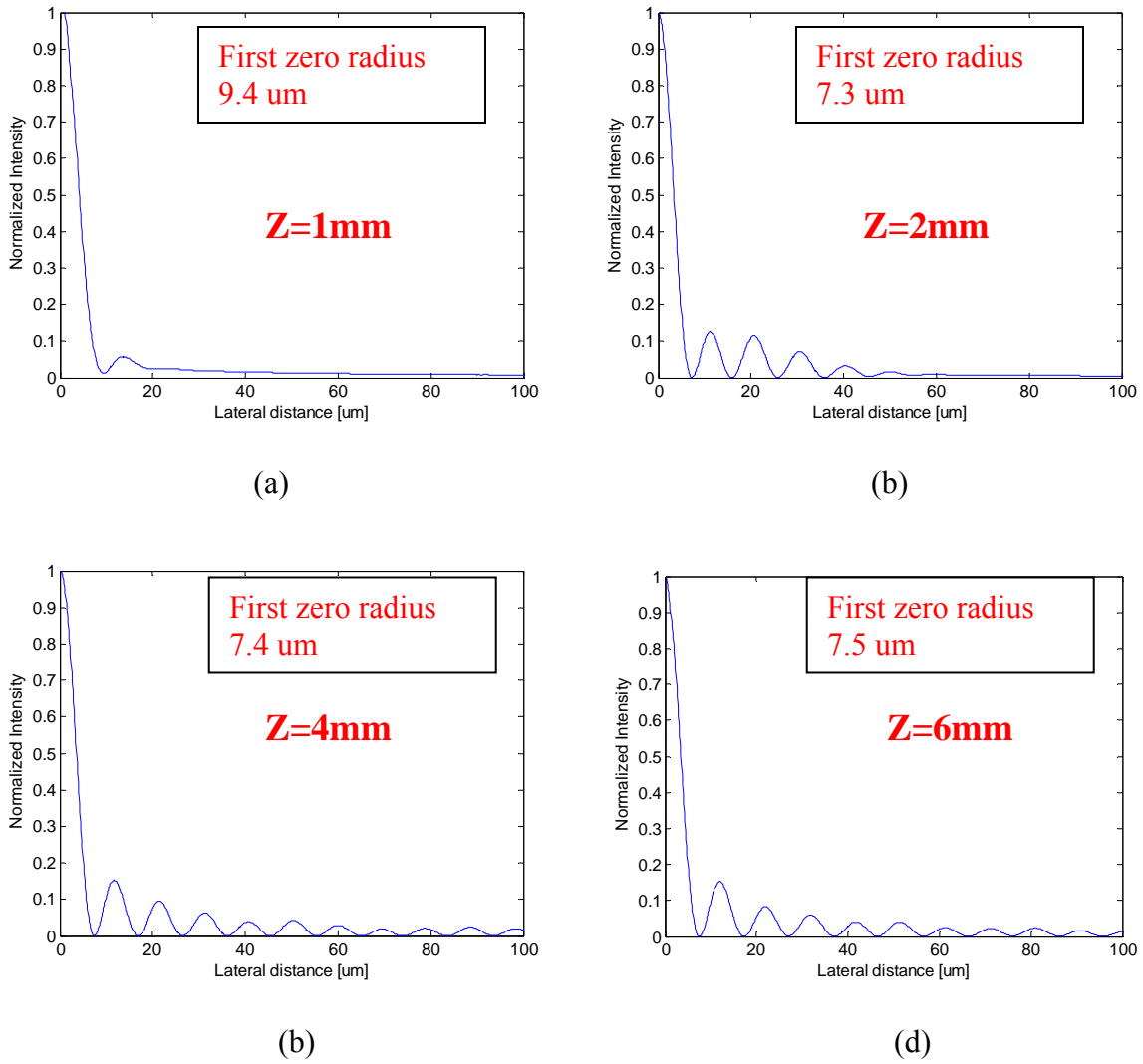
Figure 5.7 : Normalized lateral profiles over the depth of focus with a hyperbolic tip

To investigate the influence of the confocal detection imposed by the single mode fiber on imaging, the reflectance of the object is introduced as $R(x, y, z)$ and the object is scanned in x and y in 2 dimensions, which can be described by $R(x - x_s, y - y_s, z)$ where Xs and Ys are the scanned distances in the 2 dimensions. The inverse Fourier-Bessel transform of $\widetilde{E}(\rho, z)$ in Eq.

(5.13) is used for the illuminating electric field $E_{il}(x, y, z)$ shown in Fig 5.8 by converting the (r, θ) coordinate to an (x, y) coordinate . The electrical field reflected by the object is

$$E_r(x, y; x_s, y_s; -z) = E_{il}(x, y, z)R(x - x_s, y - y_s, z),$$ (5.14)

where -z means that the reflected beam is propagating back towards the fiber. It is efficient to deal with the propagation in the spatial frequency domain because the electric field after the axicon is given as a function of spatial frequency. The reflected electric field in the spatial frequency domain can be derived using a convolution as

$$\widetilde{E}_r(\xi, \eta; x_s, y_s; -z) = \widetilde{E}_{il}(\xi, \eta, z) \otimes \left[e^{-i2\pi\xi x_s} e^{-i2\pi\eta y_s} \widetilde{R}(\xi, \eta, z) \right],$$ (5.15)

where $\exp(-i2\pi\xi x_s)\exp-(i2\pi\eta y_s)\widetilde{R}(\xi, \eta, z)$ is the Fourier transform of $R(x - x_s, y - y_s, z)$. To find the electric field at the z=0 plane shown in Fig. 5.8, each x-y 2D field at -z is propagated with its own phase accumulation by $z\sqrt{k^2 - (2\pi\xi)^2 - (2\pi\eta)^2}$. The fields $\widetilde{E}_{rp}$ at the z=0 plane in spatial frequency domain are described for each x-y 2D field at –z and are given as

$$\widetilde{E}_{rp}(\xi, \eta; x_s, y_s; \Delta z) = \widetilde{E}_r(\xi, \eta; x_s, y_s; -z)\exp\left(iz\sqrt{k^2 - (2\pi\xi)^2 - (2\pi\eta)^2} \right),$$ (5.16)

where Δz is the absolute distance from the –z plane to the z=0 plane (i.e. $\Delta z = |-z|$). The electric field $\widetilde{E}_{rp}(\xi, \eta; x_s, y_s; \Delta z)$ expressed in the spatial frequency domain then takes a convolution with the Fourier transform of a phase modification $k\sqrt{x^2 + y^2}\sin\beta(x, y)$ by the

108

axicon, where $\beta(x,y)$ is given in Eq. (5.4). $\beta(x,y)$ can be derived directly by coordinate transformation using the relation $x = r \cdot \cos\theta$, $y = r \cdot \sin\theta$. So the electric field $\tilde{E}_o$ right through the axicon is given by

$$\tilde{E}_o(\xi,\eta;x_s,y_s;\Delta z) = \tilde{E}_{rp}(\xi,\eta;x_s,y_s;\Delta z) \otimes FT\left[circl\left(\frac{x}{r_{max}},\frac{y}{r_{max}}\right)\exp\left[ik\sin\beta(x,y)\cdot\sqrt{x^2+y^2}\right]\right],$$

$$(5.17)$$

where $circl(x,y)$ is the pupil size of the axicon with a clear aperture radius r_{max} and defined by

$$circl\left(\frac{x}{r_{max}},\frac{y}{r_{max}}\right) = \begin{array}{l} 1 \ \text{for} \ x^2 + y^2 \leq r_{max}^2 \\ 0 \ \text{otherwise} \end{array}, \qquad (5.18)$$

The electric field $\tilde{E}_o$ is then distributed at the tip of the fiber after propagating through the *2f* system with the relation given by [Goodman 1996]

$$E_t(x,y;x_s,y_s;\Delta z) = \frac{1}{i\lambda f}\cdot\tilde{E}_o(\xi,\eta;x_s,y_s;\Delta z)\Big|_{\xi=\frac{x}{\lambda f},\eta=\frac{y}{\lambda f}}, \qquad (5.19)$$

As a last step the powers P_f for each point (x_s,y_s) coupled into the fiber are calculated by the squared modulus of the overlap integral with the fundamental mode of the single mode fiber [O. Wallner 2002].

$$E_d(x_s, y_s; \Delta z) = \int\!\!\int\limits_{-\infty}^{\infty} E_t(x, y; x_s, y_s; \Delta z) \cdot E_f(x, y) dxdy , \qquad (5.20)$$

where $E_f(x, y)$ is the fundamental mode in a single mode fiber, given in Eq. (5.1).
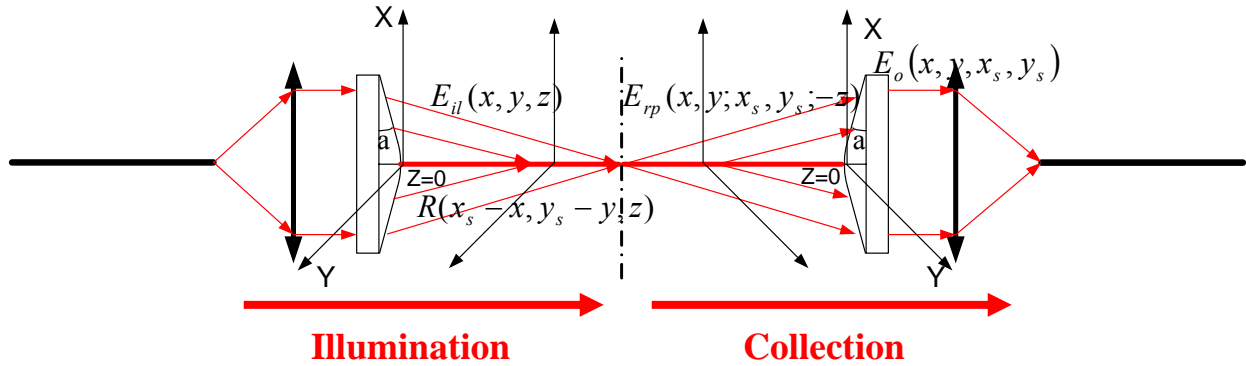
Figure 5.8 : The schematic showing the two steps of illumination of the object of interest and collection of the reflected beam by object. The optics and the geometry in both sides of the middle dot-dash line are the same. The dot-dash represents the plane of symmetry for unfolding the optical path.

5.1.2   *Simulation*

The simulation model for imaging using Bessel beam propagation was applied with the simulation parameters shown in Table 5.1 and a simplified object that corresponds to a continuous point reflector along the z dimension, which is defined as the product of two 1D delta functions.

$$R(x, y; z) = \delta(x)\delta(y) . \qquad (5.21)$$

110

In this case of a continuous point reflector described as a purple line in Fig. 5.9, it is more straightforward to calculate the electric field in the spatial domain until right after the axicon. If the reflector is located on axis, the (r,θ) coordinate is suitable because the electric fields are rotationally symmetric. The reflected electric field E_r by a point reflector on axis away from the axicon by a distance Δz is obtained by inserting the Eq. (5.21) into Eq. (5.14) as

$$E_r(r; r_s = 0; \Delta z) = E_{il}(r = 0; z = \Delta z)\delta(r) \ . \tag{5.22}$$

The propagated electric field to the axicon may be derived using Rayleigh Sommerfield diffraction [Goodman, 1996].

$$E_{rp}(r; r_s = 0; \Delta z) = \frac{E_r(r; r_s = 0; \Delta z)}{j\lambda} \frac{e^{jk\sqrt{z^2 + r^2}}}{\sqrt{z^2 + r^2}} \cdot \left(\frac{z}{\sqrt{z^2 + r^2}}\right) \ . \tag{5.23}$$

The electric field at the tip of the fiber after the phase modification by the axicon and Fourier transform via a *2f* system is given by

$$E_t(r; r_s = 0; \Delta z) = \frac{1}{i\lambda f} \cdot FT \left[\begin{array}{c} \dfrac{E_r(r; r_s = 0; \Delta z)}{j\lambda} \dfrac{e^{jk\sqrt{z^2 + r^2}}}{\sqrt{z^2 + r^2}} \cdot \left(\dfrac{z}{\sqrt{z^2 + r^2}}\right) \\ \cdot \left[circl\left(\dfrac{r}{r_{max}}\right) \exp(ik \sin \beta(r) \cdot r) \right] \end{array} \right]_{\rho = \frac{r}{\lambda f}} \ . \tag{5.23}$$

The Fourier-Bessel transform (i.e. zero-order Hankel transform) can be used for the Fourier transform because the field is rotationally symmetric. To make the numerical computation of Eq.

(5.23) simple avoiding 2D Fourier transforms, the electric fields generated from the scanned

point reflectors by Xs are derived geometrically from the image by the on-axis point reflector

assuming no off-axis aberration. The shifted point reflector is imaged on the plane of the fiber

end with the same point spread function on-axis scaled by m also shifted by mXs, where m is

magnification of the collection optics. The magnification m may be described by β / β', and m is

dependent of the distance Δz. For example, m for the reflector away from $\Delta z1$ is β / β_1' while m

for the reflector away from $\Delta z2$ is β / β_2' as shown in Fig 5.9. The purple bar shown in Fig. 5.9 is

the scanned object by Xs. For simplification, E_d is calculated with the assumption that the single

mode fiber is a point detector (i.e. $E_f(r) = \delta(r)$).

$$E_d(r_s;\Delta z) = \int_{-\infty}^{\infty} E_t(r;r_s;\Delta z) \cdot \delta(r)dr = E_t(0;r_s;\Delta z), \qquad (5.24)$$

The simulation result is shown in Fig. 5.10. The corresponding illumination peak intensities of

the first sidelobes to z=1 mm, 2 mm, 4 mm, and 6 mm are suppressed by about 20 dB after

confocal detection.
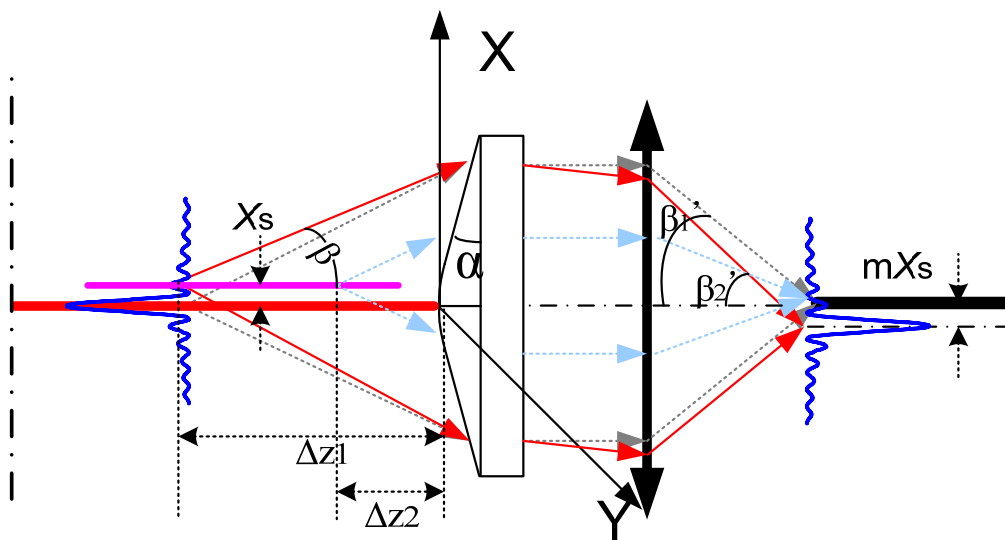
Figure 5.9 : The detection schematic for the scanned point reflector and the magnification depending on the distance Δz
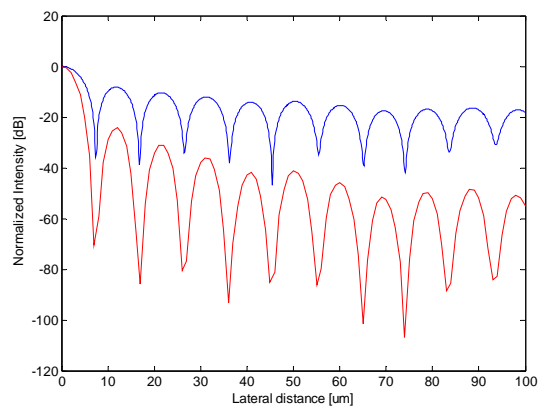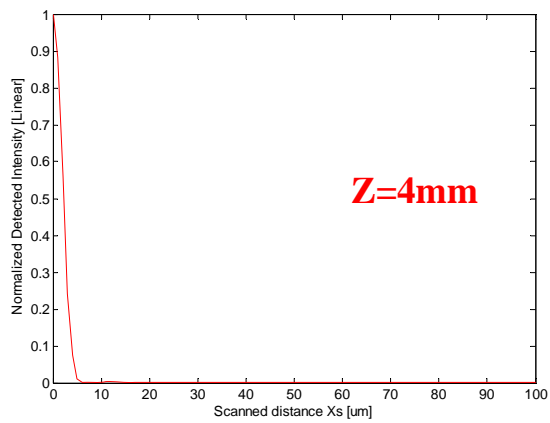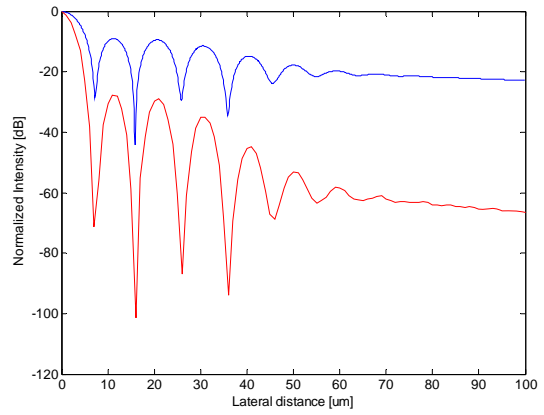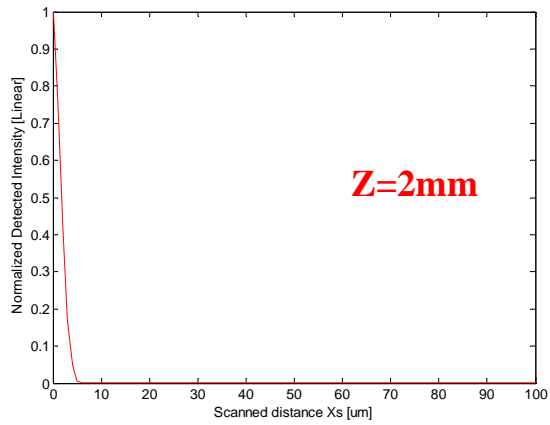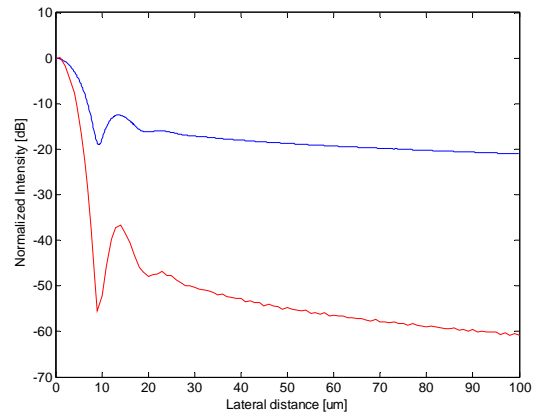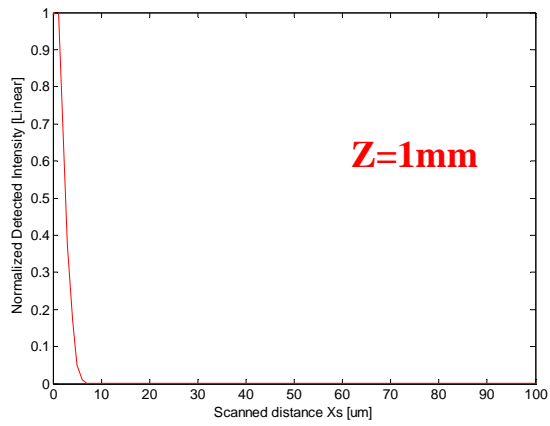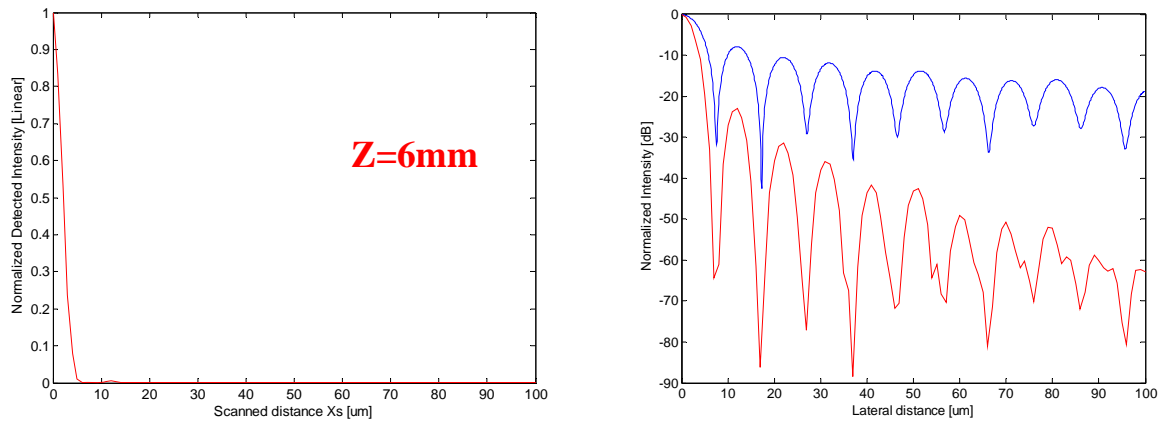
Figure 5.10 : Normalized detected intensity plots in linear scale and dB scale (Red line) with respect to the scanned distance *X*s and comparison with the illuminated point spread function (Blue line) in dB scale for z=1 mm, 2 mm, 4 mm, and 6 mm

5.2 Comparison between Bessel Beam OCT and Gaussian Beam OCT

Optical coherence tomography (OCT) is an imaging modality that provides *in vivo*, noninvasive, high resolution cross-sectional images of biological tissues. Even with the limited the depth of penetration of a light beam through biological tissue, endoscopic probes are valuable for interrogating the condition of wall linings within organs such as the lung, the stomach, the colon, and larger arteries inside the body. After the first endoscopic applications of OCT in 1996, various types of endoscopic OCT instruments were developed [Xie 2006; Rolland 2005]. Current endoscopic probes use Gaussian beam illumination. Some are moved to the targeted location by pushing and pulling a wire outside the body that guides the catheter. These types of probes operate at low numerical aperture and therefore provide limited ~20 μm lateral resolution. Other probes use higher numerical aperture optics, however they suffer from a shorter depth of focus (DOF) (i.e., measured as the confocal parameter) (e.g., ~140 μm confocal parameter for ~5 μm

FWHM lateral resolution at 800 nm). For these probes, a fine focus adjustment is required that cannot be achieved by pushing and pulling a wire. A GRIN lens rod based probe was developed to focus on a targeted location in a sample by moving a stage outside the body [Xie 2006]. However the non-flexible rod limits some endoscopic applications. Thus the development of extended DOF imaging schemes is an active area of OCT research [Meemon 2008; Murali 2007]. Bessel beam imaging, generated by axicon optics, is distinguished from Gaussian beam imaging in that it enables extension of the focusing range without loss of resolution [McLeod 1954]. The trade-off is a decrease in illumination and collection efficiency, and thus associated imaging sensitivity. While the use of axicon optics in time domain OCT was first investigated by Ding et al, [Ding 2002] no imaging in biological samples was demonstrated. Recently, using FD OCT, Leitgeb et al. proposed an imaging scheme for imaging in biological samples where the illuminating light path was achieved using an axicon lens together with imaging optics to achieve high resolution and an extended DOF, and the light was collected via a beam splitter using a conventional objective to increase imaging sensitivity compared to a double pass axicon imaging system [Leitgeb 2006]. Researchers reported 1.5 μm resolution across a 200 μm DOF. However, this is still a rather limited DOF and the space required to allow another beam path for collecting the backscattered light prohibits the scalability of the approach for application to endoscopy. In this chapter, we report on the measured resolution and sensitivity achieved with a custom-made microoptic axicon lens designed to theoretically achieve an 8 mm DOF. A measured invariant resolution of ~ 8 μm is demonstrated across a 4 mm measured DOF using the microoptic axicon, while achieving an invariant sensitivity of ~ 80 dB with a 25 mW input power. Double-pass Bessel-beam Spectral Domain Optical Coherence Tomography with an axicon microoptic (i.e.,

116

<1 mm in diameter) is for the first time demonstrated in a biological sample demonstrating invariant resolution and SNR across a 4 mm measured DOF. This is compared to a comparable Gaussian beam imaging system.

5.2.1 Depth of Focus and Lateral Resolution and Sensitivity in Bessel-beam OCT

We quantify both sensitivity and resolution and demonstrate imaging in biological tissue. An axicon microoptics lens with an apex angle of 170 degree illuminated with a 600 μm diameter Gaussian beam (i.e., diameter of the beam at $1/e^2$ intensity) was incorporated into the sample arm of a FD-OCT setup to test its performance. The two basic types of FD-OCT layouts (i.e., Spectrometer-based OCT and Swept-Source-based OCT) can benefit equally from the extended depth of focus generated by a Bessel beam. The first type of FD-OCT (i.e, Spectrometer-based OCT) was used for all measurements reported here provided the availability of a broadband femtolaser source in our laboratory. As shown in Fig. 5.11, the FD-OCT system consists of a high power broad bandwidth Ti:Sa laser centered at 800 nm with 120 nm FWHM (Femtolasers Inc., Integral), a commercial spectrometer with a 3648 line CCD array (Ocean Optics Inc, HR4000), and a broadband custom-made 80/20 (NSF-DARPA/PTAP program) fiber coupler that feeds the two arms of a Michelson interferometer. In this configuration, 80% of the beam from the coupler is collimated and then incident on the microoptic axicon lens. The light beam exiting the axicon is a Bessel type that propagates to the sample. The other 20% of the beam is reflected by a mirror through a Fourier-domain optical delay line that is used to compensate the overall dispersion of the system [Lee 2005].

117
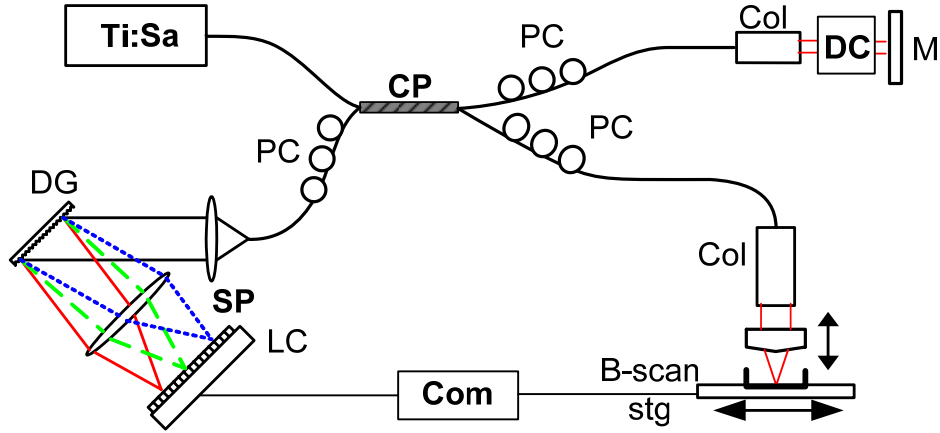
Figure 5.11 : A schematic diagram of the custom built Bessel beam based FD-OCT system. CP : fiber coupler, PC : polarization controller, Col : collimator, DC : dispersion compensation, DG : diffraction grating, LC : line ccd, SP : spectrometer, M : mirror, and B-scan stg : automatically B-scanning translation stage.

The DOF generated by illuminating the axicon with a 600 μm collimated Gaussian beam (full width at $1/e^2$) is that of a Bessel beam and is calculated to be 8 mm according to

$$DOF_B \cong R \cdot (\cot \beta - \tan \alpha),\qquad(5.25)$$

where R is the incident beam half diameter, α is the edge axicon angle (5 degree), and β is the beam deviation angle (2.24 degree) with respect to the optical axis. The axicon gives a central peak radius of 7.7 μm at 800 nm (i.e., the first zero radius from the center of the Bessel beam, which is also the lateral resolution according to the Rayleigh resolution criterion) given by

$$r_0 = 2.4048\lambda / 2\pi \sin \beta,\qquad(5.26)$$

where λ is the central wavelength. This central peak radius is invariant throughout the DOF for Bessel beams. The central peak radii along the DOF were compared to the FWHM beam diameters (i.e., a standard lateral resolution metric for Gaussian beams) formed by a conventional lens of focal length f of 8 mm operating at a Numerical Aperture (NA) of 0.037 that yields an $1/e^2$ intensity beam waist radius of 6.9 μm (i.e., 8 μm FWHM) at the focus plane. This lens has approximately a 400 μm depth of focus (i.e., two times the Rayleigh range) given by

$$DOF_G \cong 2\pi \cdot \omega_0^2 / \lambda, \qquad (5.27)$$

where ω_0 is the $1/e^2$ intensity beam waist radius.

The lateral resolution, measured as the central peak radius for the axicon and the FWHM for the conventional lens, was measured over the focal region of interest with a CCD imaging camera of 1004 by 1002 pixels and 8 μm by 8 μm pixel size (Andor Technology Inc., VP885KCS) placed at different axial positions. These positions are recorded on the x-axis of Fig. 5.12 as the relative axial distances d with respect to the medial positions of the two optics' respective DOF. The medial position m_0 of the DOF generated by the axicon is 4 mm from the axicon apex, around which the measured depth of focus is +/-2mm. The lateral resolution values are reported on the y-axis of Fig. 5.12. Results show that the axicon achieves an ~ 8 μm invariant lateral resolution across a much larger depth range compared to the 0.037 NA conventional lens.
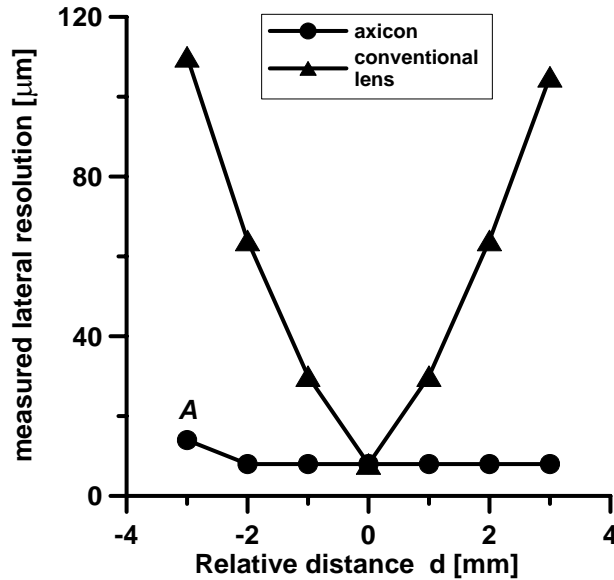
Figure 5.12 : Measured lateral resolution over the focal range parameter *d* using either a microoptics axicon of 170 degree apex angle illuminated by a 600 μm collimated beam or an 8 mm focal length lens operating at a NA of 0.037. Point A corresponds to the focus depth associated with the rounded apex of the axicon lens

The chromatic dispersion created by the 5 degree edge angle axicon was investigated and found to be negligible since the wavelength dependent maximum refraction angle deviation was assessed to be 0.009 degree (i.e., corresponding to a relative error of 0.4%) over the 120nm source bandwidth using optical raytracing software.

We shall now compare the imaging sensitivities for both optics. For Gaussian beam imaging (using the conventional lens), the peak sensitivity was measured at the focal plane of the lens where a mirror was used in place of a biological sample; an 101 dB peak sensitivity was measured with an incident power of 25 mW. This measurement was done with a difference in optical path length of 1 mm between the sample mirror and the reference mirror. For the Bessel beam imaging (using the axicon), the independent measurements of illumination efficiency (i.e,

resulting from focusing a beam with the axicon) and collection efficiency (i.e, resulting from the light collimated by the axicon from an equivalent scattering sample) are required, from which sensitivity can be computed. These measurements need however to be made for both optics given that the Gaussian beam imaging layout serves as a reference. Starting with measuring the intensity along the depth axis after each lens, illumination efficiency will be derived via normalization. The on-axis intensity distributions at the different axial positions were measured with the CCD camera for both optics and normalized by the incident intensity I_0.

Fig. 5.13 shows the measured intensities normalized to the peak intensity of the focused Gaussian beam at its focal point. These measured values are in good agreement with the theoretical normalized on-axis intensities distributions for the axicon given by

$$I_B(d)/I_G(0) = \left(4\pi^2\beta^2(d+m_0)/\lambda\right) \cdot \exp\left[-2\beta^2(d+m_0)^2/R^2\right]/I_G(0), \qquad (5.28)$$

and those for the conventional lens are given by

$$I_G(d)/I_G(0) = \left(\pi^2\omega_0^4 + \lambda^2 f^2\right)/\left(\pi^2\omega_0^4 + \lambda^2 d^2\right)/I_G(0). \qquad (5.29)$$

These normalized intensity values define the illumination efficiencies, which are reported as a function of the relative distance d. Note that the illumination efficiency at the Gaussian beam waist is 100%, or zero dB, by definition.
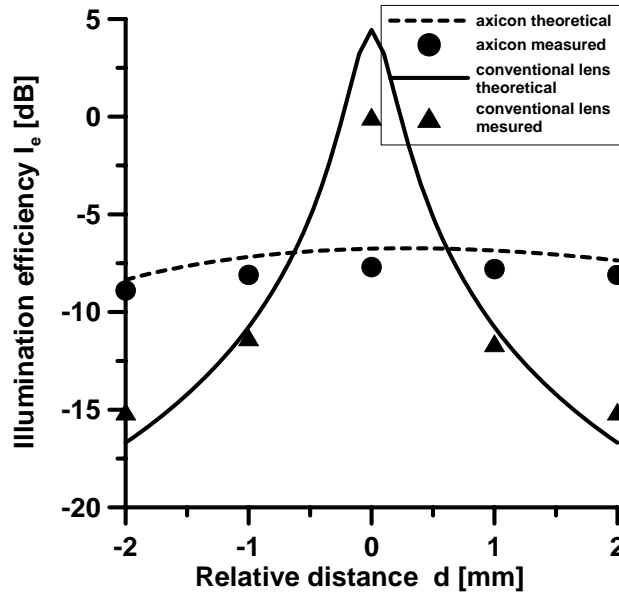
Figure 5.13 : Illumination efficiencies versus *d*

To measure collection efficiencies, we collimated the source and created a 0.12 NA focused beam (using an EC Plan NeoFluor, Zeiss Inc. combined with an iris). This setup simulates an angular distribution of the light after scattering that needs to be collected back by the axicon. The beam was then collimated by either the axicon or the conventional lens and coupled to the sample arm of the SD-OCT interferometer as shown in Fig. 5.14
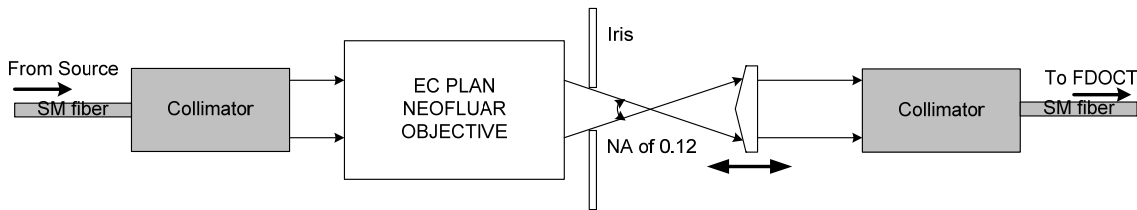
Figure 5.14 : Setup to measure collection efficiencies
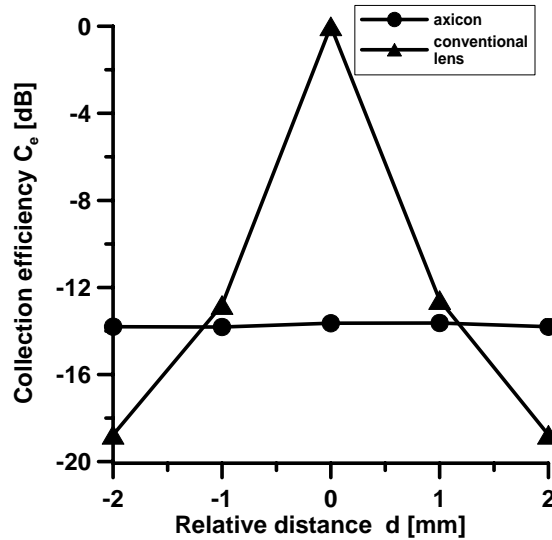
Figure 5.15 : Measured collection efficiencies versus *d*

The collected power at the various relative positions *d* was measured using a power meter connected to the detector arm of the SD-OCT interferometer. Each power value was then normalized by that of the conventional lens at its focal point as shown in Fig. 5.15. These normalized values define the collection efficiencies.

Next, we estimate the axial sensitivities of the Bessel beam layout along the dimension *d* from the measured peak sensitivity of 101 dB reported above for the conventional lens system. In Fig. 5.16 the reported sensitivities for the axicon optics versus *d* over its DOF were computed by subtracting the measured illumination and collection efficiencies from the measured 101 dB established for the conventional lens. The sensitivity of the Bessel beam SD-OCT is higher than that of the conventional lens when the sample is located beyond 1mm. Together with the reported resolution in Fig. 5.13, the measured performance demonstrates the advantage of Bessel beam imaging when an extended DOF is required.
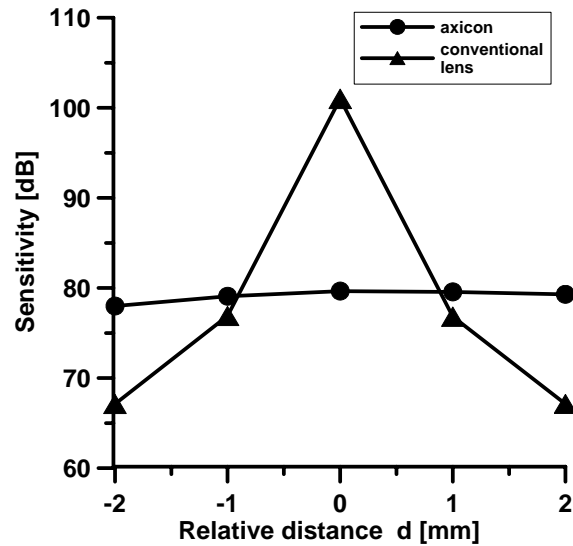
Figure 5.16 : Measured system sensitivities versus *d*

5.2.2   Biological Sample Imaging

The exceptional effectiveness of implementing an axicon microoptic in a FD-OCT system has been demonstrated by imaging a biological sample, specifically an African frog (Xenopus laevis) tadpole, at various positions *d* acquired with the same incident power of 25 mW and exposure time of 50 μs. The reference arm mirror was adjusted to be within the imaging depth capability of the CCD (i.e., ~2mm imposed by the CCD resolution) and specifically, the reference mirror was located 1 mm in optical path length from the center of the images. The Bessel beam images in Fig. 5.17(a) show invariant resolution and SNR over at least a 4 mm focal range, while the Gaussian beam images shown in Fig. 5.17(b) are already out of focus for *d* equal 1 mm.
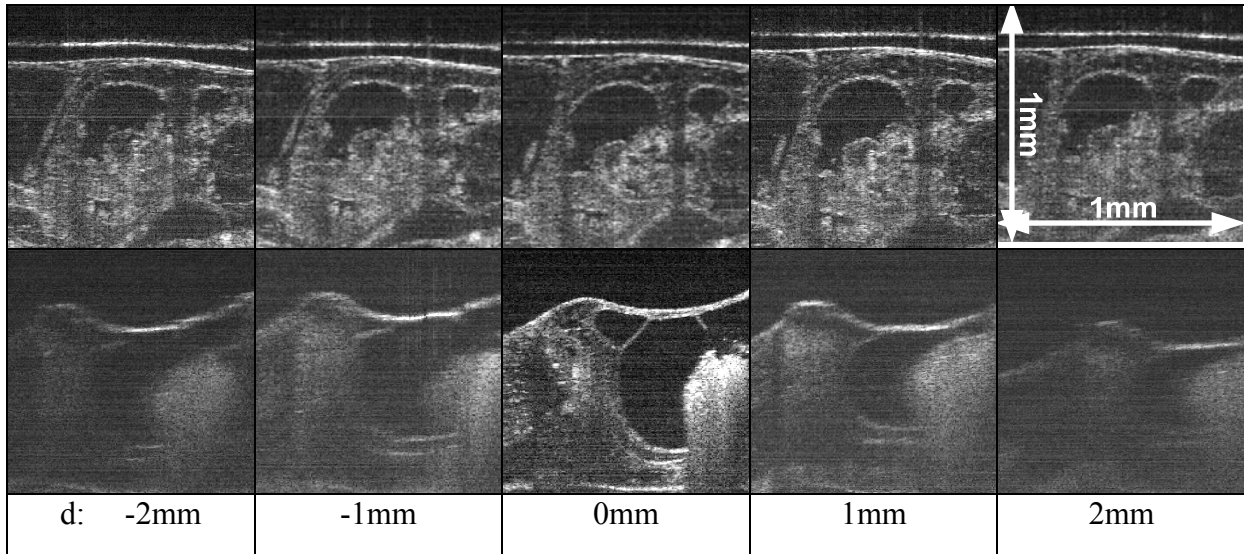
Figure 5.17: (a) 1 mm x 1 mm SD-OCT images of an African frog (Xenopus laevis) tadpole versus *d* acquired using (Top row) a 600 μm effective diameter axicon lens and (Lower row) a 0.037 NA conventional lens.

CHAPTER SIX: DESIGN AND FABRICATION OF A MICROMOTOR AND AXICON BASED CATHETER

In this Chapter, a manufacturable 5 mm biophotonic catheter was conceived to include collimation optics, a 3mm custom design fused silica axicon lens (the axicon used in Chapter 5), and custom design imaging optics combined with a 2mm outer diameter micromotor coupled to a mirror to yield a full 360 degree scan within concave structures such as arteries, lung lobes, and other internal structures. A schematic diagram and ray trace for the axicon based micromotor probe is shown in Fig. 6.1. The axicon has a 5 degree axicon angle that gives 8 μm transverse resolution computed as the central peak radius of the Bessel beam calculated from $\rho_0 = 2.4048\lambda / 2\pi \sin\beta$, where β is the beam angle with respect to the optical axis after the axicon, and λ is the central wavelength of the light source. Two spherical lenses are used to relay the depth of focus generated directly from the axicon to the area of the targeted specimen to be imaged. The relayed depth of focus was located between 0.8 mm and 2.4 mm beyond the outer surface of the catheter. The effective focal length (f_1) of the first lens is 2.4 mm and the effective focal length (f_2) of the second lens is 1.6 mm. The angle β is increased by (f_1/f_2) which improves the transverse resolution (i.e. ~5 μm) in the same ratio; however the two lenses decrease the depth of focus however by $(f_1/f_2)^2$. The positive outcome is that it confines the power within a smaller area compared to having no relay lenses, which yields more power efficiency.
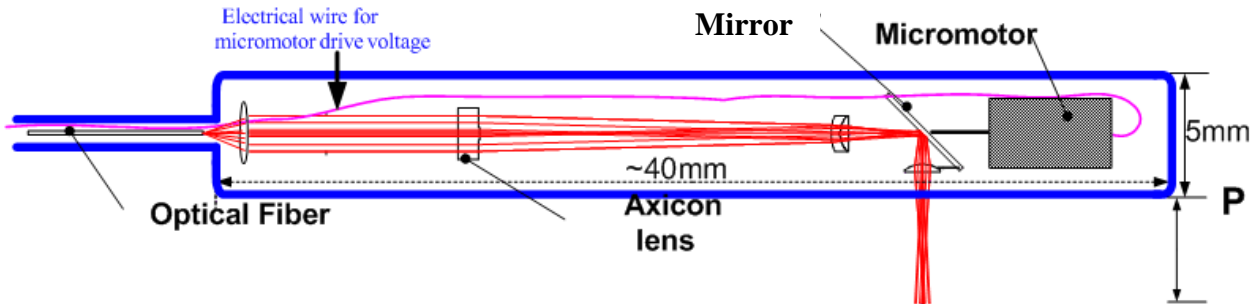
Figure 6.1 : Schematic of a 5 mm diameter catheter

Fig. 6.2 (a), (b), and (c) show the point spread functions (PSFs) at the focus planes of 0.8 mm, 1.6 mm, and 2.4 mm from point P shown in Fig. 6.1. The central peak radius (i.e. the first zero of the Bessel function) of the corresponding point spread functions are 5.5 μm, 5.1 μm, and 4.9 μm, respectively. Furthermore, the relative intensities are 78% and 69% of the peak intensity of the PSF at 1.6 mm for the focus planes of 0.8 mm and 2.4 mm, respectively.

(a)

(b)

(c)
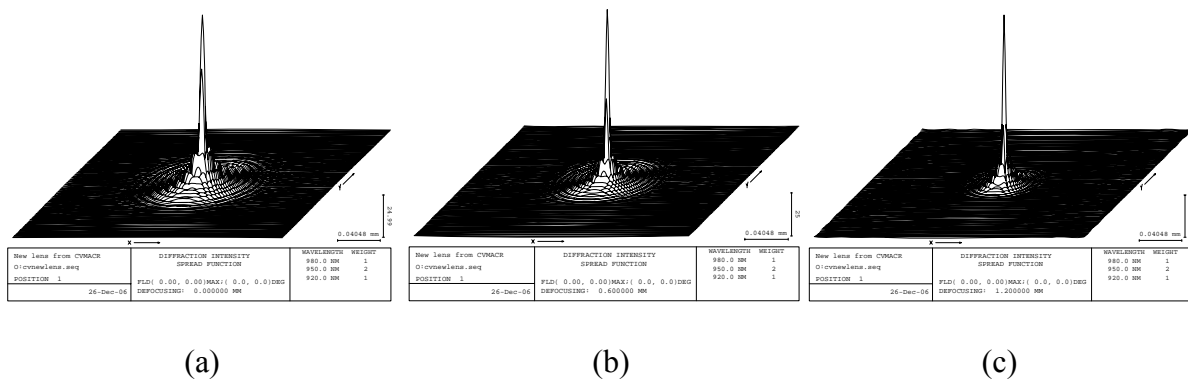
Figure 6.2 : Point spread functions at focus planes of (a) 0.8 mm (b) 1.6 mm (c) 2.4 mm from the point P

Fig. 6.3 (a) shows the optomechanical drawings of the axicon-based micromotor endoscope catheter probe assembly. A 2.5 mm outer diameter collimating optics was pigtailed

with a single mode fiber. A commercially available 2 mm outer diameter micromotor was integrated. In order to reduce the back reflected noise from the endoscope optics components, which reduces the dynamic range of the CCD camera, an optical gel was placed between the collimator and the axicon to eliminate the reflection of the first surface of the axicon. The refractive index (i.e. 1.45) of the optical gel is similar to the index of the axicon material (i.e. Fused silica). The optimized double convex lenses for reducing the aberration of the relay optics also minimized back reflections compared to plano surfaces in plano-convex lenses. Precisely-adjustable centering screws were set on each housing of the collimator, the axicon, and the first small lens to align the incident beam with the optical axis of each optical component because the performance of the axicon making Bessel beams is strongly dependent on alignment. Another key novelty of the design lies in the attachment of a microlens to a micromotor in order for the beam to stay focused as it rotates. As shown in Fig. 6.3 (b), the microlens was attached to a 45-degree-wedged ferrule via a micromachined lens holder that is connected to the shaft of the micromotor. When the micromotor spins, a beam that scans full 360 degrees was obtained. The spacer around the shaft was inserted for better connection between the ferrule and the micromotor shaft. The fabricated catheter is shown in Fig. 6.4.
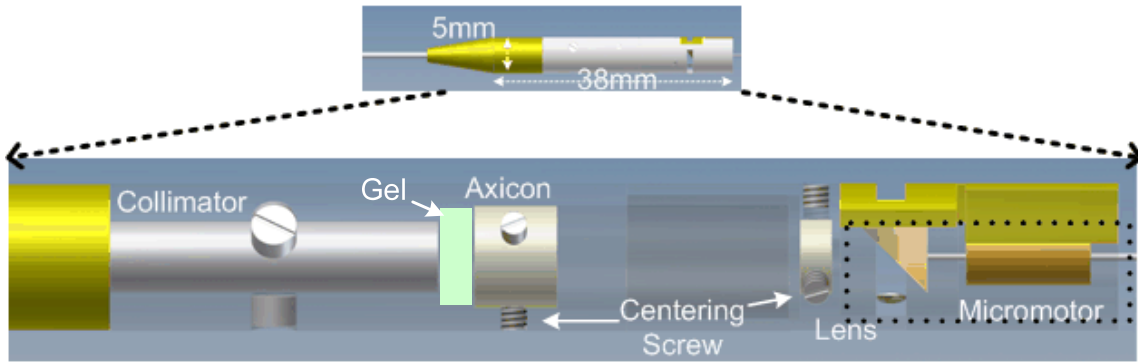
(a)
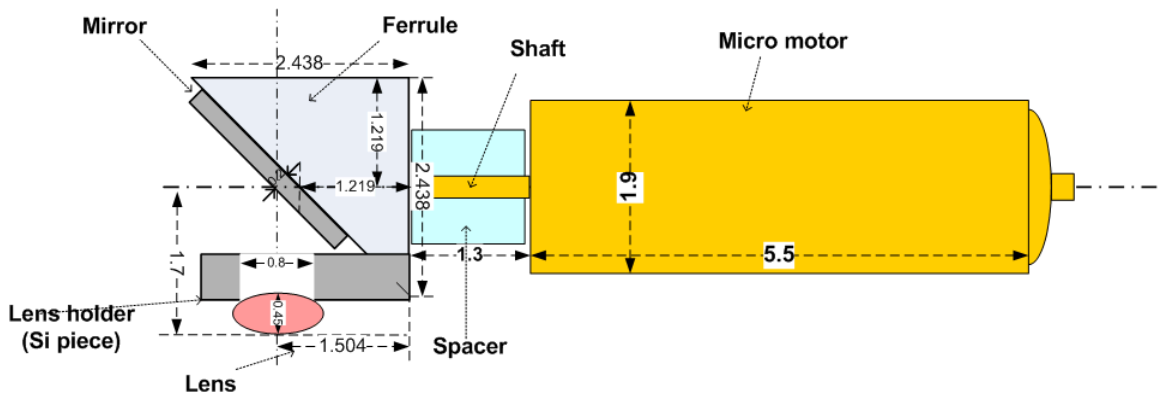
(b)

Figure 6.3 : (a) Side view of the optomechanical catheter assembly in the real size and enlarged clear view of the assembly (b) detail view of the dotted line box.

Figure 6.4 : Fabricated 5mm outer diameter catheter assembly

CHAPTER SEVEN: SUMMARY OF CONTRIBUTIONS AND CONCLUSION

Optical coherence tomography and microscopy are emerging technologies requiring advanced engineering to bring the technology to market across multiple applications, where new science will be enabled. Engineering advances lie in achieving high resolution not only axially with the design of new light sources but also laterally with the optical design and fabrication of state of the art optical imaging probes. The development and optimization of imaging architectures to address key imaging issues such as dispersion compensation, achieving extended depth of focus, the removal of mirror images at high speed, means of achieving high sensitivity, and methodology to assess image quality according to various generic tasks that may be defined across various applications [Rolland, 2005] all represent areas where improvements are needed and possible..

This dissertation describes three major contributions to endoscopic FD-OCT imaging with high axial, high lateral, and extended depth of focus: (1) The implementation of a novel system that enables full range depth imaging without a loss in acquisition speed, (2) A theoretical and experimental investigation of compensation of overall system dispersion with a Fourier domain optical delay line (FD ODL) to keep the axial resolution determined by the coherence length of a broadband source, and (3) The design, development, and experimental analysis of Bessel beam based OCT to achieve high lateral resolution over an extended depth of focus including a theoretical analysis of Bessel-beam based confocal scanning optical microscopy (BCSOM).

In the development of high axial resolution OCT using a broadband source for endoscopic imaging, the imaging depth of FD OCT is limited by spectral resolution that is calculated by dividing the bandwidth of the source by the number of pixels of a spectrometer. As the bandwidth of the source gets broader; the imaging depth gets shorter for the same number of pixels of a spectrometer [Hausler, 1998]. At a minimum, the imaging depth in OCT should be able to cover the depth of focus determined by the focusing optics.

The reduced imaging depth caused by the presence of mirror images may be doubled without upgrading the system by removing the mirror images generated from the Fourier transform of the detected real valued spectra. We designed and developed a novel FD-OCT system that we refer to as the dual-reference full-range FD-OCT (DR-FROCT) that enables doubling the imaging depth without a loss in acquisition speed. The system achieves 5 mm imaging depth with 8 μm axial resolution. In addition, DR-FROCT may be less sensitive to phase error generated by involuntary movements of the subject compared to the other established full range OCT systems because it uses two signals with phase difference of $\pi/2$ obtained simultaneously from two reference arms to remove mirror images.

In an effort directed at improving the axial resolution, we developed a mathematical model of the OCT signal that includes the effects of phase modulation including phase delay, group delay, and dispersion. This model led us to install a Fourier domain optical delay line (FDODL) into the reference arm of the OCT system. This resulted in a method that compensates overall system dispersion with an FDODL to keep the axial resolution limited only by the coherence length of a broadband source.

A challenge to endoscopic imaging remains the inability to maintain sufficient depth of focus when focusing a light beam with high numerical aperture optics to achieve high lateral resolution. The resulting short depth of focus requires refocusing, which is not practical for high speed *in vivo* imaging. In addition, the limited space of an endoscopic catheter requires compact optics that again does go against high resolution with long depth of focus. A potential solution to these issues is to resort to Bessel beams or quasi-Bessel beams imaging that enable quasi-invariant PSF and associated lateral resolution throughout the depth of focus of the imaging optics. In practice, Bessel-beam imaging may be achieved with axicon optics, which requires to be used in double pass when used for endoscopic imaging. However, there can be questions such as "Is it possible to get enough sensitivity when imaging highly scattering specimen like biological samples?," and "How does the non negligible sidelobes of the Bessel beams affect the images?".

We demonstrated in this dissertation that the side lobes of the lateral PSF, which is the Bessel function generated by an axicon, are suppressed in a confocal imaging geometry that results from an imaging interferometer built using single mode fiber. The imaging technique is referred to as Bessel-beam based confocal-scanning optical microscopy (BCSOM). Experimentally, we reported invariant lateral resolution of ~ 8 μm across a 4 mm measured depth of focus (DOF) using a microoptics axicon, while achieving an invariant sensitivity of ~ 80 dB with a 25 mW input power. Furthermore, a double-pass Bessel-beam FDOCT with an axicon microoptic (i.e., <1 mm in diameter) was demonstrated for the first time in a biological sample, where we demonstrated invariant resolution and SNR across a 4 mm DOF, which was compared to Gaussian beam imaging.

Currently, the DR-FROCT is being tested in biological samples. Such samples present a non planar front surface, thus the later can not be used for the proportional-integral-derivative (PID) controller necessary to set a constant $\pi/2$ phase difference between the two interference signals created using two phase shifted reference arms in order to remove the mirror images. This issue can be solved using another mirror in the sample arm. It may be needed to develop systems exclusively used for PID control together with signal processing to keep the high acquisition imaging speed. As we target the next generation endoscopic systems to specific clinical applications, we will design and fabricate various axicon-based catheters. Some applications may only require 1-5 mm catheters, while some applications may push the technology to accommodate requirements for catheters of less than 1 mm in diameter. Approaches where axicons are fabricated at the tip of fibers may yield yet new performance imaging probes. Importantly, Bessel-beam imaging catheter will enable high lateral resolution over an extended depth of focus.

APPENDIX: DERIVATION OF THE PHASE MODULATION IN FD ODL

A. Zvyagin and D. Sampson *et. al.* [Zvyagin 2003] derived the phase difference $\Delta\phi(\omega,t)$ in FD-ODL between the phase acquired by a ray of arbitrary frequency ω when $\theta(t)$ is non zero and the phase acquired when $\theta(t) = 0$, i.e.,

$$\Delta\phi(\omega,t) = \frac{2\omega\Delta z}{c}\cos\beta + \frac{2\omega x_0\theta(t)}{c} - \frac{2\omega\theta(t)f}{c}\sin\beta, \qquad (A1)$$

where $\theta(t)$ and β are shown in Fig. A.1
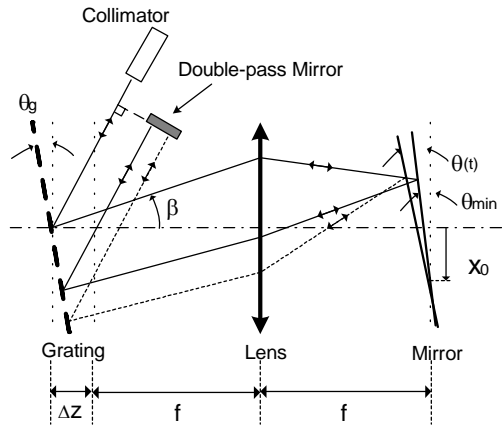
Figure A.1: Schematic diagram of the double-pass FD-ODL in the case of a grating tilted from the normal and offset from the focal plane.

Eq. (A1) is changed for a double-pass FD-ODL in Fig. A1 to

$$\begin{aligned}
\Delta\phi_{odl}(\omega,t) &= \frac{4\omega\Delta z}{c}\cos\beta + \frac{4\omega x_0\Delta\theta(t)}{c} - \frac{4\omega\Delta\theta(t)f}{c}\sin\beta, \\
&= \frac{4\omega\Delta z}{c} - \frac{8\omega\Delta z}{c}\sin^2\frac{\beta}{2} + \frac{4\omega x_0}{c}\Delta\theta(t) - \frac{4\omega\Delta\theta(t)f}{c}\sin\beta,
\end{aligned} \qquad (A2)$$

where $\Delta\theta(t) = \theta(t) - \theta_{min}$.

The grating equation can be used to replace $\sin\beta$ in Eq. (A2), which is given by

$$p\left[\sin(\beta + \theta_g) - \sin\theta_g\right] = 2\pi mc\left(\frac{1}{\omega} - \frac{1}{\omega_0}\right).$$ (A3)

The $\Delta\phi_{odl}(\omega, t)$ in a double-pass FD-ODL is the phase difference between the phase acquired by

a ray of arbitrary frequency ω when $\theta(t)$ is nonzero and the phase acquired when $\theta(t)$ is θ_{min}.

We can then express the phase delay $t_p(t)$, the group delay $t_g(t)$, the first-order group delay

dispersion $D_\omega(t)$, and the second-order group delay dispersion $D_\omega^{(1)}(t)$ in a double-pass FD-

ODL according to their definitions as

$$t_{p\_odl}(t) \equiv \frac{\Delta\phi_{odl}(\omega_0, t)}{\omega_0} = \frac{4\Delta z}{c} + \frac{4\Delta\theta(t)x_0}{c},$$ (A4)

$$t_{g\_odl}(t) \equiv \frac{\partial\left[\Delta\phi_{odl}(\omega, t)\right]}{\partial\omega}\Big|_{\omega=\omega_0} = \frac{4\Delta z}{c} + \frac{4\Delta\theta(t)x_0}{c} + \frac{8\pi\Delta\theta(t)f}{p\omega_0\cos\theta_g},$$ (A5)

$$D_{\omega\_odl}(t) \equiv \frac{\partial^2\left[\Delta\phi_{odl}(\omega, t)\right]}{\partial\omega^2}\Big|_{\omega=\omega_0} = -\frac{16\pi^2 c(\Delta z + f\Delta\theta(t)\tan\theta_g)}{p^2\omega_0^3\cos^2\theta_g},$$ (A6)

$$D_{\omega\_odl}^{(1)}(t) \equiv \frac{\partial^3\left[\Delta\phi_{odl}(\omega, t)\right]}{\partial\omega^3}\Big|_{\omega=\omega_0} = \frac{48\pi^2 c(\Delta z + f\Delta\theta(t)\tan\theta_g)}{p^2\omega_0^4\cos^2\theta_g}(1 + \frac{2\pi c\sin\theta_g}{p\omega_0\cos^2\theta_g}).$$ (A7)

LIST OF REFERENCES

[Abedin 1996] K. S. Abedin, and H. Ito, "Temperature-dependent dispersion relation of ferroelectric lithium tantalite," J. Appl. Phys. 80(11), 6561-6563 (1996).

[Agrawal 1995] G. P. Agrawal, *Nonlinear Fiber Optics* (Academic Press, San Diego, 1995).

[Akcay 2002] C. Akcay, P. Parrein, and J. P. Rolland, "Estimation of longitudinal resolution in optical coherence imaging," Appl. Opt. 41, 5256-5262 (2002).

[Barrett 2004] H. H. Barrett, and K. J. Myers, B.E.A. Saleh. Ed., *Foundations of Image Science*, (Wiley Series in Pure and Applied Optics, Hoboken, New Jersey, 2004).

[Cense 2004] B. Cense, N. A. Nassif, T. C. Chen, M. C. Pierce, S. Yun, B. H. Park, B. E. Bouma, G. J. Tearney, and J. F. de Boer, "Ultrahigh-resolution high-speed retinal imaging using spectral-domain optical coherence tomography," Optics Express 12, 2435-2447 (2004).

[Cizm´ar 2006] T. Cizm´ar, "Optical traps generated by non-traditional beams," Ph.D. thesis, Masaryk University in Brno (2006).

[Ding 2002] Z. Ding, H. Ren, Y. Zhao, J. S. Nelson, and Z. Chen, "High-resolution optical coherence tomography over a large depth range with an axicon lens," Opt. Lett. 27, 243 (2002).

[Fercher 2001] A. F. Fercher, C. K. Hitzenberger, M. Sticker, and R. Zawadzki, "Numerical dispersion compensation for Partial Coherence Interferometry and Optical Coherence Tomography," Optics Express 9, 610-615 (2001), http://www.opticsexpress.org.

[Gaskill 1978] Jack Gaskill, "Linear Systems, Fourier Transforms, and Optics," Wiley-Interscience 1th edition (1978).

[Goodman 1985] J. W. Goodman, *Statistical Optics* (John Wiley&Sons, New York, 1985).

[Goodman 1996] Joseph Goodman, "Introduction to Fourier optics," McGraw-Hill Science 2nd edition (1996).

[Gotzinger 2005] E. Gotzinger, M. Pircher, R. Leitgeb, and C. Hitzenberger, "High speed full range complex spectral domain optical coherence tomography," Opt. Express 13, 583 (2005).

[Grosjean 2005] T. Grosjean, S. Saleh, M. Suarez, I. Ibrahim, V. Piquerey, D. Charraut, and P. Sandoz "Fiber microaxicons fabricated by a polishing technique for the generation of Bessel-like beams," Appl. Opt. 46, 8061 (2005).

[Hausler 1998] Hausler G, Lindner MW. "Coherence radar and spectral radar-New tools for dermatological diagnosis," J. Biomed Opt. 3, 21-31 (1998).

[Hsu 2003] I. Hsu, C. Sun, C. Lu, C. C. Yang, C. Chiang, and C. Lin, "Resolution Improvement with Dispersion Manipulation and a Retrieval Algorithm in Optical Coherence Tomography," Appl. Opt. 42, 227-234 (2003).

[Huang 1991] D. Huang, E. A. Swanson, C. P. Lin, J. S. Schuman, W. G. Stinson, W. Chang, M. R. Hee, T. Flotte, K. Gregory, C. A. Pulifito, and J. G. Fujimoto, "Optical coherence tomography," Science 254, 1178-1181 (1991).

[Kwong 1993] K.F. Kwong, D. Yankelevich, K.C. Chu, J.P. Heritage, and A. Dienes,"400-Hz mechanical scanning optical delay line," Optics Letters 18, 558-561 (1993).

[Lakoba 1999] T. I. Lakoba and G. P. Agrawal, "Effects of third-order dispersion on dispersion-managed solitons," J. Opt. Soc. Am. B 16, 1332-1343 (1999).

[Lee 2005] K. Lee, A. Akcay, T. Delemos, E. Clarkson, and J. Rolland, "Dispersion control with a Fourier-domain optical delay line in a fiber-optic imaging interferometer," Appl. Opt. 44, 4009 (2005).

[Leitgeb 2004] R. A. Leitgeb, W. Drexler, A. Unterhuber, B. Hermann, T. Bajraszewski, T. Le, A. Stingl, and A. F. Fercher, "Ultrahigh resolution Fourier domain optical coherence tomography," Optics Express 12, 2156-2165 (2004).

[Leitgeb 2006] R. Leitgeb, M. Villiger, A. Bachmann, L. Steinmann, and T. Lasser, "Extended focus depth for Fourier domain optical coherence microscopy," Opt. Lett. 31, 2450 (2006).

[Marks 2003] D. L. Marks, A. L. Oldenburg, J. J. Reynolds, and S. A. Boppart, "Autofocus Algorithm for Dispersion Correction in Optical Coherence Tomography," Appl. Opt. 42, 3038-3046 (2003).

[Marks 2003] D. L. Marks, A. L. Oldenburg, J. J. Reynolds, and S. A. Boppart, "Digital Algorithm for Dispersion Correction in Optical Coherence Tomography for Homogeneous and Stratified Media," Appl. Opt. 42, 204-217 (2003).

[McLeod 1954] J. McLeod, "The axicon: a new type of optical element," J. Opt. Soc. Am. 44, 592 (1954).

[Meemon 2008] P. Meemon, K. Lee, S. Murali, and J. Rolland, "Optical design of a dynamic focus catheter for high-resolution endoscopic optical coherence tomography," Appl. Opt. 47, 2452-2457 (2008).

[Murali 2007] S. Murali, K. Lee, and J. Rolland. "Invariant resolution dynamic focus OCM based on liquid crystal lens." Opt. Express 15, 854 (2007).

[Nasr 2004] M. B. Nasr, B. E. A. Saleh, A. V. Sergienko, and M. Teich, "Dispersion-Cancelled and Dispersion-Sensitive Quantum Optical Coherence Tomography," Optics Express 12, 1353-1362 (2004).

[Niblack 2003] W. K. Niblack, J. O. Schenk, B. Liu, and M. E. Brezinski, "Dispersion in a Grating-Based Optical Delay Line for Optical Coherence Tomography," Appl. Opt. 42, 4115-4118 (2003).

[Rolland 2005] J. Rolland, J. O'Daniel, C. Akcay, T. Delemos, K. Lee, K. Cheong, E. Clarkson, R. Chakrabarti, and R. Ferris, "Task-based optimization and performance assessment in optical coherence imaging," JOSA A 22, 1132 (2005).

[Rolland 2008] Rolland, J.P., P. Meemon, S. Murali, A. Jain, N. Papp, K. Thompson, and K.S. Lee, "Gabor Domain Optical Coherence Microscopy," 1st Canterbury Workshop on Optical Coherence Tomography and Adaptive Optics, September 8-10, Proceedings of the SPIE (2008) (invited).

[Rolland 2008] Rolland, J.P., K. Lee, A. Mahmood, L. Fluck, and *et*. *al*., "Collaborative Engineering: 3-D Optical Imaging and Gas Exchange Simulation of In-Vitro Alveolar Constructs," The 16th Annual Medicine Meets Virtual Reality Conference (2008)

[Rollins 1998] A. M. Rollins, M. D. kulkarni, S. Yazdanafar, R. Ungarunyawee, and J. A. Izatt, "In vivo video rate optical coherence tomography," Optics Express 3, 219-229 (1998), http://www.opticsexpress.org.

[Smith 2002] E. D. J. Smith, A. V. Zvyagin, and D. D. Sampson, "Real-time dispersion compensation in scanning interferometry," Optics Letters 27, 1998-2000 (2002).

[Sorokin 2000] E. Sorokin, G. Tempea, and T. Brabec, "Measurement of the root-mean-square width and the root-mean-square chirp in ultrafast optics," J. Opt. Soc. Am. B 17, 146-150 (2000).

[Tearney 1996] G. J. Tearney, B. E. Bouma, S. A. Boppart, B. Golubovic, E. A. Swanson, and J. G. Fujimoto, "Rapid acquisition of in vivo biological images by use of optical coherence tomography," Optics Letters 21, 1408-1410 (1996).

[Tearney 1997] G. J. Tearney, B. E Bouma, and J. G. Fujimoto, "High speed phase- and group-delay scanning with a grating based phase control delay line," Optics Letters 22, 1811-1812 (1997).

[Tran 2004] P. Tran, D. S. Mukai, M. Brenner, and Z. Chen, "In vivo endoscopic optical coherence tomography by use of rotational microelectromechanical system probe ," Optics Letters 29, 1236-1238 (2004).

[Troy 2001] T. L. Troy, and S. N. Thennadil, "Optical properties of human skin in the near infrared wavelength range of 1000 to 2200 nm," J. of Biomed. Opt. 6(2), 167-176 (2001).

[Wang 2003] Y. Wang, J. Stuart Nelson, Z. Chen, B. J. Reiser, R. S. Chuck, and R. S. Windeler, "Optimal wavelength for ultrahigh-resolution optical coherence tomography," Optics Express 11, 1411-1417 (2003).

[Wojtkowski 2004] M. Wojtkowski, V. J. Srinivasan, T. H. Ko, J. G. Fujimoto, A. Kowalczyk, and J. S. Duker, "Ultrahigh-resolution, high-speed, Fourier domain optical coherence tomography and methods for dispersion compensation," Optics Express 12, 2404-2422 (2004).

[Xie 2006] T. Xie, S. Guo, Z Chen, D. Mukai, and M. Brenner, "GRIN lens rod based probe for endoscopic spectral domain optical coherence tomography with fast dynamic focus tracking," Opt. Express 14, 3238 (2006).

[Zvyagin 2003] A. V. Zvyagin, E. D. J. Smith, and D. D. Sampson, "Delay and dispersion characteristics of a frequency-domain optical delay line for scanning interferometry," J. Opt. Soc. Am. A 20, 333-341 (2003).